

This item is the archived peer-reviewed author-version of:

Methane coupling in nanosecond pulsed plasmas : correlation between temperature and pressure and effects on product selectivity

Reference:

Morais Eduardo, Delikonstantis Evangelos, Scapinello Marco, Smith Gregory, Stefanidis Georgios D., Bogaerts Annemie.- Methane coupling in nanosecond pulsed plasmas : correlation between temperature and pressure and effects on product selectivity
Chemical engineering journal - ISSN 1873-3212 - 462(2023), 142227
Full text (Publisher's DOI): <https://doi.org/10.1016/J.CEJ.2023.142227>
To cite this reference: <https://hdl.handle.net/10067/1958810151162165141>

1 **Methane coupling in nanosecond pulsed plasmas: correlation between**
2 **temperature and pressure and effects on product selectivity**

3 Eduardo Morais,^{a†} Evangelos Delikonstantis,^{b,ct} Marco Scapinello,^c Gregory Smith,^a Georgios D.
4 Stefanidis,^{c,d*} Annemie Bogaerts^{a*}

5 ^a PLASMANT, Department of Chemistry, University of Antwerp, Wilrijk-Antwerp 2610, Belgium

6 ^b AristEng S.à r.l., 77, rue de Merl, L-2146, Luxembourg City, Luxembourg

7 ^c Laboratory for Chemical Technology, Ghent University; Tech Lane Ghent Science Park 125, Ghent, B-
8 9052, Belgium

9 ^d School of Chemical Engineering, National Technical University of Athens, Iroon Polytechniou 9, 15780,
10 Athens, Greece

11

12 **Abstract**

13 We present a zero-dimensional kinetic model to characterise specifically the gas-phase dynamics
14 of methane conversion in a nanosecond pulsed discharge (NPD) plasma reactor. The model
15 includes a systematic approach to capture the nanoscale power discharges and the rapid ensuing
16 changes in electric field, gas and electron temperature, as well as species densities. The effects
17 of gas temperature and reactor pressure on gas conversion and product selectivity are extensively
18 investigated and validated against experimental work. We discuss the important reaction
19 pathways and provide an analysis of the dynamics of the heating and cooling mechanisms. H
20 radicals are found to be the most populous plasma species and they participate in hydrogenation
21 and dehydrogenation reactions, which are the dominant recombination reactions leading to C₂H₄
22 and C₂H₂ as main products (depending on the pressure).

23

24 *Correspondence to:

Annemie Bogaerts

annemie.bogaerts@uantwerpen.be

Georgios D. Stefanidis

georgios.stefanidis@ugent.be

gstefani@mail.ntua.gr

25

26 †The authors have equally contributed to this work

27 **1. Introduction**

28 Given the current energy crisis, the societal and industrial importance of natural gas as a primary
29 energy source and feedstock will be significant in the coming decennia. Methane (CH₄), the most
30 abundant compound of natural gas, can be converted stepwise to synthetic fuels via syngas.
31 Alternatively, methane can be converted to valuable chemicals that serve as high added-value
32 building blocks in the chemical industry. Among them, ethylene (C₂H₄) has the highest market
33 value since it is the basic building block for a very broad range of chemicals, including polymers,
34 synthetic fibres, alcohols, and solvents. Thus, scalable and energy-efficient processes to convert
35 methane to ethylene are of high research interest.

36 Ethylene derives from natural gas via thermally driven (catalytic) oxidative or non-oxidative
37 methane coupling. The oxidative coupling of methane is an exothermic reaction occurring at 1000-
38 1200 K, usually in presence of catalyst. Along with ethylene, other lower-value side-products,
39 such as carbon dioxide (CO₂), carbon monoxide (CO), hydrogen (H₂) and water (H₂O), are
40 formed, restricting the application prospects of this route. Unlike oxidative methane coupling, non-
41 oxidative coupling promotes the formation of high-value species, i.e., ethane (C₂H₆), ethylene
42 (C₂H₄) and acetylene (C₂H₂), hydrogen, benzene (C₆H₆) and other aromatics at appropriate
43 temperatures and in presence of suitable catalysts. Carbon and hydrogen are thermodynamically
44 favoured between 1500-3300 K; benzene between 1100-1500 K; acetylene at higher
45 temperatures, whereas ethylene production is maximized between 1300-1800 K.^{1,2}

46 Besides thermally-driven routes,³ electrified options have also been proposed for non-oxidative
47 methane coupling.⁴ In this context, plasma is employed to enable the reaction. Specifically, non-
48 thermal plasma (NTP) can electrically activate methane molecules at lower bulk gas temperatures
49 than pyrolysis, maximizing the conversion of electrical into chemical energy and subsequently,
50 improving the global energy efficiency. Different plasma technologies, i.e., dielectric barrier
51 discharges (DBD),^{5,6} microwave (MW),⁷ gliding arc (GA),⁸ spark and corona,^{9,10} have been tested
52 for methane reforming. In low-energy density plasmas (DBD), ethane is formed as the major
53 product, whereas acetylene formation dominates in high-energy density discharges (MW, GA and
54 spark). Ethylene selectivity is enhanced in corona discharges, yet the overall yield still remains
55 low. Collectively, plasma is not very selective to ethylene unless it is integrated with catalysts
56 suitable for acetylene hydrogenation to ethylene in the post-plasma zone.¹¹ The reason for the
57 very broad product distribution lies in the different electron temperature and electron density each
58 plasma technology features, which impose the operating temperature and consequently, drive the
59 plasma chemistry.

60 The Nanosecond Pulsed Discharge (NPD), a spark-regime discharge that can sufficiently
61 populate the desirable vibrational and electronic states while limiting translational excitation, has
62 been lately adopted to methane valorisation applications, attaining high single-pass C_2 yields at
63 relatively low energy cost.¹¹⁻¹⁴ Acetylene was always the majorly produced, like other high-energy
64 density discharges, but the reaction mechanism has not been defined yet. Only limited works
65 elaborating on methane plasma chemistry have been published; most of them regard
66 microsecond pulsed discharges, a similar but not the same plasma type as NPDs. Kado et al.¹⁵
67 investigated the mechanism of acetylene formation in such discharges; they reported that
68 methane is mainly dissociated via electron impact reactions into atomic carbon, which is then
69 hydrogenated to C_2H and CH and finally, those species serve as the precursors for C_2H_2 formation
70 under certain hydrogenation and recombination reactions. Gao et al.¹⁶ suggested that methane
71 vibrational excitation is the lead methane dissociation mechanism since the vibrational excitation
72 cross section has the dominant role in the energy channelling. They also claimed that vibrational-
73 translational/rotational relaxation promotes thermal methane coupling to C_2 and carbon when gas
74 temperature overpasses 1100 K.

75 Recently, Stefanidis and co-workers reported for the first time in the literature that gas phase
76 plasma-assisted non-oxidative methane coupling can lead to the formation of ethylene as major
77 product in NPDs – attaining $\sim 20\%$ single-pass ethylene yield at $2020 \text{ kJ/mol}_{C_2H_4}$ energy cost –
78 when co-feeding recyclable hydrogen ($CH_4:H_2 = 1:1$) and operating at moderate pressures (3.5 –
79 5 bar).¹⁷ The reaction pathways that shifted the product selectivity from acetylene to ethylene
80 were determined via an isotope analysis. It was found that higher bulk gas temperatures imposed
81 by the overpressure (>3 bar) activate direct gas-phase methane coupling to ethylene and
82 suggested that some acetylene hydrogenation to ethylene takes place at the copper-based
83 reactor electrode.¹⁸

84 In the current work, we aim to elucidate the correlation between temperature and pressure effects
85 on C_2 products selectivity under different operating windows. First, we experimentally study the
86 NPD plasma reactor performance in terms of methane conversion and C_2 selectivity in the
87 pressure range of 1 to 5 bar. Further, we develop a zero-dimensional kinetic model to characterise
88 the gas-phase dynamics of methane conversion in the NPD plasma reactor. The model includes
89 a systematic approach to capture the nanoscale power discharges and the rapid ensuing changes
90 in electric field, gas and electron temperature, as well as species densities. The effects of gas
91 temperature and reactor pressure on gas conversion and product selectivity are extensively
92 investigated and validated against the experimental work. Finally, we discuss the important

93 reaction pathways and provide an analysis of the dynamics of the heating and cooling
94 mechanisms.

95 **2. Experimental and computational methodology**

96 **2.1. Nanosecond pulsed plasma setup**

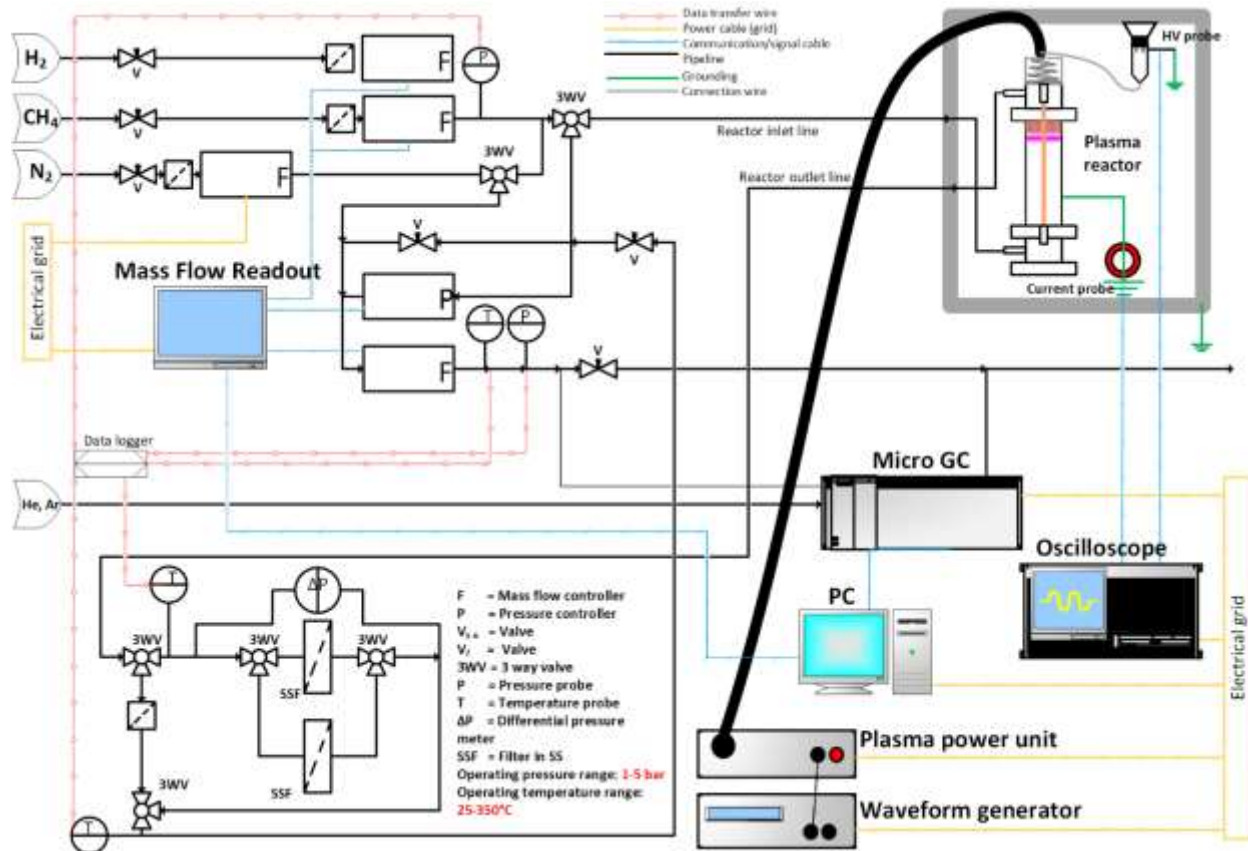
97 The experimental setup used for the plasma-assisted non-oxidative methane experiments is
98 presented in Figure 1. The discharge was ignited by a nanosecond pulsed power supply (n-PS)
99 (NPG-18/100k, Megaimpulse Ltd.) which was triggered by a waveform generator (WFG) (33220A,
100 Keysight Technology) at 3 kHz pulse repetition frequency. Based on a parametric study previously
101 conducted,¹⁹ a pulse repetition frequency of 3 kHz led to an optimum performance with respect
102 to single-pass conversion and energy efficiency. A high-voltage probe (P6015A Tektronix, 75 MHz
103 bandwidth) and an I/V converter (CT-D-1.0, Magnelab, 200Hz-500MHz bandwidth) were used for
104 the pulse voltage and current measurement, respectively. Voltage and current signals were
105 recorded over the course of the experiment by a digital oscilloscope (Wavesurfer 10, Teledyne
106 Lecroy) with a sampling frequency of 10 Gs/s. The pulse energy (E_{pulse}) was estimated as
107 elsewhere.²⁰ It equals the integral of the instantaneous power ($V \times I$), considering the voltage (V)
108 and current (I) signals time delay. The voltage and current signals time delay was calculated by
109 zeroing the $V \times I$ product time integral in the absence of plasma, managed by filling the plasma
110 reactor with SF_6 .²¹ Optical access to the discharge was not possible, however, representative
111 pictures of the nanosecond pulsed discharge can be found in our previous work.¹⁹

112 The co-axial plasma reactor consisted of an inner, copper-based, axial wire (2.2 mm diameter)
113 and an outer, stainless steel-based, co-axial tube (10.4 mm and 13 mm internal and external
114 diameter, respectively). The inner axial wire constituted the high voltage (HV) electrode of the
115 reactor while the outer coaxial tube constituted the ground electrode (GE) of the reactor. The
116 interelectrode distance (plasma gap) and the coaxial plasma reactor length were 4.2 mm and
117 25 cm, respectively. The mixture of the reactants was fed through the bottom of the reactor
118 (reactor inlet line) and the reactor effluent exited from the top of the reactor (reactor outlet line).

119 Mass flow controllers (GF40 Series, Brooks Instrument) controlled the feed flow rate of the
120 reactants (100 sccm CH_4 and 100 sccm H_2 ; Air Liquide 99.995% purity). A filter (SS-4TF-7,
121 Swagelok) with 7-micron pore size was installed at the plasma reactor outflow to retain the formed
122 carbon. A differential pressure meter (Model 700.02, WIKA) was used to monitor the differential
123 pressure across the filter cloth, which was cleaned when the differential pressure gauge exceeded
124 a certain value. The plasma reactor pressure was regulated by using a pressure flow controller

125 (SLA5820, Brooks Instrument) that was placed after the filter. A third mass flow controller (GF40
126 Series, Brooks Instrument), which was operated as flowmeter, continuously recorded the
127 volumetric flowrate of the plasma reactor effluent. However, the readout value depends on a gas
128 factor, which varied with the gas composition. Since the latter was not constant over the course
129 of the plasma reaction, N₂ (Air Liquide, 99.999% purity) was used as internal standard to
130 accurately measure the volume of the plasma reactor effluent. A known amount of N₂ (5 sccm)
131 was only fed to the plasma reactor effluent (not inside the plasma zone over the course of the
132 reaction).²² The three-way valve (3WV) was positioned in a manner such that N₂ was not allowed
133 to flow through the plasma reactor along with the reactants, instead it drove the N₂ flow towards
134 the reactor effluent. The outlet flow rate was obtained by multiplying the initial total flowrate
135 (CH₄+H₂+N₂) by the ratio of the chromatographic area of N₂ before and during the plasma. An
136 additional mass flow controller (4800 series, Brooks Instrument) was used to set the internal
137 standard N₂ flow. The mass flow controllers were configured accordingly, and the respective gas
138 factors were set before setting up of the experiments. The mass flow controllers for CH₄ and N₂
139 supply were set by default only for CH₄ and N₂ handling. Pressure probes (P1600 and P1650,
140 Pace Scientific) and thermocouples (PT 900 Pace scientific) were employed to monitor the reactor
141 operating conditions.

142 The analysis of the plasma reactor product stream was performed by an on-line GC (3000
143 MicroGC, Inficon). H₂, N₂ and CH₄ were detected by a molesieve column (10 m) with backflush
144 (3 m, Plot U), while for C₂ species a Plot U column (10 m) with backflush (1 m, Plot Q) was used.



145

146 **Figure 1** Schematic representation of the experimental set-up used for the non-oxidative methane coupling
 147 experiments.

148 The following metrics were assessed to evaluate the plasma reactor performance: CH₄
 149 conversion, C₂ selectivity and power input:

150
$$\text{CH}_4 \text{ conversion} = \left(1 - \frac{[\text{CH}_4]_{\text{out}} \times v_{\text{out}}}{[\text{CH}_4]_{\text{in}} \times v_{\text{in}}} \right) \times 100\% \quad (1)$$

151
$$\text{C}_2\text{H}_x \text{ selectivity} = \frac{2 \times [\text{C}_2\text{H}_x]_{\text{out}} \times v_{\text{out}}}{[\text{CH}_4]_{\text{in}} \times v_{\text{in}} - [\text{CH}_4]_{\text{out}} \times v_{\text{out}}} \times 100\% \quad (2)$$

152
$$\text{Power input (MW)} = E_{\text{pulse}} \times \left(\frac{\text{MJ}}{\text{pulse}} \right) \times f \left(\frac{\text{pulses}}{\text{s}} \right) \quad (3)$$

153 where [...]in and [...]out correspond to CH₄ concentration at the plasma reactor feed and effluent
 154 stream, respectively, while v_{in} and v_{out} correspond to the corrected volumetric flowrates.

155 2.2. Plasma-kinetic model

156 (a) Numerical details

157 Our zero-dimensional kinetic model was constructed using the ZDPlasKin kinetic solver,²³ which
 158 operates by evaluating the continuity differential equation for each chemical species s with
 159 number density $n_s(t)$ considered in the model:

$$160 \quad \frac{dn_s}{dt} = \sum_r C_{r,s} k_r \prod_q n_q \quad (4)$$

161 where $C_{r,s}$ is the stoichiometric coefficient of a given species s in reaction r , k_r is the rate coefficient
 162 of reaction r and q is the colliding species in this process. Reactions which do not involve electron
 163 collisions use rate coefficients k_r from literature. k_r was given within a temperature range and
 164 written as a function of gas temperature where such data existed. In the case of electron impact
 165 reactions, k_r was extracted from continuous evaluation of collisional cross sections and the
 166 Electron Energy Distribution Function (EEDF) via the BOLSIG+ solver. BOLSIG+ operates in
 167 tandem with ZDPlasKin and requires electric field as input to derive the EEDF, from which the
 168 mean electron energy is determined, to then return rate coefficients for electron impact
 169 reactions.²⁴ The electric field E , required by BOLSIG+ to solve the Boltzmann equation, is
 170 calculated via the differential of the Joule heating equation

$$171 \quad \frac{dP}{dV} = \mathbf{J} \cdot \mathbf{E} = \sigma E^2 \quad (5)$$

172 in which P is the power deposited in a volume element V , J (or σE) is the current density and σ is
 173 the electron conductivity, which is calculated by $\sigma = en_e \mu_e$ (e being the elementary charge, n_e the
 174 electron number density and μ_e the electron mobility, calculated by BOLSIG+).²⁴

175 Neglecting any spatial dependence, the reduced electric field (E/N) is determined from the power
 176 density $p \equiv P/V$ as

$$177 \quad \left(\frac{E}{N}\right) = \frac{1}{N} \sqrt{\frac{p}{\sigma}} \quad (6)$$

178 with N being the total number density of species in the gas phase.

179 **(b) Power input**

180 The power discharges were integrated in the model as power density, defined by the ratio of
 181 instantaneous power and volume of the plasma region. The instantaneous power contained in
 182 the discharges was determined using the experimental voltage and current profiles, whilst the
 183 volume of the plasma region in the reactor was assumed to be constant for the duration of the
 184 pulses.¹⁷ The power density was defined as a function of time using linear functions to generate
 185 asymmetrical triangular power pulses (shown in section 3.2 below). This definition considered the

186 intensity and nanoscale width or duration of each individual pulse, as well as pulse frequency and
187 operational duty cycle. In the theoretical framework of this model, this approach allowed for an
188 accurate representation of the plasma discharges and their variation with the applied pressure in
189 the reactor. These were measured by current and voltage probes during the experiments and are
190 shown in the Supporting Information (SI, section 2).^{17,20} In the interest of model stability and
191 physicality, the concept of a minimum power density between the pulses (*i.e.* plasma off period)
192 was introduced to maintain the electron density and the electric field within viable ranges for model
193 operation.

194 **(c) Gas temperature**

195 Calculations of gas temperature variation with time were performed self-consistently using the
196 reaction enthalpies included in the model.²⁵ As the gas temperature T_{gas} (in Kelvin) can be
197 assumed to be the same for all neutral species, only the adiabatic isometric heat transport
198 equation needs to be solved:²³

$$199 \quad N \frac{\gamma k}{\gamma - 1} \frac{dT_{\text{gas}}}{dt} = P_{e,el} + \sum_j R_j \Delta H_j - P_{\text{ext}} \quad (7)$$

200 where $N = \sum n_i$ is the total neutral species density, γ is the specific heat ratio of the total gas
201 mixture, k is the Boltzmann constant (in J K^{-1}), $P_{e,el}$ is the gas heating power density due to
202 elastic electron-neutral collisions (in W m^{-3}), R_j is the rate of reaction j (in $\text{m}^{-3} \text{s}^{-1}$), ΔH_j is the heat
203 released (or consumed when this value is negative) by reaction j (in J) and P_{ext} is the heat loss
204 due to energy exchange with the surroundings (in W m^{-3}). A detailed description of the gas
205 temperature calculations is given in the SI (section 3).

206 **(d) Gas expansion**

207 Certain reactions in the chemistry of CH_4 conversion involve the formation of two molecules from
208 one molecule. These reactions cause gas expansion, affecting the pressure and flow rate, which
209 are calculated from the actual species density, velocity and gas temperature. To ensure
210 conservation of gas pressure and mass flow rate, the species densities (calculated using eq. 4)
211 and velocity are corrected at every time step to account for gas expansion. More details are given
212 in Kozak and Bogaerts.²⁵

213 **(e) Assumed plasma volume and number of pulses per residence time**

214 Accurate kinetic (and fluid dynamic) modelling under plasma discharges, particularly for
215 simulations carried out with self-consistent temperature calculations, at atmospheric pressures
216 and using pulsed power sources, is a challenging task. In particular, to model pulsed discharges

217 in a 0D framework, it was necessary to make assumptions about the plasma volume and the
 218 number of pulses experienced by the gas molecules during their residence time in the reactor.^{26,27}
 219 Hence, the modeller needs to make some assumptions to run within a feasible time-scale. Here
 220 we describe these assumptions, as well as the limitations of the model.

221 The volume of the plasma discharges in this reactor configuration was estimated to be 3% of the
 222 total volume of the reactor at 1 bar. Provided that the NPD streamer (accurately approximated as
 223 a column) diameter can be $\sim 0.3 \text{ mm}^{13}$ at these operating conditions and considering the total
 224 effective reactor volume to be the space defined by the NPD streamer diameter and the plasma
 225 reactor cross-section area (since the NPD streamer is erratically ignited around the HV electrode),
 226 only $\sim 3\%$ of the total effective reactor volume is occupied by the NPD streamer during each
 227 event. This volume was assumed to remain constant in the pressure range of 1 to 5 bar. The
 228 difference between the total volume of the reactor and the plasma region affects how many pulses
 229 are experienced by each gas molecule traversing the reactor within the residence time. Although
 230 the pulse frequency is set to 3 kHz in the experiments, it is obvious that molecules travelling
 231 through the reactor will not be exposed to 3000 power pulses in 1 second (even if this were their
 232 residence time in the reactor). This is because exposure to power discharges occurs only in the
 233 plasma region, since the pulses are contained within the plasma volume. Considering these
 234 factors, the model was adjusted to account for 15 pulses, as an approximation to the number of
 235 pulses experienced by the gas molecules in the reactor. In all cases this number of pulses was
 236 sufficient for the modelled results to remain unaltered after the twelfth pulse.

237 **(f) Conversion and selectivity**

238 The CH₄ conversion is calculated as follows:

$$239 \quad \chi_{\text{CH}_4}(\%) = 1 - \frac{n_{\text{CH}_4 f} (\text{cm}^{-3}) v_f (\text{cm s}^{-1})}{n_{\text{CH}_4 i} (\text{cm}^{-3}) v_i (\text{cm s}^{-1})} \times 100\% \quad (8)$$

240 where $n_{\text{CH}_4 i}$ and v_i are the initial CH₄ density and velocity, while $n_{\text{CH}_4 f}$ and v_f are the final CH₄ density
 241 and velocity.

242 The hydrocarbon selectivity is calculated as follows:

$$243 \quad S_{C_x H_y}(\%) = \frac{x n_{C_x H_y} (\text{cm}^{-3}) v_f (\text{cm s}^{-1})}{n_{\text{CH}_4 i} (\text{cm}^{-3}) v_i (\text{cm s}^{-1}) - n_{\text{CH}_4 f} (\text{cm}^{-3}) v_f (\text{cm s}^{-1})} \times 100\% \quad (9)$$

244 with $n_{C_x H_y}$ being the density of any given hydrocarbon in the steady state.

245 **2.3. Chemistry included in the model**

246 A mixture of CH₄ and H₂ at a 50/50 ratio was adopted as input gas, in order to compare with the
 247 experiments. The species included in the model comprise CH₄ and H₂ molecules in ground and
 248 some vibrationally excited states, C and H atoms, various compounded C_xH_y molecules, as well
 249 as the corresponding radicals and ions, as shown in Table 1. These species react with each other
 250 in a large number of reactions, as detailed in SI (sections 4 – 6). To develop this reaction set, we
 251 built upon the basis of an earlier publication by PLASMANT, which investigated the utilisation of
 252 different plasma sources in CH₄ conversion.²⁸ In this study, ionic processes were expanded, rates
 253 of recombination reactions were updated and H₂ VV interactions were corrected to include
 254 detailed balance. These modifications were carried out using rate coefficients procured from
 255 various sources in the literature. A complete list of the reactions and corresponding rate
 256 coefficients (including interactions between vibrational levels), as well as relevant citations, can
 257 be found in Tables S2 – S5 in the SI.

258 **Table 1** Species considered in the model.

Stable molecules			Radicals			Ions and electrons				Excited molecules					
CH ₄	H ₂	C ₂ H ₂	C	C ₂	C ₃	H	CH ₃	H ⁺	H ₂ ⁺	H ₃ ⁺	C ⁺	C ₂ ⁺	CH ⁺	CH ₂ ⁺	Vibrational:
C ₂ H ₄	C ₂ H ₆	C ₃ H ₆	CH ₂	CH	C ₂ H	CH ₃ ⁺	CH ₄ ⁺	CH ₅ ⁺	C ₂ H ⁺	C ₂ H ₂ ⁺					H ₂ (v = 1...14)
C ₃ H ₈	C ₄ H ₁₀	C _(s)	C ₂ H ₃	C ₂ H ₅	C ₃ H ₅	C ₂ H ₃ ⁺	C ₂ H ₄ ⁺	C ₂ H ₅ ⁺	C ₂ H ₆ ⁺						CH ₄ (v = 1...4)
			C ₃ H ₇	C ₄ H ₉		H ⁻	CH ⁻	CH ₂ ⁻	electrons						Electronic: H ₂ [*] and CH ₄ [*]

259

260 3. Results and discussion

261 3.1. Plasma reactor performance

262 A streamer-to-spark discharge was ignited which covered only a restricted volume inside the co-
 263 axial plasma reactor; it accounted for ~ 3% of the hollow-cylindrical shaped volume around the
 264 HV electrode, as defined by the streamer diameter and the plasma reactor cross-section area.¹³
 265 The limited plasma volume compared to the reactor cross section provided rapid product
 266 quenching: the products exiting the plasma zone were instantly mixed with the low-temperature
 267 unreacted gases; the bulk gas temperature abruptly dropped and consequently, undesirable side-
 268 reactions, i.e., C₂ species decomposition to carbon and hydrogen, were inhibited. The quenching
 269 rates may have been enhanced by the repetitive ignition (in the order of nanosecond) of the spark.
 270 It is noted that reactions can also be enabled in the proximity of the plasma zone, at distances
 271 longer than that of the discharge diameter, due to the relatively high gas temperature.²⁹ Hydrogen

272 was co-fed to suppress carbon and benzene formation and increase acetylene selectivity at the
273 expense of methane conversion.³⁰

274 The reactor performance in the non-oxidative CH₄ conversion is presented in Figure 2. Pressure
275 increase incentivises the electron-molecule collision frequency and the electron mean energy. As
276 the discharge pressure is increased, the system is driven to thermal equilibrium leading to a higher
277 number of electron-molecule collisions, and resulting in lower electron mean energy, thereby less
278 energetic collisions. Therefore, methane conversion is initially boosted from 30% to 45% as
279 pressure rises from 1 to 4 bar. At 5 bar, there is a slight drop in methane conversion, due to the
280 slightly lower discharge energy. Beyond 5 bar, the reduction of electron mean energy becomes
281 significant and conversion is compromised.

282 Regarding product distribution, C₂H₂ is the dominant product when operating at atmospheric
283 pressure. At 2 bar and higher pressures, C₂H₄ becomes the dominant product. The highest
284 ethylene selectivity is attained at 5 bar. At this pressure, the C₂H₂ and C₂H₆ yields account for
285 less than 5% of product distribution. This product selectivity shift can be attributed to the direct
286 CH₂ radical coupling (with CH₃) to ethylene and C₂H₃ hydrogenation with H radicals – both
287 reactions are enhanced by high bulk gas temperatures imposed by the overpressure (> 3 bar) –
288 as revealed by the isotopic analysis previously performed by Stefanidis and co-workers¹⁸ and
289 further explored in the reaction pathway analysis provided by the modelled results (section 3.5).
290 Moreover, in pulsed plasmas, catalytic hydrogenation occurring at the surface of the copper-
291 based HV electrode also has an effect on the improved C₂H₄ selectivity at higher pressures,¹⁸
292 owing to the ability of copper to promote C₂H₂ to C₂H₄ hydrogenation reactions.³¹ In a future follow-
293 up, we intend to expand this work to investigate this effect under these conditions both on
294 experimental and computational fronts.

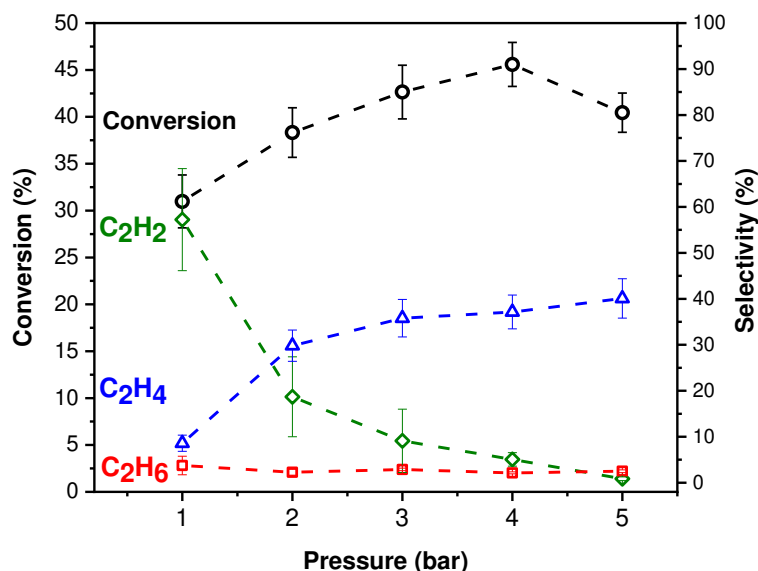


Figure 2. NPD plasma reactor performance in terms of CH₄ conversion and C₂ selectivity across the 1 – 5 bar pressure range. Total feed rate: 200 sccm; gas feed composition: CH₄:H₂ = 1:1; frequency: 3 kHz; discharge gap: 2.4 mm.

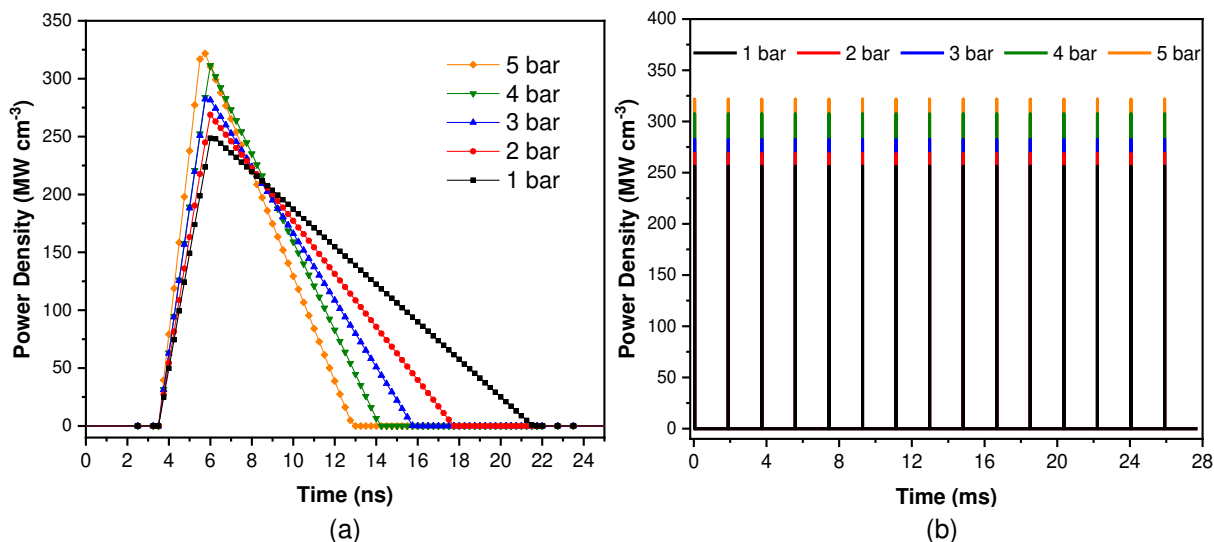
295

296
297
298
299

300 3.2. Modelled plasma characteristics

301 In all calculations carried out in this study, the following parameters were kept constant: gas
302 feed composition of CH₄:H₂ = 1:1, gas flow rate of 200 sccm, reactor dimensions (see section
303 2.1), pulse frequency of 3 kHz, number of modelled pulses as 15 pulses, initial gas
304 temperature of 298.15 K and volume of the plasma region as 3% of the reactor volume.¹³ This
305 was done to highlight the effects of variations in the applied pressure (1 to 5 bar) and power
306 input (and in turn gas and electron temperature), as well as to study how CH₄ conversion,
307 product selectivity and reaction pathways respond to these different conditions of pressure
308 and power input.

309 The time-resolved power density profiles constructed to emulate the pulsed plasma
310 discharges at different pressures are shown in Figure 3a. Each pulse is characterised by an
311 asymmetrical triangle with shorter upslope (rise time) and longer downslope (fall time). In line
312 with experimental power inputs (see Figure S1), the intensity and width of the power density
313 pulses in the model are pressure dependent, with the maximum power of each pulse rising
314 with pressure and the width decreasing with increasing pressure, generating pulses with
315 shorter duration (sharper triangles).



316
 317 **Figure 3** (a) One asymmetrical triangular pulse at different pressures (1 to 5 bar) in the nanosecond range.
 318 The duration of the pulses varies from ~ 10 ns at 5 bar to 18 ns at 1 bar. (b) The 15 power pulses and afterglows
 319 modelled for the gas residence time (27.8 ms) in the reactor, corresponding to a gas flow rate of 200 sccm,
 320 as used in the experiments. The difference in width upon different pressure is not visible, but the different
 321 intensity of each pulse can be observed.

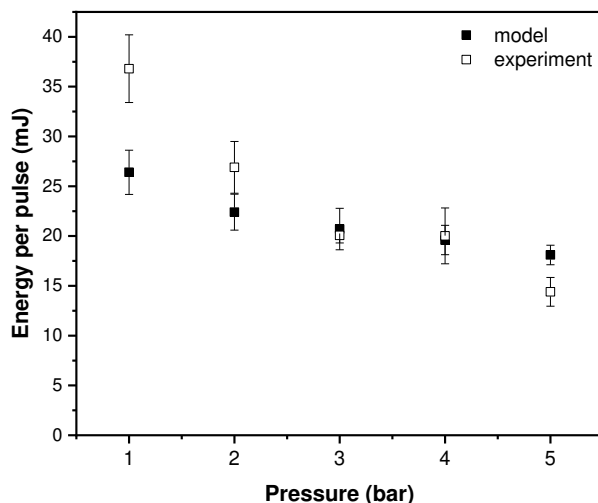
322 In Figure 3b the 15 modelled pulses are plotted at different pressures. While the effect of pressure
 323 on pulse duration is not observable on the timescale of the residence time (ms), the different
 324 height of the power density pulses in the 1 to 5 bar pressure range is evident. The values of
 325 intensity and duration of the pulses for each pressure can be found in Table 2, alongside the
 326 calculated energy injected into the reactor per pulse. Table 2 also shows the total power deposited
 327 within the residence time, the maximum reduced electric field (E/N) reached at the top of the
 328 pulses and the average gas temperature in the afterglow estimated by the model at each
 329 pressure.

330 **Table 2** Pulse characteristics, overall deposited power and calculated reduced electric field and average bulk
 331 gas temperature in the afterglow at different pressures.

Pressure (bar)	Pulse Characteristics			Power (W)	E/N max (Td)	T_{gas} (K)
	Intensity (MW cm ⁻³)	Duration (ns)	Energy (mJ)			
1	251.7	18.0	26.4	14.3	347.5	1037.6
2	269.3	14.2	22.4	12.1	199.1	991.2
3	287.6	12.3	20.7	11.2	179.1	982.9
4	312.4	10.7	19.6	10.6	156.2	990.5
5	329.5	9.36	18.1	9.80	144.1	1074.0

332 The energy (in mJ) channelled into the reactor per power pulse is reduced with rising pressure,
 333 as shown in Table 2. This effect is due to the pulses becoming shorter as the pressure is
 334 increasing (despite the higher intensity), resulting in less energy being deposited in the system

335 with each pulse. This is obviously reflected in the total power (in W), which decreases with
336 increasing pressure. The calculated values and the trend across the pressure range are in good
337 alignment with experimental results (Figure 4), especially in the mid pressure range, boding well
338 for species density and temperature calculations carried out later in the model.

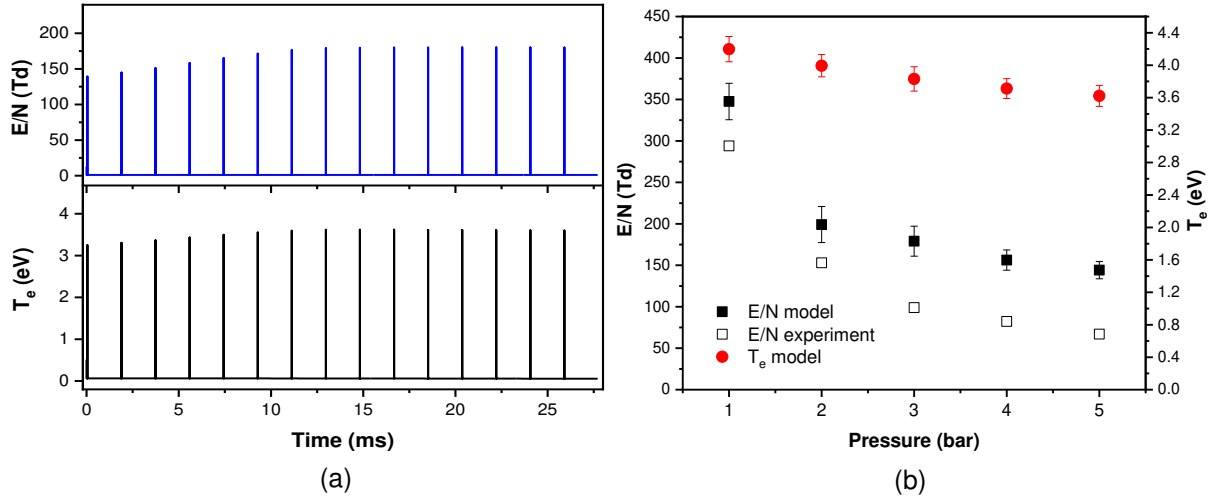


339

340
341
342
343
344

Figure 4 Comparison between modelled and experimental energy per pulse deposited into the reactor across the pressure range studied. The modelled error bars are the standard deviation at each data point.

345 The response of the reduced electric field and in turn of the electron temperature to the power
346 pulses is plotted in Figure 5a. Akin to power density, the two profiles exhibit pulsed behaviour and
347 the peaks in both are coincidental in time with the power discharges.³² This is expected as the
348 model computes the electric field from the power input, and in turn the electric field is supplied to
349 BOLSIG+ for EEDF calculations and electron temperature. The latter determine the energy of
350 electrons in the plasma zone, which will initiate chemical reactions with the incoming CH₄ and H₂
351 molecules in the gas flow. Since the reduced electric field is inversely proportional to the density
352 of gas-phase species, the maximum values calculated by the model (reached at the top of each
353 power pulse) are reduced as the pressure is increased (Figure 5b). This trend is also observed in
354 the experimental values of the electric field (Figure 5b), however these are somewhat lower than
355 those calculated by the model. This is likely due to the nanosecond scale of the pulses, rendering
356 precise acquisition of maximum electric field very difficult, and thus the values measured
357 experimentally may be lower (i.e. with a relative delay) than those reached at the top of the power
358 pulses.²⁷ The resulting calculated maximum electron temperature for each pressure is also plotted
359 in Figure 5b, showing consistency with the trend in the reduced electric field.



360

361

362

363

364

Figure 5 (a) Calculated temporal profile of the reduced electric field (top) showing peaks which are coincidental to the power pulses, as well as pulsed behaviour of the calculated electron temperature as a response to the electric field (bottom). Both calculations were carried out at 4 bar. (b) Maximum reduced electric field and electron temperature values calculated by the model at different applied pressures. The experimental E/N is also shown for comparison.

365

366

367

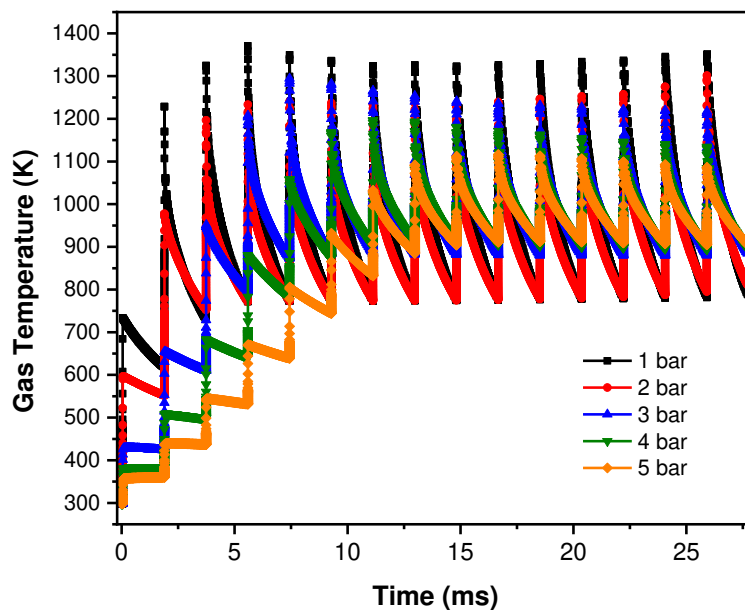
368

369

370

371

Figure 6 displays the profiles of gas temperature versus time for the different applied pressures as calculated by the 0D model (no experimental gas temperatures were measured). All profiles exhibit pulsed behaviour. While heating (leading to temperature peaks) occurs for ~ 120 ns after each power pulse, cooling begins subsequently and is a much slower process (resembling that of an exponential decay) as it takes place on the ms scale (~ 1.2 ms) during the afterglow until the next pulse. The heating and cooling dynamics derived from model calculations are presented and discussed in Section 3.6 below.



372

373

374

375

Figure 6 Calculated temperature profiles at different applied pressures showing the pulsed evolution of calculated gas temperature within the gas residence time.

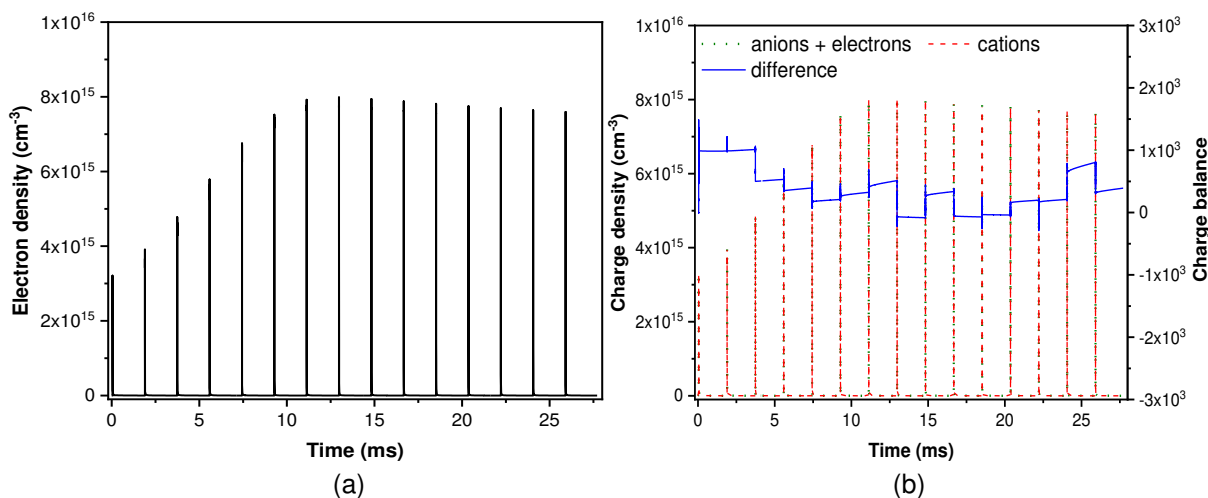
376 The amplitude of temperature variation (*i.e.* the difference between the calculated temperature at
 377 the top of each peak and at the very end of the subsequent afterglow) is inversely proportional to
 378 the applied pressure, with higher variations observed at lower pressures. Note that (i) the more
 379 intense E/N peaks and (ii) longer power depositions at lower pressures will both lead to the
 380 generation of more radicals whose recombination into stable molecules releases energy and
 381 heats the system following the power discharges. As the concentration of radicals is higher at
 382 lower pressures, more heating is experienced, resulting in more intense temperature peaks.³³ The
 383 difference in the amplitude of temperature variation as a function of pressure will be discussed in
 384 section 3.5.

385 In the afterglow, the time-averaged calculated gas temperature is similar at all pressures, around
 386 1000 K, which is comparable to a report by Ravasio and Cavallotti for a similar system.³³ The
 387 calculated gas temperatures ($T_{\text{gas}} = 1400 - 900$ K, with an average of 1000 K) are starkly lower
 388 than the calculated electron temperatures ($T_e = 39000 - 51000$ K or 3.6 – 4.2 eV) for all applied
 389 pressures, clearly indicating that the system operates in a non-thermal plasma regime in all
 390 cases.³⁴ This was also previously observed by Heijkers et al. for CO₂ conversion under NPD
 391 discharges.³²

392 3.3. Modelled analysis of gas phase kinetics

393 (a) Electrons

394 The temporal profile of electron density, showing pulsed behaviour in the model, is shown in
 395 Figure 7a.



396
 397 **Figure 7** Simulated profiles of (a) electron density and (b) sum of electrons and anions versus sum of cations (left
 398 y-axis), with the numerical difference shown on the right y-axis. These calculations were performed at 4 bar.

399 The calculated peak electron densities (*i.e.* during the pulses) vary from $6.9 \times 10^{15} \text{ cm}^{-3}$ (at 5 bar)
400 to $1.1 \times 10^{16} \text{ cm}^{-3}$ (at 1 bar) and this range agrees well with experimental data reported by Maqueo
401 et al³⁵ for CH_4 and CH_4/O_2 mixtures (*i.e.* order of 10^{15} to 10^{17} cm^{-3}). Consistent with other reports
402 in literature, the electron density magnitude is inversely proportional to the applied pressure
403 (Table 3).^{13,18,35}

404 **Table 3** Maximum electron density at each applied pressure

Pressure (bar)	Electron density (cm^{-3})
1	1.08×10^{16}
2	9.97×10^{15}
3	9.22×10^{15}
4	7.99×10^{15}
5	6.95×10^{15}

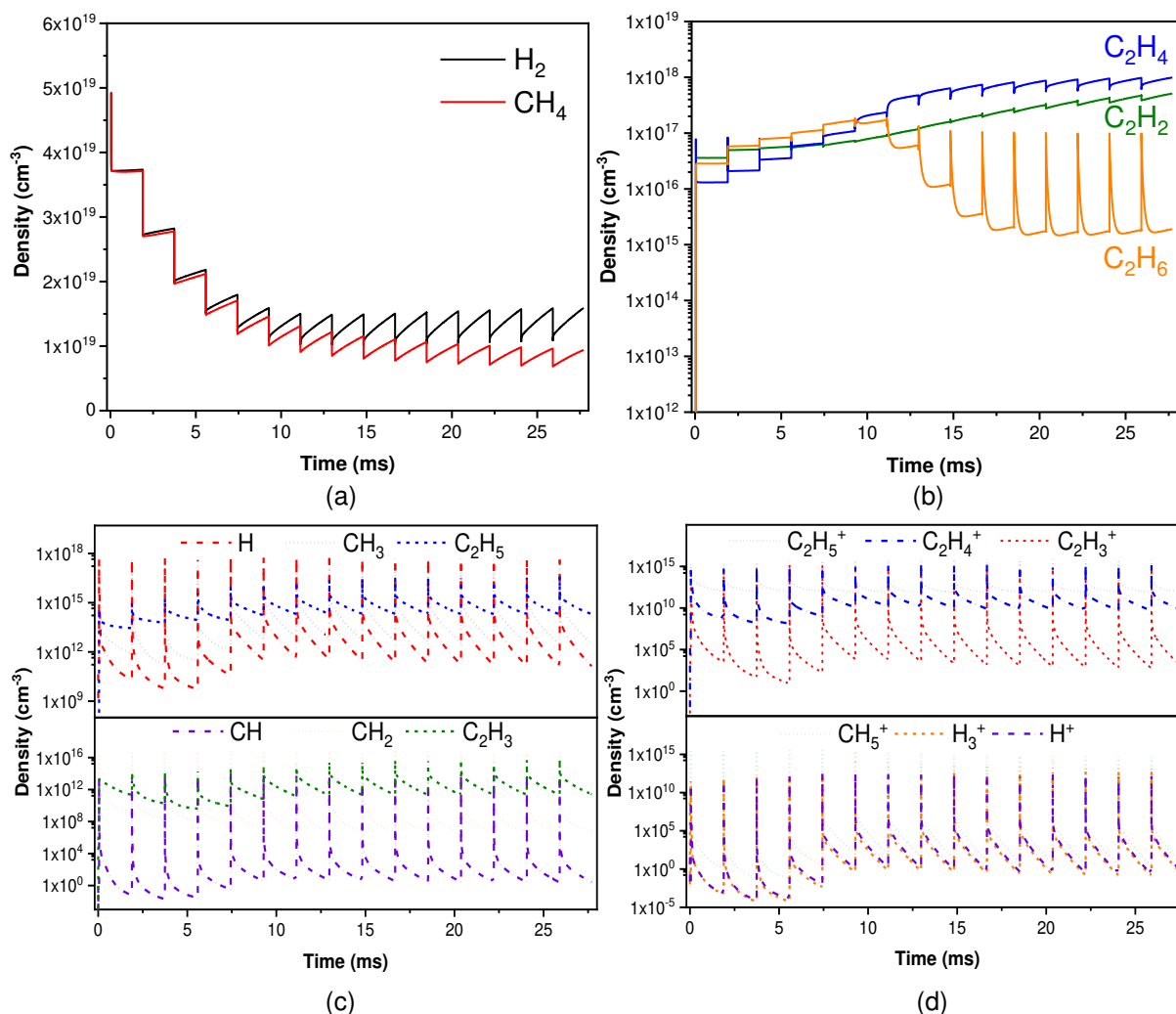
405 The electron density along the residence time reaches its peak at the top of each pulse (Figure
406 7a). Though these densities are high (in line with the intense power discharges), they are very
407 short lived and only last for 9 – 18 nanoseconds, depending on the pressure. Both electron density
408 and electron temperature plummet to negligible values ($\sim 5 \times 10^8 \text{ cm}^{-3}$) in the afterglow (in between
409 the pulses), slowing down or halting electron impact processes, as recombination reactions
410 become more important. The increase in the peak of electron density over the first 6 pulses (~ 10
411 ms) is related to the rise in the gas temperature in the same time period (green profile in Figure
412 6). Due to the ideal gas law, this rise in the gas temperature decreases the number of species
413 (density) in the gas phase, whilst pressure and volume are held constant. Since, the reduced
414 electric field is inversely proportional to the density of neutral gas species, a reduction in the latter
415 causes the reduced electric field to increase, leading to a proportional increase in electron density.

416 As shown in Figure 7b, there is a precise overlay in the profiles of positive ions and of electrons
417 plus negative ions, indicating a tight charge balance is kept throughout the simulations. The
418 maximum difference observed ($\sim 10^3 \text{ cm}^{-3}$; right y-axis of Figure 7b) lies within the error range of
419 the model and is insignificant compared to the magnitude of the charge densities in the model
420 ($10^{11} - 10^{16} \text{ cm}^{-3}$).

421 **(b) Feed gas molecules and major products**

422 Figure 8 displays density profiles of various important species considered in the model. It is clear
423 that all profiles exhibit pulsed behaviour, where sharp and rapid decreases (for the gas feed

424 molecules: CH₄ and H₂) and increases (for the radical and ionic species) occur in simultaneity
 425 with the power pulses, while much slower and gradual variations take place in the interpulse
 426 periods.

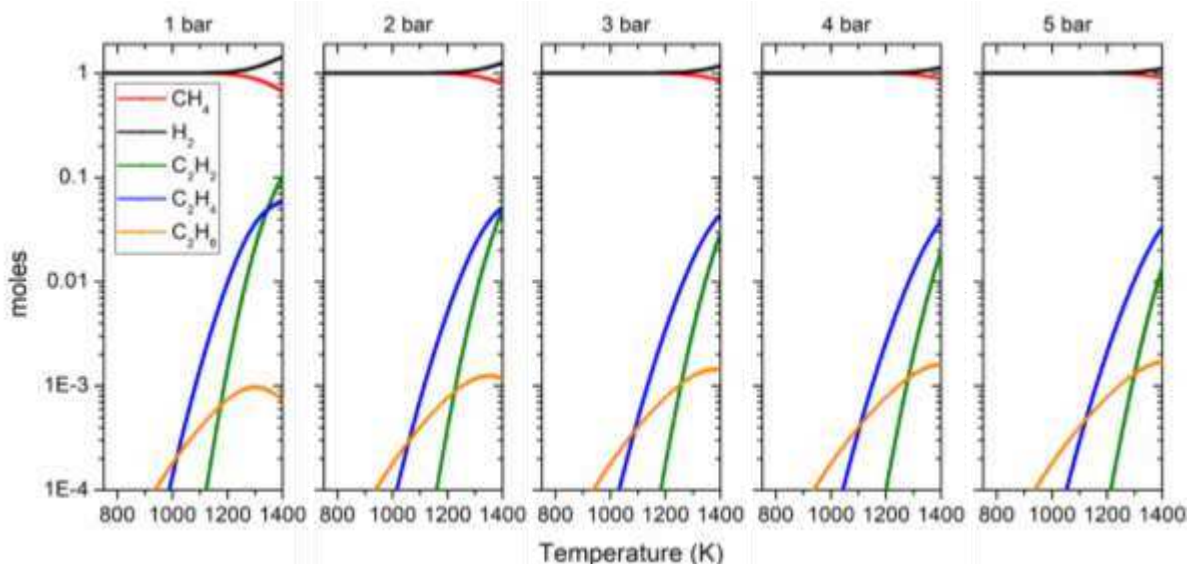


427
 428 **Figure 8** Calculated density profiles of (a) feed gas molecules, (b) major products from non-oxidative CH₄
 429 conversion, (c) most important radicals and (d) main cations in the simulations. These calculations were performed
 430 at an applied pressure of 4 bar.

431 The reactants' profiles show (i) sudden drops where the pulses occur (especially within the first
 432 10 ms of the simulations) and (ii) steady growth in the afterglow, signalling consumption and
 433 reformation, respectively (Figure 8a). CH₄ and H₂ are chiefly decomposed through electron impact
 434 reactions during the power discharges, and reformed otherwise via the very efficient
 435 recombination channels of CH₃ + H and H + H, respectively. Concomitantly, other recombination
 436 reactions lead to the formation of higher hydrocarbons. Overall, H₂ is consumed in the beginning,
 437 however production surpasses consumption after 11 pulses, and H₂ becomes thus a product of
 438 CH₄ conversion. Conversely, CH₄ exhibits a decreasing tendency throughout.

439 At 4 bar, C_2H_4 appears as the top product, followed by C_2H_2 and finally C_2H_6 , which is a minor
 440 product in the entire pressure range. These C_2 species also undergo consumption by electron
 441 impact reactions during the pulses and are reformed in the afterglows, when electron density
 442 decreases between the pulses. After 8 ms, C_2H_4 becomes the dominant product and the density
 443 variations no longer affect the selectivity order at 4 bar (*i.e.* $C_2H_4 > C_2H_2 > C_2H_6$). It is of note that
 444 this onset accompanies the stabilisation of the gas temperature variation (see Figure 6). While
 445 the steady state tendencies observed for the C_2H_4 and C_2H_6 products are roughly attained at 18
 446 ms, the C_2H_2 density continues to increase slightly in the residence time.

447 To elaborate further on this analysis, the thermodynamic equilibrium compositions of the plasma
 448 reactor effluent over the operating temperature (750 – 1400 K, see Figure 6) and pressure range
 449 of interest (1 – 5 bar) are presented in Figure 9. When operating at atmospheric pressure and
 450 temperatures > 1200 K, C_2H_2 is the most stable, thereby, the most favourable product among the
 451 C_2 species. When operating at elevated pressures, particularly > 3 bar, C_2H_4 becomes the most
 452 favourable product over the discussed temperature range (750 – 1400 K). This behaviour tallies
 453 very well with the species density trends depicted in Figure 8, as they match the equilibrium
 454 compositions shown in Figure 9 (plot of 4 bar), suggesting that the rates of interconversion
 455 between C_2H_2 and C_2H_4 via other intermediate species are fast, thus, the relative C_2
 456 concentrations can reach their thermodynamic equilibrium values. Among all the species, CH_4
 457 appears to be the most stable, thereby, the most abundant species under the tested conditions.



458
 459 **Figure 9** Thermodynamic equilibrium compositions of the plasma reactor effluent over the operating temperature and
 460 pressure range of interest. The calculations were performed in ASPEN Plus process simulator, using the Peng-
 461 Robinson equation of state. Feed composition: $CH_4:H_2=1:1$.

462 In Section 3.5 we present a detailed analysis of the effect of pressure and temperature on the
463 reaction pathways and in turn on the product selectivity.

464 **(c) Radicals and ions**

465 The calculated densities of the main radicals and ions are plotted in Figure 8c and 8d,
466 respectively. The densities of all other radicals and ions considered in the model were
467 considerably lower, and therefore not included in this figure. The order of abundance of the
468 radicals shown in the graphs is $H > CH_3 > C_2H_5 > C_2H_3 > CH_2 > CH$. The peak density for all
469 radicals is suddenly (ns scale) reached through electron impact dissociation of molecules during
470 the power pulses. In the wake of each pulse, the radical densities decrease sharply (falling to ~
471 2/3 of the maximum density in the pulse) within 120 ns due to radical recombination. This
472 decreasing tendency remains in later stages of the afterglow, up to the next pulse. However, it
473 deaccelerates significantly, giving rise to the tails seen in the interpulse periods.

474 In Figure 8d it is evident that the main ions in the model follow accurately the trends described
475 above for the radicals. Electron impact ionisation and ionic recombination reactions account for
476 peak cation production and consumption, respectively. The order of abundance of the ions is as
477 follows: $C_2H_5^+ > C_2H_4^+ > H^+ > C_2H_3^+ > CH_5^+ > H_3^+$.

478 **3.4. Calculated conversion and selectivity, and validation with experiments**

479 The calculated and experimental results for CH_4 conversion and C_2 products selectivity are plotted
480 and compared in Figure 10.

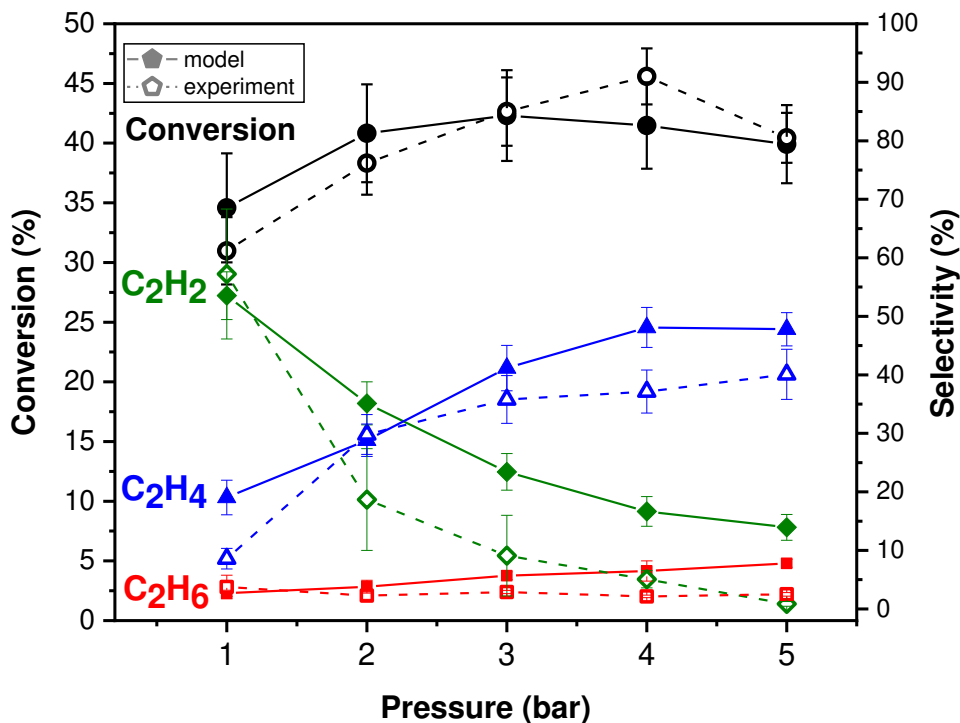


Figure 10 CH₄ conversion and selectivity of C₂H₆, C₂H₄ and C₂H₂. Modelled and experimental results are compared across the 1 to 5 bar pressure range.

481
 482
 483
 484 As observed in Figure 10, it is evident that pressure plays a major role for both conversion and
 485 selectivity in the non-oxidative CH₄ coupling. In terms of conversion, both model and experiments
 486 show that pressure increase has a beneficial effect up to ~ 4 bar (in the experiments; ~ 3 bar in
 487 the model), however a further increase to 5 bar leads to lower conversion than those registered
 488 at 3 and 4 bar.

489 Selectivity varies widely across the pressure range under study. At 1 bar, C₂H₂ is clearly the major
 490 product (at ~ 60%, both in the model and the experiments), followed by C₂H₄ (at 10% in the
 491 experiments and 20% in the model) and finally C₂H₆ appearing as a minor product in the reaction
 492 (at ~ 5%, both the experiments and the model). Such observations for product distribution at 1
 493 bar are in line with other studies of CH₄ conversion under NPD.^{13,33} Raising the pressure to 2 bar
 494 causes significant enhancement in C₂H₄ production and reduces C₂H₂ formation, resulting in
 495 higher selectivity towards C₂H₄ than C₂H₂ in the experiments. In the model, though C₂H₂ still
 496 shows marginally leading selectivity at 2 bar, the trend of rising C₂H₄ formation is accurately
 497 captured. In both model and experiment, from 3 to 5 bar, C₂H₄ becomes the dominant product,
 498 and its selectivity continues to increase, whilst the C₂H₂ selectivity dwindles with every pressure
 499 increment. In fact, the C₂H₂ selectivity falls to ~ 5% at 4 bar and ~ 1% at 5 bar in the experiments,
 500 while remaining at ~ 15% in the model (the reason for this contrast is explained below).

501 Nevertheless, the decaying trend is qualitatively captured by the model. Though the model
502 predicts a gradual increase in C_2H_6 selectivity with pressure (peaking at $\sim 8\%$ at 5 bar), this is not
503 backed up by the experiment, showing that C_2H_6 production is not affected by the applied pressure
504 and remains very slow in all cases.

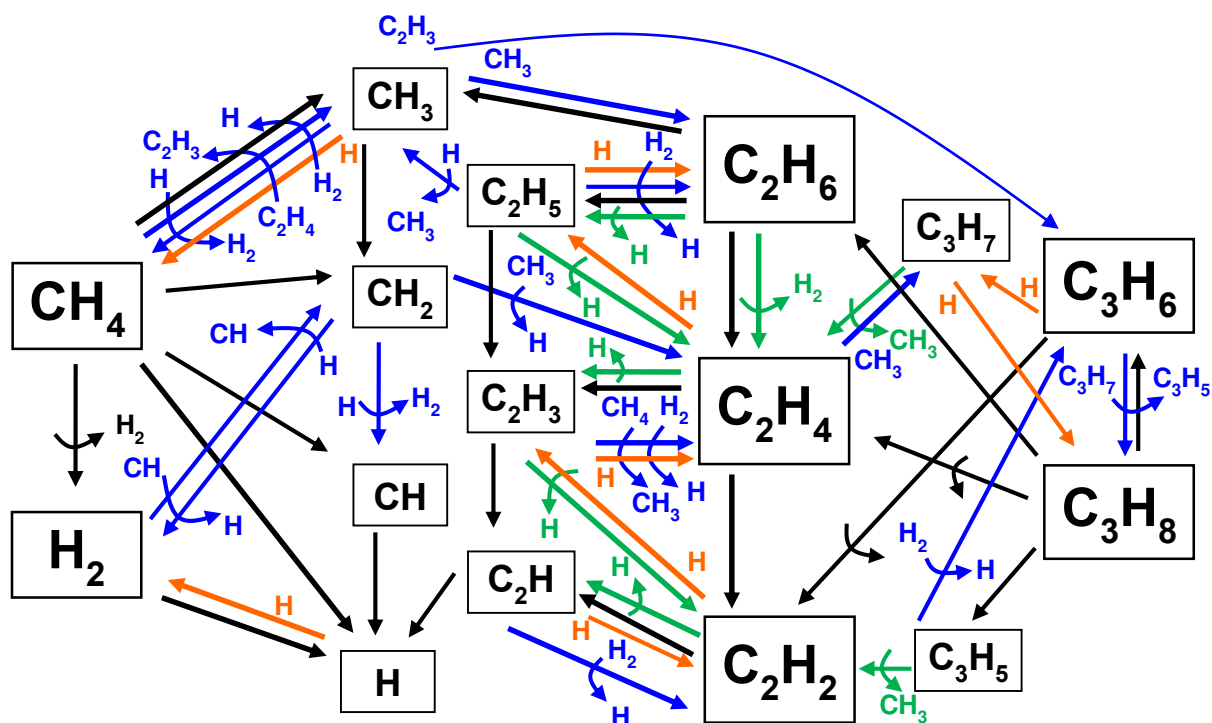
505 The model predicts production of appreciable quantities of C_3H_6 and C_3H_8 , with maximum
506 selectivity (at 5 bar) of 4% and 5.5%, respectively. In the model, C_3H_6 and C_3H_8 are formed at all
507 pressures and their selectivity rises as the pressure is increased. Since C_3 products (or higher
508 hydrocarbons) were not measured in the experiments, this prediction cannot be validated by
509 experimental data. Formation of C_3H_6 , C_3H_8 and $C_{(s)}$ (discussed below) is most likely the reason
510 for the less than 100% selectivity observed in the model and experiments.

511 Significant amounts of coking, i.e., $C_{(s)}$, are produced in the experiments, but remained
512 unquantified. This is likely one of the main reasons, along with C_2H_2 into C_2H_4 hydrogenation
513 promoted by the copper-based HV electrode, for the overestimation in the production of all C_2
514 products in the model, leading to higher C_2 selectivity compared to experimental values, especially
515 at higher pressures. Though low quantities of $C_{(s)}$ are calculated in the model, extensive formation
516 of solid carbon is observed in the reactor and this is detrimental to C coupling into higher
517 hydrocarbons, in turn reducing C_2 selectivity. We believe the model calculations under predicts
518 the formation of $C_{(s)}$, which in turn overestimates the production (and selectivity) of other products.
519 Indeed, stepwise gas-phase dehydrogenation of C_2H_2 into $C_{(s)}$ is the only route considered in the
520 model. In future works, we plan to study the potential C_2H_2 hydrogenation into C_2H_4 catalysed by
521 the copper-based HV electrode in the NPD plasma experiments (as previously discussed in the
522 reactor performance analysis, see Section 3.1)^{31,36,37} and to include more surface species and
523 decomposition reactions, such as benzene pyrolysis and dehydrogenation reactions at the reactor
524 walls (main production avenues for carbon particles).^{6,38,39} However, this lies outside the scope of
525 the present study, among other reasons, because it would require unreasonable computational
526 resources.

527 In summary, modelled and experimental results correspond well for (i) absolute values (maximum
528 12% discrepancy for C_2H_2 selectivity at 5 bar) and (ii) trends across the pressure range. Therefore,
529 in the coming section we will use the model to perform reaction pathway and mechanism analyses
530 and draw correlations between pressure, temperature and gas-phase reactivity.

531 **3.5. Reaction pathway analysis**

532 The formation and consumption routes of various species were investigated using time-resolved
 533 calculations of reaction rates (in the pulses and in the afterglows) of all processes included in the
 534 model. We assessed the reactivity of the multitude of species in the plasma system at steady
 535 state and composed an integral reaction pathway diagram for the reactants and most abundant
 536 products in the model. This reaction pathway analysis was carried out for all pressures, offering
 537 insights into the interplay between pressure, temperature and reactivity of ions and molecules
 538 and the overall selectivity. The findings are discussed below and presented in Figures 11 (which
 539 shows all major neutral reaction pathways), 12 and 13.



540

541 **Figure 11** The complex network of species and reactions involved in (50%) CH₄ and (50%) H₂ conversion at
 542 steady state (this analysis was performed at 4 bar). Thicker arrows in the diagram indicate important reactions
 543 listed in the discussion section. Black arrows indicate electron impact dissociation, blue arrows indicate
 544 recombination reactions, except H radical addition reactions which are the most abundant type of reaction
 545 between neutral species and therefore indicated by orange arrows for clarity. Finally, green arrows indicate
 546 decomposition reactions. Reactants and products are also shown alongside the arrows.

547 CH₄, methane: As feed gas molecule, methane is one of the most abundant species in the model.
 548 As the electron density peaks on the timescale of the pulses, methane is converted into
 549 vibrationally excited CH₄ (v1, 3) (exclusively via electron collisions) and CH₄ (v2, 4) (via electron
 550 collisions and so-called vibrational-vibrational (VV) relaxation from the CH₄ (v1, 3) states), and
 551 also into electronically excited CH₄* (at 7.9 eV), by electron impact excitation. As soon as the
 552 electron density drops in the very early afterglow (nanosecond scale after the pulse), over 99.95%

553 of the vibrationally excited CH₄ species undergo deexcitation, returning to ground state CH₄ via
554 the so-called vibrational-translational (VT) relaxation. Therefore, under the simulated conditions
555 and timescale considered, our model confirms that the vibrational excitation channel does not
556 drive dissociation of CH₄. This result is in line with previous observations described in studies by
557 Heijkers *et al.*,²⁸ Butterworth *et al.*⁴⁰ and Maitre *et al.*⁴¹ Thus, for clarity, the vibrationally (and also
558 electronically) excited CH₄ molecules are not shown in Figures 11 and 13.

559 CH₄ dissociation is initiated by electron impact reactions within the power pulse, leading to CH₃
560 (89.1%), CH₂ (4.76%) and CH (0.45%) radicals. This is illustrated in Figure 8c where radical
561 densities are observed peaking with each pulse. The vast majority of C₁ radicals are generated
562 from ground state CH₄ and from CH₄* (7.9 eV). Especially in the case of CH₃ radicals, CH₄ and
563 CH₄* (7.9 eV) are the main sources, with contributions of 11.90% and 84.35%, respectively. As
564 the afterglow of each pulse begins and electron density drops, radical recombination reactions
565 gain extensive traction, generating higher hydrocarbons (discussed below) and reforming H₂ and
566 CH₄. Two reformation reactions that should be underlined are (i) H + H + M → H₂ + M, accounting
567 for 15% of the H radical total consumption and contributing with 34% to H₂ production, as well as
568 (ii) CH₃ + H + M → CH₄ + M, accounting for 18% and 13% of CH₃ and H radical total consumption,
569 respectively, and being responsible for 78% of CH₄ reformation. These values apply to the 1 bar
570 case and the percentages rise upon pressure increase.

571 H₂, hydrogen: H₂ also has high initial density and also undergoes a vibrational excitation-
572 deexcitation loop, very similar to that discussed above for CH₄. Upon start of the pulses, ground
573 state H₂ molecules are excited to H₂ (v1 – 14) and rapidly deexcited, returning to ground state H₂
574 via VT relaxation. While the relaxation of vibrationally excited H₂ levels is crucial for gas-phase
575 heating, H₂ (v1 – 14) molecules, just as CH₄ (v1 – 4), do not enter dissociation channels to any
576 appreciable extent. Dissociation into H radicals takes place from ground state H₂ (99%) passing
577 through the electronically excited state H₂* (11.83 eV) which, in the model, is a lump of four
578 electronically excited states of H₂: H₂(b³Σ_u⁺), H₂(b¹Σ_u⁺), H₂(c³Π_u⁺) and H₂(a³Σ_g⁺). H radicals are
579 chiefly produced by H₂ dissociation with 47% contribution, while CH₄ + e⁻ → CH₃ + H is the second
580 most important channel in H radical production with 20% contribution. H radicals are the single
581 most important radicals in the system, as they participate in all hydrogenation reactions and are
582 involved in H₂ and CH₄ reformation.

583 A reaction pathway diagram displaying a complex network with the main processes for
584 dissociation and recombination of the most important molecules and radicals in the system is
585 shown in Figure 11. The pathways considered above, and the reactions involved in the formation

586 of C₂ and C₃ products are shown in the context of the entire reaction set. In Figure 12 (below), the
 587 separate production processes for the C₂ hydrocarbons are indicated in more detail, along with
 588 tables for their relative contributions at the different pressures investigated.

589

590

591

592

593

594

595

596

597

598

599

600

601

602

603

604

605

606

607

608

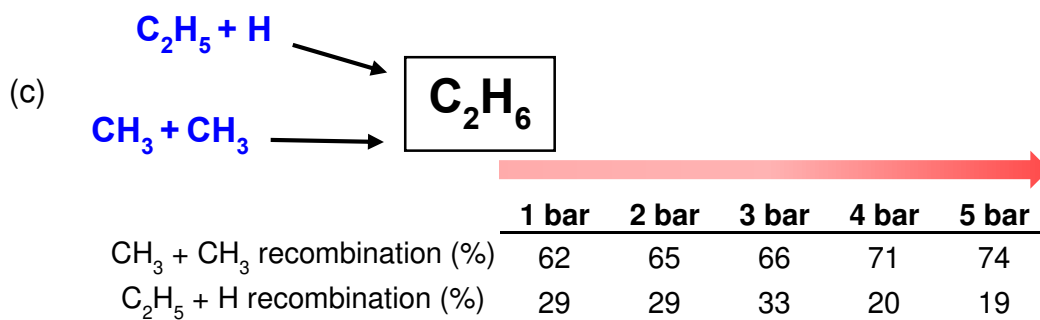
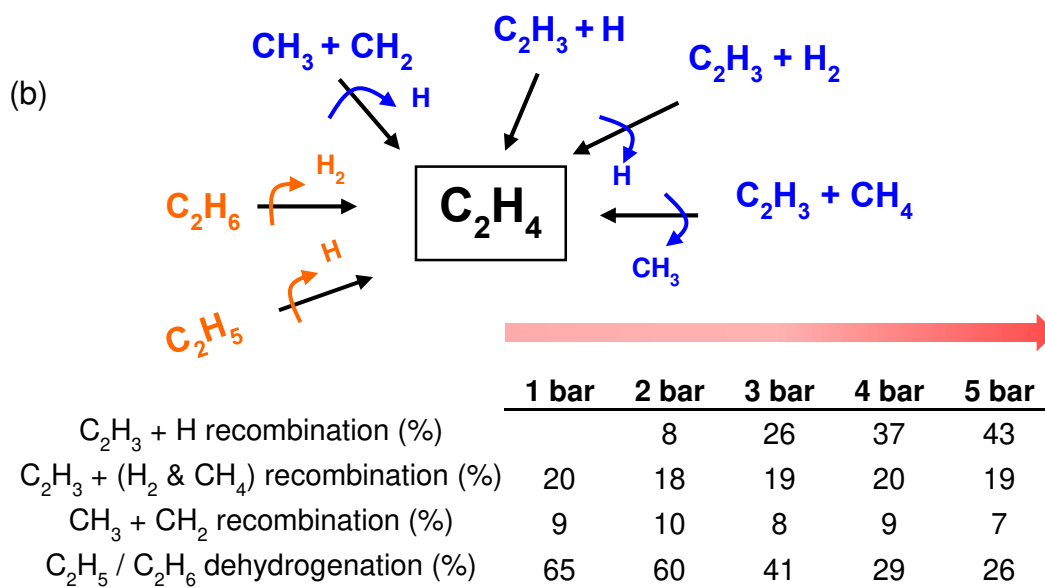
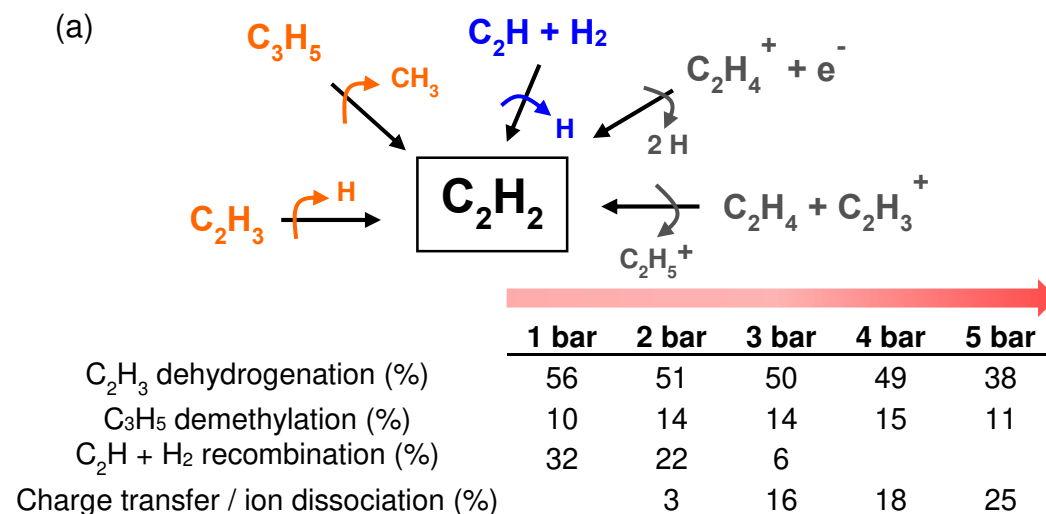
609

610

611

612

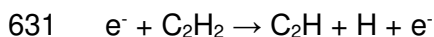
613



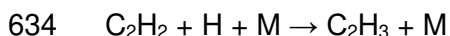
614 **Figure 12** Principal reaction pathways leading to formation of (a) C₂H₂, (b) C₂H₄ and (c) C₂H₆ hydrocarbons
615 in our model. The contribution (%) of each formation route is given across the studied pressure range.

616 C₂H₂, acetylene: C₂H₂ is the least hydrogenated species amongst the stable C₂ hydrocarbons. It
617 is mostly produced via dehydrogenation of C₂H₃ (which is in turn chiefly formed via stepwise
618 dehydrogenation of C₂H₄, C₂H₅ and C₂H₆) and by C₂H and H₂ recombination reactions. In line with
619 our previous mechanistic report,^{11,18} our model confirms stepwise dehydrogenation is the primary
620 route for C₂H₂ production at 1 bar and also stands as the main route across the entire pressure
621 range (see Table in Figure 12a). The efficiency remains approximately constant from 1 to 4 bar
622 and declines at 5 bar. Also, demethylation of C₃H₅ is non-negligible to C₂H₂ production, and
623 alongside C₂H₃ dehydrogenation, these dissociations are the main production channel in the
624 entire pressure range. The recombination between C₂H and H₂ is important at 1 bar, but loses
625 efficiency at 2 bar and becomes insignificant above 3 bar (see Table in Figure 12a). At higher
626 pressures (> 4 bar), as the two main production channels lose strength, the ionic reactions (also
627 shown in Figure 12a) start to play a role in C₂H₂ formation.

628 C₂H₂ undergoes decomposition whilst the power pulses are discharged and in the early afterglow,
629 about ~ 120 ns after each power pulse (as the gas temperature peaks). The larger fraction (57%)
630 of C₂H₂ conversion takes place through dehydrogenation upon electron collision:



632 Besides, hydrogenation of C₂H₂ into C₂H₃ as well as C₂H₂ dissociation upon collision with any
633 neutral molecule (M) account for 22% and 10% of its total consumption, respectively:



636 Once created, C₂H radicals mostly hydrogenate and return to C₂H₂ but also form C₂H₃ and C₂H₅
637 radicals (not indicated in Figure 11, for the sake of clarity). C₂H₃ radicals undergo both
638 hydrogenation (leading to C₂H₄ and eventually C₂H₆) and dehydrogenation (reforming C₂H₂).

639 Considering these pathways, C₂H₂ essentially seems to cycle through dehydrogenation and re-
640 hydrogenation processes with high production efficiency, especially at lower pressures. While the
641 former process leads to C₂H (and C₂H₂ from C₂H₃) and occurs during the power peaks when
642 electrons have maximum energy, the latter takes place immediately after the pulse mainly at 1
643 bar.

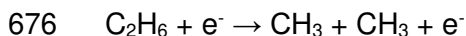
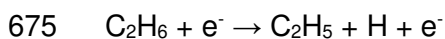
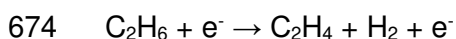
644 C₂H₄, ethylene: Similar to C₂H₂, hydrogenation and dehydrogenation reactions are the principal
645 channel for C₂H₄ formation, as displayed in Figures 11 and 12b. At low pressures (1 and 2 bar),

646 dehydrogenation of C₂H₅ and C₂H₆ provides the largest contribution towards C₂H₄ formation.^{33,42}
647 However, the efficiency of these dehydrogenations dwindles as the pressure is increased (see
648 table in Figure 12b), highlighting the negative effect of high pressure on decomposition reactions.
649 On the other hand, hydrogenation of C₂H₃ (*i.e.* C₂H₃ + H recombination) accounts for the majority
650 of C₂H₄ production in the high-pressure range (3 to 5 bar), and becomes the dominant process at
651 4 and 5 bar (see table in Figure 12b). The C₂H₃ + H₂ or CH₄ recombination reactions are also
652 important, as well as CH₃ + CH₂ recombination, but do not depend on the applied pressure, thus
653 their contribution remains constant across the range. Considering that C₂H₃ is the most abundant
654 C₂ radical, it is not surprising that the main pathways for C₂H₄ formation involve this species.

655 Conversion of C₂H₄ takes place through three distinct channels: (i) hydrogenation to C₂H₅ and (ii)
656 methylation to C₃H₇ both in the late afterglow and (iii) electron impact dissociation to C₂H₃ and
657 C₂H₂ during the power peaks, and these account for 74%, 6% and 19% of the total C₂H₄
658 consumption, respectively. Like C₂H₂, C₂H₄ and C₂H₃ undergo cycles of hydrogenation,
659 dehydrogenation and re-hydrogenation.

660 From the C₂H₂ and C₂H₄ formation and destruction pathway analysis, we can deduce that at low
661 pressures the production of C₂H₂ is favoured, since the dehydrogenation of C₂H₃ (*i.e.*
662 decomposition of C₂H₃ into C₂H₂ and H) is a very efficient channel (see Table in Figure 12a). From
663 3 bar to 5 bar, the principal channel for C₂H₃ conversion shifts from dehydrogenation to C₂H₂ into
664 re-hydrogenation to C₂H₄. In fact, hydrogenation of C₂H₃ (with H radicals, and also with H
665 abstraction from H₂ and CH₄ molecules) becomes the most effective avenue for C₂H₄ production
666 (see Table in Figure 12b), boosting its yield and growing as the main product of CH₄ conversion.

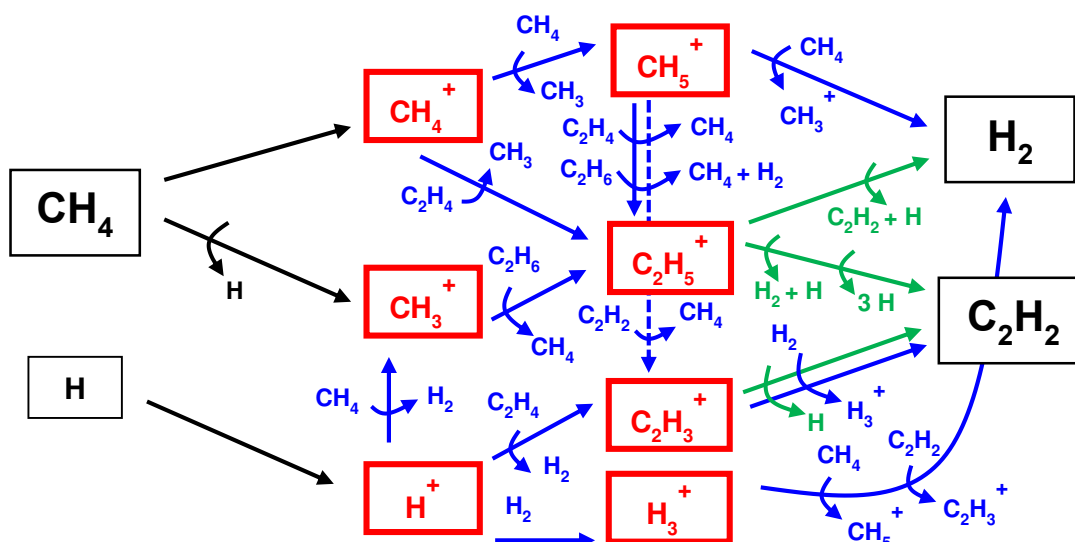
667 C₂H₆, ethane: Unlike C₂H₂ and C₂H₄, gain and loss of H radicals are not the main avenue for C₂H₆
668 production. C₂H₆ is chiefly formed via recombination between CH₃ radicals and the effectiveness
669 of this route increases with pressure (see Table in Figure 12c). It is interesting to note that in the
670 overall process of CH₄ coupling, C₂H₆ is the first C₂ species to be produced (see initial 5 pulses
671 in Figure 8b) owing to the much higher density of CH₃ radicals compared to other C₁ radicals.
672 C₂H₆ is decomposed via three electron impact dissociation reactions, accounting for 45%, 36%
673 and 10% of C₂H₆ consumption, respectively:



677 Also, as the gas temperature rises and stabilises in steady state, C_2H_6 undergoes decomposition
 678 into C_2H_4 and C_2H_5 via dehydrogenation (green arrows in Figure 11). These new C_2 products will
 679 recombine and further dissociate, eventually entering a cycle leading to steady production of C_2H_4
 680 and C_2H_2 as the main products observed at each studied pressure.

681 At all pressures, the gas temperature in the plasma zone is much too high for selective C_2H_6
 682 production, and therefore it is obvious that this product's selectivity remains very low across the
 683 entire pressure range.

684 Ions: The ions are not included in Figures 11 and 12 above, as they do not play a dominant role
 685 in the reaction scheme. However, to highlight their importance in the chemistry, the principal
 686 positive ions along with their formation and destruction routes are shown in Figure 13 below.



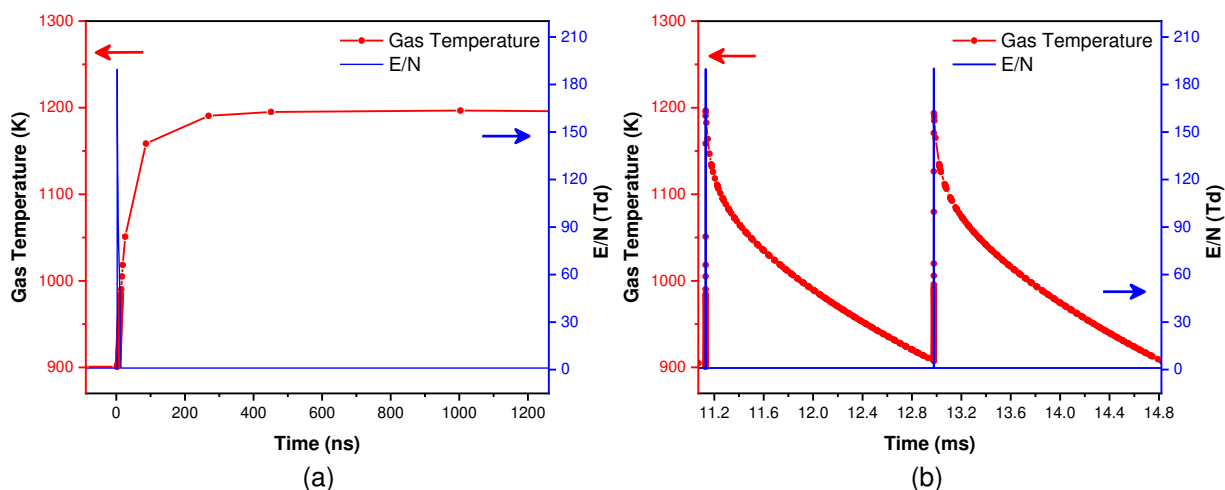
687
 688
 689 **Figure 13** Network of reactions and species involved in the formation and consumption of important
 690 ions in the model. This figure highlights the role of ionic processes in the synthesis of C_2H_2
 691 (especially at high pressures) and reformation of H_2 . Black arrows indicate electron impact
 692 ionisations, blue arrows indicate recombination reactions and green arrows indicate dissociative
 693 neutralisation reactions.

694 Positive ions are exclusively produced through electron impact reactions, as soon as the first
 695 pulse is discharged, either via direct ionisation or dissociative ionisation. The three most abundant
 696 ions primarily formed from the reactants in the feed gas are H^+ , CH_4^+ and CH_3^+ , and subsequently
 697 these positive ions react with neutral molecules (via H^+ abstraction and electron transfer
 698 processes), creating secondary ions (see Figure 13). The most important secondary positive ions
 699 are H_3^+ , CH_5^+ , $C_2H_5^+$ and $C_2H_3^+$. $C_2H_3^+$ and $C_2H_5^+$ are also produced via electron impact
 700 ionisation from their neutral counterparts, while H_3^+ , CH_5^+ are exclusively formed via recombination
 701 reactions from the primary ions.

702 Besides their fundamental role in keeping the charge balance in a plasma environment, this
703 reaction pathway analysis reveals the important role of ions and their reactions in the reformation
704 of H_2 and the production of C_2H_2 . Some of the main neutralisation avenues for H_3^+ , CH_5^+ , $C_2H_5^+$
705 and $C_2H_3^+$ (especially dissociative neutralisation reactions) result in creation of H_2 and C_2H_2
706 molecules, as shown in Figure 13.

707 3.6. Heating and cooling mechanisms

708 As the gas temperature dynamics (i.e., heating and cooling during and after the pulses) play a
709 crucial role in the chemistry of NPD, we also used our model calculations and simulated
710 temperature profiles to perform heat transfer analyses and garner quantitative information on
711 individual reaction contributions to heating and cooling at steady state conditions. In figure 14, we
712 plot the gas temperature (red curve) and the reduced electric field (E/N) (blue curve, to indicate
713 the pulses), for (a) one pulse and the beginning of the ensuing afterglow and (b) two consecutive
714 pulses and afterglows, emphasising the late afterglow periods. The gas temperature undergoes
715 a sharp increase in the model following the E/N peak within the power discharges, as shown in
716 Figure 14a.



717
718 **Figure 14** E/N (blue) and gas temperature (red) profiles over (a) one power pulse and beginning of the ensuing
719 afterglow (the relative scale of the x-axis was adjusted for pulse start at $t = 0$ ns) and (b) two consecutive pulses
720 and two complete afterglows. This calculation was carried out at 4 bar.

721 This temperature rise is due to heat release through exothermic processes and occurs on a similar
722 timescale (ns scale) to that of the pulses. The mechanism for heat release in the system can be
723 understood in three parts.

- 724 (i) As the electron density peaks in the pulses, the rate of elastic momentum transfers is
725 the highest, leading to heating of the gas phase.

726 (ii) Also in the pulse, H₂ vibrational levels are rapidly populated and resulting relaxation
727 (through VT processes) releases heat to the gas phase. These two events cause the
728 steep temperature rise seen in Figure 14a and account for 34% and 29% of the total
729 heating, respectively.

730 (iii) In the early afterglow, *i.e.* 500 ns after the electron density drops, the exothermic
731 recombination reaction, CH₃ + H + M → CH₄ + M + ΔH, sustains the temperature rise
732 on the μs scale (see also Figure 14a), while the cooling events are activated. H and
733 CH₃ radical recombination is responsible for 35% of the total heat release in the model.

734 Conversely, cooling is a much slower process, as it takes place steadily throughout the afterglow,
735 giving rise to the sawtooth profile (red curve in Figure 14b). Heat loss to the reactor walls is the
736 principal cooling event in the system with a contribution of 76% to the total heat loss. Noticeably,
737 cooling is more pronounced in the early afterglow. This is due to two endothermic reactions which
738 take place at high rates in that interval: C₂H₅ + M + ΔH → C₂H₄ + H + M (11 – 17%) and C₂H₃ +
739 M + ΔH → C₂H₂ + H + M (8 – 14%). In the late afterglow, these two reactions lose importance, as
740 stable molecules are formed and the density of radicals drops.

741 Upon rising pressure, the E/N peaks drop (see Figure 5b), lowering the rate of energy transfer
742 from electrons to the gas-phase molecules via elastic collisions and vibrational relaxation. Thus,
743 the temperature peaks become less accentuated at higher pressures. Moreover, at high
744 pressures, endothermic dissociations (such as the C₂H₃ and C₂H₅ decompositions mentioned
745 above) also have significantly lower rates (since maintenance of fewer molecules is favoured),
746 slowing the overall cooling process in the afterglow. Combined, these two effects play a role in
747 progressively reducing the amplitude between the maximum temperature following the pulses
748 and the minimum temperature at the end of each afterglow, as was observed in Figure 6 above.

749 **4. Conclusions**

750 In this work, nanosecond pulsed discharges have been studied for methane conversion using a
751 0D plasma kinetic model, and validated against an experimental setup showing good alignment
752 for conversion and products selectivity. Experimental power deposition characteristics from a
753 coaxial plasma reactor over a pressure range of 1 to 5 bar were taken as input in a 0D model that
754 performs self-consistent gas temperature calculations and incorporates gas temperature and
755 pressure dependent reaction rates.

756 The simulation results highlight pulsed behaviour in all the physical parameters, such as electric
757 field, gas temperature and electron energy, and the densities of plasma species also exhibit
758 pulsed profiles. Good agreement was observed with the experimental measurements of CH₄
759 conversion and C₂ hydrocarbon selectivity, which indicates that the gas-phase kinetic dynamics
760 occurring in the reactor are comparable to those included in the model. A reaction pathway
761 analysis of the simulation results demonstrates that the mechanisms responsible for formation of
762 different C₂ products change upon increasing pressure of the system, which is of importance
763 when considering the C₂H₂ and C₂H₄ selectivity trends in the 1 to 5 bar pressure range. Further
764 analysis of the processes that lead to temperature variations in the gas phase highlights the
765 complexity of the interactions between the different plasma species in such a system.

766 In our future work we plan to look at the effect of carbon deposition and the influence of surfaces
767 on the resulting products and selectivity, with main focus on how post-plasma catalysts can
768 improve the ethylene selectivity by hydrogenation from acetylene. Indeed, the conversion of
769 methane into ethylene using nanosecond pulsed discharges with post-plasma catalysis remains
770 a complex process that requires further study.

771 **5. Acknowledgments**

772 We gratefully acknowledge financial support by the Flemish Government through the Moonshot
773 cSBO project “Power-to-Olefins” (P2O; HBC.2020.2620).

774 **6. References**

- 775 1. Fincke, J. R., Anderson, R. P., Hyde, T. A. & Detering, B. A. Plasma pyrolysis of methane to
776 hydrogen and carbon black. *Ind. Eng. Chem. Res.* **41**, 1425–1435 (2002).
- 777 2. Fincke, J. R. *et al.* Plasma Thermal Conversion of Methane to Acetylene. *Plasma Chem. Plasma*
778 *Process.* **22**, 105–136 (2002).
- 779 3. Guo, X. *et al.* Direct, nonoxidative conversion of methane to ethylene, aromatics, and hydrogen.
780 *Science (80-.)*. **344**, 616–619 (2014).
- 781 4. Scapinello, M., Delikonstantis, E. & Stefanidis, G. D. The panorama of plasma-assisted non-
782 oxidative methane reforming. *Chemical Engineering and Processing: Process Intensification* vol.
783 117 120–140 (2017).
- 784 5. Liu, S. Y., Mei, D. H., Shen, Z. & Tu, X. Nonoxidative conversion of methane in a dielectric barrier
785 discharge reactor: Prediction of reaction performance based on neural network model. *J. Phys.*
786 *Chem. C* **118**, 10686–10693 (2014).
- 787 6. García-Moncada, N., van Rooij, G., Cents, T. & Lefferts, L. Catalyst-assisted DBD plasma for
788 coupling of methane: Minimizing carbon-deposits by structured reactors. *Catal. Today* **369**, 210–
789 220 (2021).
- 790 7. Shen, C., Sun, D. & Yang, H. Methane coupling in microwave plasma under atmospheric pressure.
791 *J. Nat. Gas Chem.* **20**, 449–456 (2011).

- 792 8. Shuanghui, H. *et al.* Conversion of methane to C₂ hydrocarbons and hydrogen using a gliding Arc
793 reactor. *Plasma Sci. Technol.* **15**, 555–561 (2013).
- 794 9. Yang, Y. Methane conversion and reforming by nonthermal plasma on pins. *Ind. Eng. Chem. Res.*
795 **41**, 5918–5926 (2002).
- 796 10. Kuznetsov, D. L., Uvarin, V. V. & Filatov, I. E. Plasma chemical conversion of methane by pulsed
797 electron beams and non-self-sustained discharges. *J. Phys. D. Appl. Phys.* **54**, (2021).
- 798 11. Delikonstantis, E., Scapinello, M. & Stefanidis, G. D. Low energy cost conversion of methane to
799 ethylene in a hybrid plasma-catalytic reactor system. *Fuel Process. Technol.* **176**, 33–42 (2018).
- 800 12. Yao, S. L., Suzuki, E., Meng, N. & Nakayama, A. A High-Efficiency Reactor for the Pulsed Plasma
801 Conversion of Methane. *Plasma Chem. Plasma Process.* **22**, 225–237 (2002).
- 802 13. Lotfalipour, R., Ghorbanzadeh, A. M. & Mahdian, A. Methane conversion by repetitive nanosecond
803 pulsed plasma. *J. Phys. D. Appl. Phys.* **47**, (2014).
- 804 14. Zhang, S. *et al.* Time-resolved characteristics and chemical kinetics of non-oxidative methane
805 conversion in repetitively pulsed dielectric barrier discharge plasmas. *J. Phys. D. Appl. Phys.* **51**, 16
806 (2018).
- 807 15. Kado, S. *et al.* Reaction mechanism of methane activation using non-equilibrium pulsed discharge
808 at room temperature. *Fuel* **82**, 2291–2297 (2003).
- 809 16. Gao, Y. *et al.* Highly efficient conversion of methane using microsecond and nanosecond pulsed
810 spark discharges. *Appl. Energy* **226**, 534–545 (2018).
- 811 17. Scapinello, M., Delikonstantis, E. & Stefanidis, G. D. Direct methane-to-ethylene conversion in a
812 nanosecond pulsed discharge. *Fuel* **222**, 705–710 (2018).
- 813 18. Scapinello, M., Delikonstantis, E. & Stefanidis, G. D. A study on the reaction mechanism of non-
814 oxidative methane coupling in a nanosecond pulsed discharge reactor using isotope analysis.
815 *Chem. Eng. J.* **360**, 64–74 (2019).
- 816 19. Delikonstantis, E., Scapinello, M., Van Geenhoven, O. & Stefanidis, G. D. Nanosecond pulsed
817 discharge-driven non-oxidative methane coupling in a plate-to-plate electrode configuration plasma
818 reactor. *Chem. Eng. J.* **380**, 122477 (2020).
- 819 20. Scapinello, M., Martini, L. M., Dilecce, G. & Tosi, P. Conversion of CH₄/CO₂ by a nanosecond
820 repetitively pulsed discharge. *J. Phys. D. Appl. Phys.* **49**, (2016).
- 821 21. Takashima, K., Zuzeeq, Y., Lempert, W. R. & Adamovich, I. V. Characterization of a surface
822 dielectric barrier discharge plasma sustained by repetitive nanosecond pulses. *Plasma Sources Sci.*
823 *Technol.* **20**, (2011).
- 824 22. Lee, R., Labrecque, R. & Lavoie, J. M. Inline analysis of the dry reforming process through fourier
825 transform infrared spectroscopy and use of nitrogen as an internal standard for online gas
826 chromatography analysis. *Energy and Fuels* **28**, 7398–7402 (2014).
- 827 23. Pancheshnyi, Sergey ; Eismann, Benjamin ; Hagelaar, Gerjan ; Pitchford, L. ZDPlasKin: a new tool
828 for plasmachemical simulations. in *American Physical Society, 61st Annual Gaseous Electronics*
829 *Conference* (2008).
- 830 24. Hagelaar, G. J. M. & Pitchford, L. C. Solving the Boltzmann equation to obtain electron transport
831 coefficients and rate coefficients for fluid models. *Plasma Sources Sci. Technol.* **14**, 722–733 (2005).
- 832 25. Kozák, T. & Bogaerts, A. Evaluation of the energy efficiency of CO₂ conversion in microwave
833 discharges using a reaction kinetics model. *Plasma Sources Sci. Technol.* **24**, (2015).
- 834 26. Van 'T Veer, K., Reniers, F. & Bogaerts, A. Zero-dimensional modeling of unpacked and packed
835 bed dielectric barrier discharges: The role of vibrational kinetics in ammonia synthesis. *Plasma*
836 *Sources Sci. Technol.* **29**, (2020).
- 837 27. Van 'T Veer, K. *et al.* Spatially and temporally non-uniform plasmas: Microdischarges from the

- 838 perspective of molecules in a packed bed plasma reactor. *J. Phys. D. Appl. Phys.* **54**, 15 (2021).
- 839 28. Heijkers, S., Aghaei, M. & Bogaerts, A. Plasma-Based CH₄ Conversion into Higher Hydrocarbons
840 and H₂: Modeling to Reveal the Reaction Mechanisms of Different Plasma Sources. *J. Phys. Chem.*
841 *C* **124**, 7016–7030 (2020).
- 842 29. Lo, A. *et al.* Streamer-to-spark transition initiated by a nanosecond overvoltage pulsed discharge in
843 air. *Plasma Sources Sci. Technol.* **26**, (2017).
- 844 30. Holmen, A., Olsvik, O. & Rokstad, O. A. Pyrolysis of natural gas: chemistry and process concepts.
845 *Fuel Process. Technol.* **42**, 249–267 (1995).
- 846 31. Wang, S. *et al.* Highly efficient ethylene production via electrocatalytic hydrogenation of acetylene
847 under mild conditions. *Nat. Commun.* **12**, (2021).
- 848 32. Heijkers, S., Martini, L. M., Dilecce, G., Tosi, P. & Bogaerts, A. Nanosecond Pulsed Discharge for
849 CO₂ Conversion: Kinetic Modeling to Elucidate the Chemistry and Improve the Performance. *J.*
850 *Phys. Chem. C* **123**, 12104–12116 (2019).
- 851 33. Ravasio, S. & Cavallotti, C. Analysis of reactivity and energy efficiency of methane conversion
852 through non thermal plasmas. *Chem. Eng. Sci.* **84**, 580–590 (2012).
- 853 34. Fridman, A. *Plasma chemistry. Plasma Chemistry* vol. 9780521847 (2008).
- 854 35. Maqueo, P. D. G., Maier, M., Evans, M. D. G., Coulombe, S. & Bergthorson, J. M. Regimes of an
855 atmospheric pressure nanosecond repetitively pulsed discharge for methane partial oxidation. *J.*
856 *Phys. D. Appl. Phys.* **51**, (2018).
- 857 36. Zhao, B., Zhang, R., Huang, Z. & Wang, B. Effect of the size of Cu clusters on selectivity and activity
858 of acetylene selective hydrogenation. *Appl. Catal. A Gen.* **546**, 111–121 (2017).
- 859 37. Shi, X. *et al.* Copper Catalysts in Semihydrogenation of Acetylene: From Single Atoms to
860 Nanoparticles. *ACS Catal.* **10**, 3495–3504 (2020).
- 861 38. Saggese, C. *et al.* Kinetic modeling study of polycyclic aromatic hydrocarbons and soot formation in
862 acetylene pyrolysis. *Energy and Fuels* **28**, 1489–1501 (2014).
- 863 39. Martin, A., Cozmuta, I., Wright, M. J. & Boyd, I. D. Kinetic rates for gas-phase chemistry of phenolic-
864 based carbon ablator in atmospheric air. *J. Thermophys. Heat Transf.* **29**, 222–240 (2015).
- 865 40. Butterworth, T. *et al.* Plasma induced vibrational excitation of CH₄ - A window to its mode selective
866 processing. *Plasma Sources Sci. Technol.* **29**, (2020).
- 867 41. Maitre, P. A., Bieniek, M. S. & Kechagiopoulos, P. N. Modelling excited species and their role on
868 kinetic pathways in the non-oxidative coupling of methane by dielectric barrier discharge. *Chem.*
869 *Eng. Sci.* **234**, (2021).
- 870 42. Pourali, N., Hessel, V. & Rebrov, E. V. The Effects of Pulse Shape on the Selectivity and Production
871 Rate in Non-oxidative Coupling of Methane by a Micro-DBD Reactor. *Plasma Chem. Plasma*
872 *Process.* **42**, 619–640 (2022).
- 873

1 **Methane coupling in nanosecond pulsed plasmas: correlation**
2 **between temperature and pressure and effects on product selectivity**

3 Eduardo Morais,^{a†} Evangelos Delikonstantis,^{b,c†} Marco Scapinello,^c Gregory Smith,^a Georgios
4 D. Stefanidis,^{c,d*} Annemie Bogaerts^{a*}

5 ^a PLASMANT, Department of Chemistry, University of Antwerp, Wilrijk-Antwerp 2610, Belgium

6 ^b AristEng S.à r.l., 77, rue de Merl, L-2146, Luxembourg City, Luxembourg

7 ^c Laboratory for Chemical Technology, Ghent University; Tech Lane Ghent Science Park 125, Ghent,
8 B-9052, Belgium

9 ^d School of Chemical Engineering, National Technical University of Athens, Iroon Polytechniou 9,
10 15780, Athens, Greece

11

12

13

14 †The authors have equally contributed to this work

15

16

17

18 *Correspondence to:

Annemie Bogaerts

annemie.bogaerts@uantwerpen.be

Georgios D. Stefanidis

gstefani@mail.ntua.gr

19

20 Supporting Information

21 1. Carbon and hydrogen balance

22 **Table S1** Carbon and hydrogen balance

Pressure (bar)	Carbon recovery (%)	H Recovery (%)
1	90.5	97.1
2	81.0	98.1
3	77.7	94.4
4	74.7	95.4
5	77.2	90.7

23 Carbon and hydrogen recoveries (C_{out}/C_{in} and H_{out}/H_{in}) were calculated on the basis of the
24 chromatographic data of C_2 species produced by the plasma reactor and methane/hydrogen
25 fed into the plasma reactor using the equations below. Heavy species with minor selectivity,
26 *i.e.*, C_3 – C_6 were also formed but not quantified. At higher conversions (2 – 5 bar), carbon and
27 hydrogen balance of ~ 75 – 80% and ~ 90 – 95%, respectively, were calculated. The majority
28 of the missing carbon must be attributed to C_3 or longer hydrocarbons. Based upon the weight
29 of all solid matter collected following the experiment and assuming that it consists of only
30 carbon, about 5 – 10% of the missing carbon is related to the formation of carbon black and
31 other solid carbonaceous products deposited on the reactor wall or collected by the filter.
32

33

$$34 \quad C \text{ recovery} = \frac{v_{out} \times ([CH_4]_{out} + 2 \times ([C_2H_2] + [C_2H_4] + [C_2H_6]))}{v_{in} \times [CH_4]_{in}} \times 100\%$$

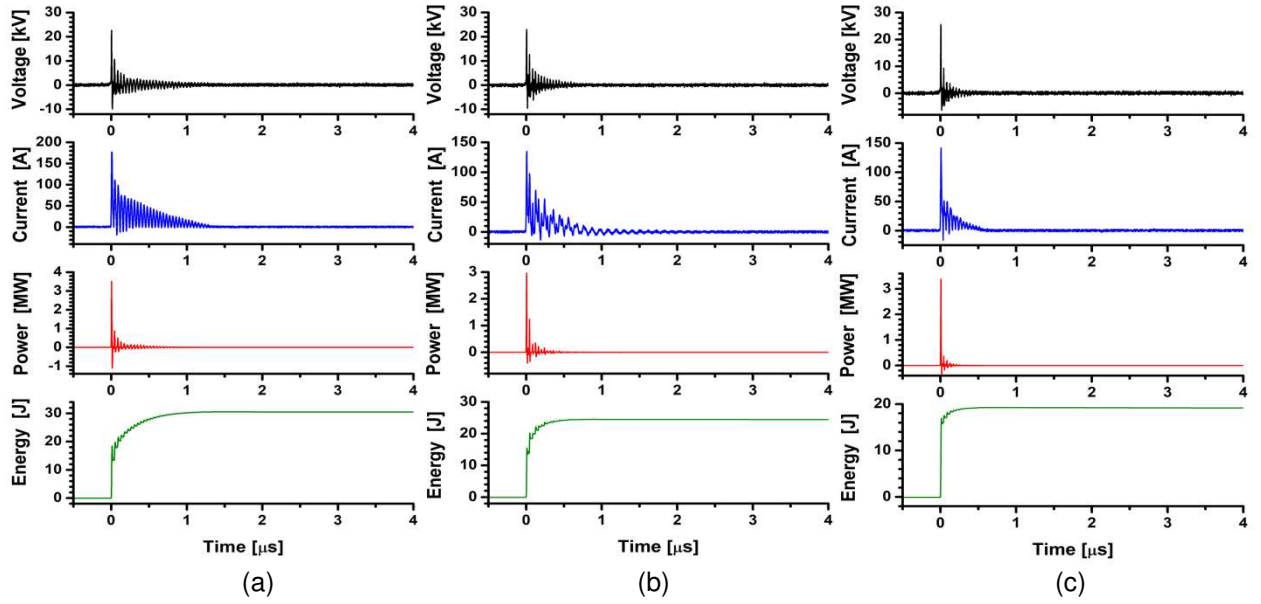
35

$$36 \quad H \text{ recovery} = \frac{v_{out} \times [4 \times ([CH_4]_{out} + [C_2H_4]) + 2 \times ([H_2] + [C_2H_2]) + 6 \times [C_2H_6]]}{4 \times v_{in} \times [CH_4]_{in} + 2 \times v_{in} \times [H_2]_{in}} \times 100\%$$

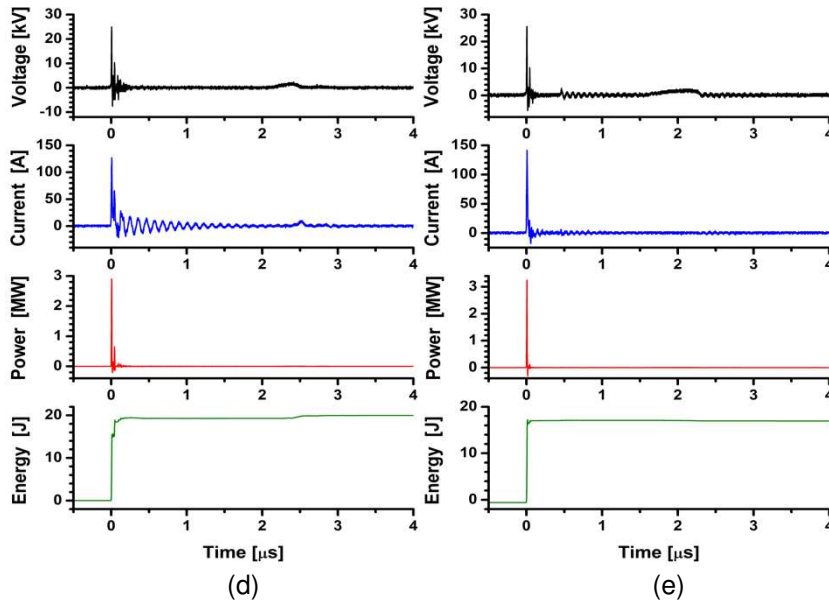
37

38 2. Power deposition characteristics

39 The current and voltage waveforms, power pulses and energy curves of the co-axial reactor
40 operating at applied pressure in the 1 to 5 bar pressure range are presented in Figure S1.



41
42



43
44

45 **Figure S1** Experimental profiles of voltage (black), current (blue), peak of derived instantaneous power
46 (red) and curve of delivered energy (green) at the applied pressures of (a) 1 bar, (b) 2 bar, (c) 3 bar, (d)
47 4 bar and (e) 5 bar. Pulses were generated by the nanosecond pulsed power supply NPG-18/100k,
48 Megaimpulse Ltd. in the co-axial plasma reactor operating at 200 sccm ($\text{CH}_4:\text{H}_2=1:1$ molar basis),
49 discharge gap 2.5 mm, pulse frequency 3 kHz (continuous mode).

50 3. Gas temperature calculations

51 The balance equation to solve the gas temperature in the system is as follows

$$52 \quad N \frac{\gamma k}{\gamma - 1} \frac{dT_{gas}}{dt} = P_{e,el} + \sum_j R_j \Delta H_j - P_{ext}$$

53 where $N = \sum n_i$ is the total neutral species density, γ is the specific heat ratio of the total gas
54 mixture, k is the Boltzmann constant (in J K^{-1}), $P_{e,el}$ is the gas heating power density due to
55 elastic electron-neutral collisions (in W m^{-3}), R_j is the rate of reaction j (in $\text{m}^{-3} \text{s}^{-1}$), ΔH_j is the
56 heat released (or consumed when this value is negative) by reaction j (in Joules) and P_{ext} is

57 the heat loss due to energy exchange with the surroundings (in W m^{-3}). The latter is expressed
 58 by the equation:

$$59 \quad P_{ext} = \frac{8\lambda_{CH_4}}{R^2} (T_{gas} - T_{gas,i}) x_{CH_4} + \frac{8\lambda_{H_2}}{R^2} (T_{gas} - T_{gas,i}) x_{H_2}$$

60 With R being the radius of the plasma zone, T_{gas} the plasma gas temperature and $T_{gas,i}$ the
 61 gas temperature at the edge of the plasma zone, which is assumed to be the average between
 62 room temperature and plasma temperature, according to Berthelot.¹ λ is the gas thermal
 63 conductivity of each gas (in $\text{W cm}^{-1} \text{K}^{-1}$) and x is the fraction of each gas (CH_4 and H_2). The
 64 thermal conductivity of CH_4 and H_2 taken respectively from Hepburn et al.² and Edlmann et
 65 al.³ can be expressed as:

$$66 \quad \lambda_{CH_4} = (1.49 \times 10^{-6}) * T_{gas} - 9.92 \times 10^{-5}$$

$$67 \quad \lambda_{H_2} = (4.90 \times 10^{-6}) * T_{gas} + 3.85 \times 10^{-4}$$

68 It is important to note that the model developed in this study investigates the gas temperature
 69 in the plasma volume confined within the reactor volume. Thus, the gas temperatures
 70 calculated by the model may not reflect the gas temperature in the whole reactor body.
 71 Moreover, the model is concerned with a finite element volume and does not account for
 72 conductive or convective losses in the reactor.

73 4. Vibrational kinetics of H_2

74 Alongside ground state H_2 , 14 vibrational levels of H_2 are included in the model with ascending
 75 energy from the ground state (0 eV) up to the dissociation limit (4.48 eV). The energy of each
 76 level is calculated using the anharmonic oscillator theory for a diatomic molecule, where the
 77 first two vibrational constants, $\omega_e = 4401.213 \text{ cm}^{-1}$ $\omega_e x_e = 121.336 \text{ cm}^{-1}$, of the hydrogen
 78 molecule are used in this work⁴. The energy values are $\text{H}_2 = 0.00 \text{ eV}$, $\text{H}_2(v1) = 0.516 \text{ eV}$,
 79 $\text{H}_2(v2) = 1.001 \text{ eV}$, $\text{H}_2(v3) = 1.457 \text{ eV}$, $\text{H}_2(v4) = 1.882 \text{ eV}$, $\text{H}_2(v5) = 2.277 \text{ eV}$, $\text{H}_2(v6) = 2.642$
 80 eV , $\text{H}_2(v7) = 2.977 \text{ eV}$, $\text{H}_2(v8) = 3.282 \text{ eV}$, $\text{H}_2(v9) = 3.557 \text{ eV}$, $\text{H}_2(v10) = 3.802 \text{ eV}$, $\text{H}_2(v11) =$
 81 4.017 eV , $\text{H}_2(v12) = 4.201 \text{ eV}$, $\text{H}_2(v13) = 4.356 \text{ eV}$ and $\text{H}_2(v14) = 4.480 \text{ eV}$.

82 (a) VV-relaxation between H_2 molecules

83 The rate coefficient of $\text{H}_2\text{-H}_2$ relaxation processes of vibrationally excited states, i.e.,
 84 $\text{H}_2(v+1) + \text{H}_2(w) \rightarrow \text{H}_2(v) + \text{H}_2(w+1)$, were scaled with the approach proposed by
 85 Matveyev and Silakov,⁵ and Loureiro and Ferreira.⁶ In this approach, the rate coefficient of the
 86 lowest levels $k_{1,0}^{0,1}$ (in $\text{cm}^3 \text{s}^{-1}$) is used to determine the rate coefficient of reactions involving
 87 higher levels $k_{v+1,v}^{w,w+1}$:

$$88 \quad k_{v+1,v}^{w,w+1} = k_{1,0}^{0,1} (v+1)(w+1) \left[\frac{3}{2} - \frac{1}{2} \exp(-\delta(w-v)) \right] \exp[\Delta_1(w-v) - \Delta_2(w-v)^2] \quad w > v$$

89 With $k_{1,0}^{0,1} = 4.23 \times 10^{-15} \left(\frac{300}{T_{gas}}\right)^{\frac{1}{3}}$, $\delta = 0.21 \sqrt{\left(\frac{T_{gas}}{300}\right)}$, $\Delta_1 = 0.236 \left(\frac{T_{gas}}{300}\right)^{\frac{1}{4}}$ and $\Delta_2 = 0.0572 \left(\frac{300}{T_{gas}}\right)^{\frac{1}{3}}$

90 Detailed balance is then applied to this equation to calculate reverse reaction rates.

91 (b) VT-relaxation of H₂ molecules

92 For VT relaxation processes, i.e, $H_2(v) + M \rightarrow H_2(v \pm 1) + M$, we also employed the
 93 approach proposed by Matveyev and Silakov,⁵ in which the rate coefficient of $k_{v,v-1}$ levels
 94 (upon VT relaxation from higher levels) can be determined using the rate coefficient of the $k_{1,0}$
 95 process, or the $H_2(v1) + M \rightarrow H_2 + M$ reaction.

$$96 \quad k_{v,v-1} = k_{1,0} v \exp \left[0.97 \left(\frac{300}{T_{gas}}\right)^{\frac{1}{3}} (v-1) \right]$$

97 The rate expression of $k_{1,0}$ is taken from Capitelli et al.⁷

$$98 \quad k_{1,0} = 7.47 \times 10^{-12} T_{gas}^{0.50} \exp \left(-93.87 T_{gas}^{-\frac{1}{3}} \right) \left[1 - \exp \left(-\frac{E_{1,0}}{T_{gas}} \right) \right]^{-1}$$

99 With $E_{1,0} = 5983 \text{ K}$. The reverse processes are included using detailed balance.

100 The H₂ VT reactions in which H atoms are collision partners, $H_2(v) + H \rightarrow H_2(v \pm 1) + H$,
 101 are divided into two distinct processes, one of non-reactive character (i) and another of
 102 reactive character (ii), depending on the occurrence (ii) or not (i) of atomic exchange between
 103 the H₂ and H species. These reactions were described by Gorse et al.⁸ for $w < v < 10$ and
 104 the proposed rate coefficient is:

$$105 \quad k = A_{nr} \exp \left(-\frac{E_{a,nr}}{T_{gas}} \right) + A_r \exp \left(-\frac{E_{a,r}}{T_{gas}} \right)$$

106 Where the pre-exponential factors A_{nr} and A_r (in cm³ s⁻¹) and activation energies $E_{a,nr}$ and
 107 $E_{a,r}$ (in K) are given in Gorse et al. for the relaxation reactions from all levels $v < 10$ to all
 108 levels $w \leq v - 1$.

109 5. Vibrational kinetics of CH₄

110 The lowest energy level of the four degenerate vibrational modes of CH₄ are considered in the
 111 model: the v_1 singly degenerate symmetric stretch mode (at 0.362 eV), the v_2 doubly
 112 degenerate scissoring bend mode (at 0.190 eV), the v_3 triply degenerate asymmetric stretch
 113 mode (at 0.374 eV) and the v_4 triply degenerate umbrella bend mode (at 0.162 eV).⁹ The
 114 relaxation processes between these modes were studied by Menard-Bourcin et al.¹⁰ who
 115 determined the reaction rates at gas temperature of 193 and 296 K. Based on earlier works of
 116 Capitelli et al.,⁷ Wang and Springer¹¹ and Richards and Sigafos,¹² it is possible to express

117 the rate constants of these relaxation processes at any given gas temperatures T_1 and T_2 (in
 118 Kelvin, $T_1 > T_2$) as follows

$$119 \frac{k_{T_2}}{k_{T_1}} = \exp\left(-\alpha T_2^{-\left(\frac{1}{3}\right)} + \alpha T_1^{-\left(\frac{1}{3}\right)}\right)$$

120 Where k_{T_1} and k_{T_2} are the rate coefficients (in $\text{cm}^3 \text{s}^{-1}$) at gas temperatures T_1 and T_2 and α is
 121 a constant derived from the rates calculated by Menard-Bourcin et al. at 193 and 296 K. The
 122 reverse reactions are also included in the model and their rate coefficients were defined by
 123 the detailed balance approach suggested by Menard-Bourcin et al.¹⁰

124 6. Full chemistry of CH_4 and H_2

125 The chemical reactions included in the model are divided in different types and are listed in
 126 the tables below.

127 **Table S2** Electron impact reactions with neutral species and corresponding rate coefficients. The rate
 128 coefficients are evaluated using cross section data $f(\sigma)$, or an analytical expression with T_{gas} and T_e in
 129 Kelvin. The rate coefficients for two-body and three-body reactions are given in $\text{cm}^3 \text{s}^{-1}$ or $\text{cm}^6 \text{s}^{-1}$,
 130 respectively. References are shown in the last column.

$e^- + \text{CH}_4 \rightarrow e^- + \text{CH}_4$	$f(\sigma)$	IST Lisbon database - Lxcat net
$e^- + \text{CH}_4(v1 - v4) \leftrightarrow e^- + \text{CH}_4(v1 - v4)$	$f(\sigma)$	13
$e^- + \text{CH}_3 \rightarrow e^- + \text{CH}_3$	$f(\sigma)$	IST Lisbon database - Lxcat net
$e^- + \text{CH}_2 \rightarrow e^- + \text{CH}_2$	$f(\sigma)$	IST Lisbon database - Lxcat net
$e^- + \text{CH} \rightarrow e^- + \text{CH}$	$f(\sigma)$	IST Lisbon database - Lxcat net
$e^- + \text{C} \rightarrow e^- + \text{C}$	$f(\sigma)$	IST Lisbon database - Lxcat net
$e^- + \text{C}_s \rightarrow e^- + \text{C}_s$	$f(\sigma)$	IST Lisbon database - Lxcat net
$e^- + \text{C}_2\text{H}_6 \rightarrow e^- + \text{C}_2\text{H}_6$	$f(\sigma)$	IST Lisbon database - Lxcat net
$e^- + \text{C}_2\text{H}_5 \rightarrow e^- + \text{C}_2\text{H}_5$	$f(\sigma)$	IST Lisbon database - Lxcat net
$e^- + \text{C}_2\text{H}_4 \rightarrow e^- + \text{C}_2\text{H}_4$	$f(\sigma)$	IST Lisbon database - Lxcat net
$e^- + \text{C}_2\text{H}_3 \rightarrow e^- + \text{C}_2\text{H}_3$	$f(\sigma)$	IST Lisbon database - Lxcat net
$e^- + \text{C}_2\text{H}_2 \rightarrow e^- + \text{C}_2\text{H}_2$	$f(\sigma)$	IST Lisbon database - Lxcat net
$e^- + \text{C}_2\text{H} \rightarrow e^- + \text{C}_2\text{H}$	$f(\sigma)$	IST Lisbon database - Lxcat net
$e^- + \text{C}_3\text{H}_8 \rightarrow e^- + \text{C}_3\text{H}_8$	$f(\sigma)$	IST Lisbon database - Lxcat net
$e^- + \text{C}_3\text{H}_7 \rightarrow e^- + \text{C}_3\text{H}_7$	$f(\sigma)$	IST Lisbon database - Lxcat net
$e^- + \text{C}_3\text{H}_6 \rightarrow e^- + \text{C}_3\text{H}_6$	$f(\sigma)$	IST Lisbon database - Lxcat net
$e^- + \text{C}_3\text{H}_5 \rightarrow e^- + \text{C}_3\text{H}_5$	$f(\sigma)$	IST Lisbon database - Lxcat net

$e^- + H \rightarrow e^- + H$	f(σ)	IST Lisbon database - Lxcat net
$e^- + H_2 \rightarrow e^- + H_2$	f(σ)	IST Lisbon database - Lxcat net
$e^- + H_2(v1 - 14) \leftrightarrow e^- + H_2(v1 - 14)$	f(σ)	14
$e^- + H_2^* \rightarrow e^- + H_2^*$	f(σ)	IST Lisbon database - Lxcat net
$e^- + CH_4(v) \leftrightarrow e^- + CH_4(w)$	f(σ)	13
$e^- + CH_4 \rightarrow CH_2^- + H_2$	f(σ)	IST Lisbon database - Lxcat net
$e^- + CH \rightarrow CH^-$	f(σ)	Itikawa database - Lxcat net
$e^- + H_2 \rightarrow e^- + H_2(v1 - 14)$	f(σ)	14
$e^- + H_2(v) \leftrightarrow e^- + H_2(w)$	f(σ)	14
$e^- + H_2 \rightarrow e^- + H_2^*$	f(σ)	IST Lisbon database - Lxcat net
$e^- + CH_4 \rightarrow e^- + e^- + CH_4^+$	f(σ)	15
$e^- + CH_4 \rightarrow e^- + e^- + CH_3^+ + H$	f(σ)	15
$e^- + CH_4 \rightarrow e^- + e^- + CH_2^+ + H_2$	f(σ)	15
$e^- + CH_4 \rightarrow e^- + CH_3 + H$	f(σ)	15
$e^- + CH_4 \rightarrow e^- + CH_2 + H_2$	f(σ)	15
$e^- + CH_4 \rightarrow e^- + CH_2 + H + H$	f(σ)	15
$e^- + CH_4 \rightarrow e^- + CH + H_2 + H$	f(σ)	15
$e^- + CH_4 \rightarrow e^- + C + H_2 + H_2$	f(σ)	15
$e^- + CH_3 \rightarrow e^- + e^- + CH_3^+$	f(σ)	15
$e^- + CH_3 \rightarrow e^- + e^- + CH_2^+ + H$	f(σ)	15
$e^- + CH_3 \rightarrow e^- + e^- + CH^+ + H_2$	f(σ)	15
$e^- + CH_3 \rightarrow e^- + CH_2 + H$	f(σ)	15
$e^- + CH_3 \rightarrow e^- + CH + H_2$	f(σ)	15
$e^- + CH_3 \rightarrow e^- + C + H_2 + H$	f(σ)	15
$e^- + CH_2 \rightarrow e^- + e^- + CH_2^+$	f(σ)	15
$e^- + CH_2 \rightarrow e^- + CH + H$	f(σ)	15
$e^- + CH_2 \rightarrow e^- + C + H_2$	f(σ)	15
$e^- + CH_2 \rightarrow e^- + C + H + H$	f(σ)	15
$e^- + CH \rightarrow e^- + e^- + CH^+$	f(σ)	15
$e^- + CH \rightarrow e^- + C + H$	f(σ)	15
$e^- + C_2H_6 \rightarrow e^- + e^- + C_2H_6^+$	f(σ)	15
$e^- + C_2H_5 \rightarrow e^- + e^- + C_2H_5^+$	f(σ)	15
$e^- + C_2H_4 \rightarrow e^- + e^- + C_2H_4^+$	f(σ)	15
$e^- + C_2H_3 \rightarrow e^- + e^- + C_2H_3^+$	f(σ)	15
$e^- + C_2H_2 \rightarrow e^- + e^- + C_2H_2^+$	f(σ)	15
$e^- + C_2H_6 \rightarrow e^- + e^- + C_2H_5^+ + H$	f(σ)	15
$e^- + C_2H_6 \rightarrow e^- + e^- + C_2H_4^+ + H_2$	f(σ)	15
$e^- + C_2H_6 \rightarrow 2e^- + C_2H_3^+ + H_2 + H$	f(σ)	15
$e^- + C_2H_6 \rightarrow e^- + e^- + C_2H_2^+ + 2H_2$	f(σ)	15
$e^- + C_2H_6 \rightarrow e^- + e^- + CH_3^+ + CH_3$	f(σ)	15
$e^- + C_2H_5 \rightarrow e^- + e^- + C_2H_4^+ + H$	f(σ)	15
$e^- + C_2H_5 \rightarrow e^- + e^- + C_2H_3^+ + H_2$	f(σ)	15
$e^- + C_2H_5 \rightarrow 2e^- + C_2H_2^+ + H_2 + H$	f(σ)	15
$e^- + C_2H_4 \rightarrow e^- + e^- + C_2H_3^+ + H$	f(σ)	15
$e^- + C_2H_4 \rightarrow e^- + e^- + C_2H_2^+ + H_2$	f(σ)	15
$e^- + C_2H_3 \rightarrow e^- + e^- + C_2H_2^+ + H$	f(σ)	15
$e^- + C_2H_6 \rightarrow e^- + C_2H_5 + H$	f(σ)	15
$e^- + C_2H_6 \rightarrow e^- + C_2H_4 + H_2$	f(σ)	15
$e^- + C_2H_6 \rightarrow e^- + C_2H_3 + H_2 + H$	f(σ)	15
$e^- + C_2H_6 \rightarrow e^- + C_2H_2 + 2H_2$	f(σ)	15

$e^- + C_2H_6 \rightarrow e^- + CH_4 + CH_2$	f(σ)	15
$e^- + C_2H_6 \rightarrow e^- + CH_3 + CH_3$	f(σ)	15
$e^- + C_2H_5 \rightarrow e^- + C_2H_4 + H$	f(σ)	15
$e^- + C_2H_5 \rightarrow e^- + C_2H_3 + H_2$	f(σ)	15
$e^- + C_2H_5 \rightarrow e^- + C_2H_3 + 2H$	f(σ)	15
$e^- + C_2H_5 \rightarrow e^- + C_2H_2 + H_2 + H$	f(σ)	15
$e^- + C_2H_5 \rightarrow e^- + C_2H + 2H_2$	f(σ)	15
$e^- + C_2H_5 \rightarrow e^- + CH_4 + CH$	f(σ)	15
$e^- + C_2H_5 \rightarrow e^- + CH_3 + CH_2$	f(σ)	15
$e^- + C_2H_4 \rightarrow e^- + C_2H_3 + H$	f(σ)	15
$e^- + C_2H_4 \rightarrow e^- + C_2H_2 + H_2$	f(σ)	15
$e^- + C_2H_4 \rightarrow e^- + C_2H_2 + 2H$	f(σ)	15
$e^- + C_2H_4 \rightarrow e^- + C_2H + H_2 + H$	f(σ)	15
$e^- + C_2H_4 \rightarrow e^- + CH_3 + CH$	f(σ)	15
$e^- + C_2H_4 \rightarrow e^- + CH_2 + CH_2$	f(σ)	15
$e^- + C_2H_4 \rightarrow e^- + C + CH_4$	f(σ)	15
$e^- + C_2H_3 \rightarrow e^- + C_2H + H + H$	f(σ)	15
$e^- + C_2H_3 \rightarrow e^- + C_2 + H_2 + H$	f(σ)	15
$e^- + C_2H_3 \rightarrow e^- + CH_2 + CH$	f(σ)	15
$e^- + C_2H_3 \rightarrow e^- + C + CH_3$	f(σ)	15
$e^- + C_2H_2 \rightarrow e^- + C_2H + H$	f(σ)	15
$e^- + C_2H_2 \rightarrow e^- + C_2 + H_2$	f(σ)	15
$e^- + C_2H_2 \rightarrow e^- + C_2 + 2H$	f(σ)	15
$e^- + C_2H_2 \rightarrow e^- + CH + CH$	f(σ)	15
$e^- + C_2H_2 \rightarrow e^- + C + CH_2$	f(σ)	15
$e^- + C_2H \rightarrow e^- + C_2 + H$	f(σ)	15
$e^- + C_2H \rightarrow e^- + C + CH$	f(σ)	15
$e^- + C_3H_8 \rightarrow e^- + e^- + C_2H_5^+ + CH_3$	f(σ)	15
$e^- + C_3H_8 \rightarrow e^- + e^- + C_2H_4^+ + CH_4$	f(σ)	15
$e^- + C_3H_7 \rightarrow e^- + e^- + C_2H_5^+ + CH_2$	f(σ)	15
$e^- + C_3H_7 \rightarrow e^- + e^- + C_2H_4^+ + CH_3$	f(σ)	15
$e^- + C_3H_7 \rightarrow e^- + e^- + C_2H_3^+ + CH_4$	f(σ)	15
$e^- + C_3H_7 \rightarrow e^- + e^- + CH_3^+ + C_2H_4$	f(σ)	15
$e^- + C_3H_6 \rightarrow e^- + e^- + C_2H_5^+ + CH$	f(σ)	15
$e^- + C_3H_6 \rightarrow e^- + e^- + C_2H_4^+ + CH_2$	f(σ)	15
$e^- + C_3H_6 \rightarrow e^- + e^- + C_2H_3^+ + CH_3$	f(σ)	15
$e^- + C_3H_6 \rightarrow e^- + e^- + C_2H_2^+ + CH_4$	f(σ)	15
$e^- + C_3H_6 \rightarrow e^- + e^- + CH_3^+ + C_2H_3$	f(σ)	15
$e^- + C_3H_5 \rightarrow e^- + e^- + C_2H_3^+ + CH_2$	f(σ)	15
$e^- + C_3H_5 \rightarrow e^- + e^- + C_2H_2^+ + CH_3$	f(σ)	15
$e^- + C_3H_5 \rightarrow e^- + e^- + CH_3^+ + C_2H_2$	f(σ)	15
$e^- + C_3H_8 \rightarrow e^- + C_3H_7 + H$	f(σ)	15
$e^- + C_3H_8 \rightarrow e^- + C_3H_6 + H_2$	f(σ)	15
$e^- + C_3H_8 \rightarrow e^- + C_2H_4 + CH_4$	f(σ)	15
$e^- + C_3H_8 \rightarrow e^- + C_2H_6 + CH_2$	f(σ)	15
$e^- + C_3H_8 \rightarrow e^- + C_2H_5 + CH_3$	f(σ)	15
$e^- + C_3H_7 \rightarrow e^- + C_3H_6 + H$	f(σ)	15
$e^- + C_3H_7 \rightarrow e^- + C_2H_4 + CH_3$	f(σ)	15
$e^- + C_3H_7 \rightarrow e^- + C_2H_3 + CH_4$	f(σ)	15
$e^- + C_3H_7 \rightarrow e^- + C_3H_5 + H_2$	f(σ)	15
$e^- + C_3H_6 \rightarrow e^- + C_2H_2 + CH_4$	f(σ)	15
$e^- + C_3H_6 \rightarrow e^- + C_3H_5 + H$	f(σ)	15
$e^- + C_3H_6 \rightarrow e^- + C_2H_3 + CH_3$	f(σ)	15
$e^- + C_3H_6 \rightarrow e^- + C_2H_4 + CH_2$	f(σ)	15

$e^- + C_3H_5 \rightarrow e^- + C_2H_2 + CH_3$	f(σ)	15
$e^- + C_3H_5 \rightarrow e^- + C_2H + CH_4$	f(σ)	15
$e^- + H_2 \rightarrow e^- + H + H$	f(σ)	16
$e^- + H_2(v1 - 14) \rightarrow e^- + H + H$	f(σ)	16
$e^- + H_2^* \rightarrow e^- + H + H$	f(σ)	16
$e^- + H_2 \rightarrow e^- + e^- + H_2^+$	f(σ)	16
$e^- + H_2(v1 - 14) \rightarrow e^- + e^- + H_2^+$	f(σ)	16
$e^- + H_2^* \rightarrow e^- + e^- + H_2^+$	f(σ)	16
$e^- + H^+ \rightarrow H$	See reference	17
$e^- + H_3^+ \rightarrow H_2 + H$	f(σ)	18,19
$e^- + H_3^+ \rightarrow e^- + H_2 + H^+$	f(σ)	18,19
$e^- + H_3^+ \rightarrow H + H + H$	f(σ)	18,19
$e^- + H_2^+ \rightarrow e^- + H + H^+$	f(σ)	17
$e^- + H_3^+ \rightarrow e^- + H + H + H^+$	f(σ)	18,19
$e^- + H \rightarrow e^- + e^- + H^+$	f(σ)	IST Lisbon database - Lxcat net
$e^- + H^- \rightarrow e^- + e^- + H$	f(σ)	Itikawa database - Lxcat net
$e^- + CH_4 \rightarrow CH_3 + H^-$	f(σ)	Itikawa database - Lxcat net
$e^- + CH_4 \rightarrow CH_2^- + H_2$	f(σ)	IST Lisbon database - Lxcat net
$e^- + H_2 \rightarrow H + H^-$	f(σ)	Itikawa database - Lxcat net
$e^- + H_2(v1 - 14) \rightarrow H + H^-$	f(σ)	IST Lisbon database - Lxcat net
$e^- + H_2^* \rightarrow H + H^-$	f(σ)	Itikawa database - Lxcat net
$e^- + CH_4 \rightarrow CH_2^- + H_2$	f(σ)	Itikawa database - Lxcat net
$e^- + H_2^+ \rightarrow H + H$	See reference	17
$e^- + C \rightarrow e^- + e^- + C^+$	f(σ)	IST Lisbon database - Lxcat net
$e^- + C_2 \rightarrow e^- + e^- + C_2^+$	f(σ)	15
$e^- + C_2 \rightarrow e^- + C + C$	f(σ)	15
$e^- + C_2^+ \rightarrow e^- + C^+ + C$	f(σ)	15
$e^- + C_2^+ \rightarrow C + C$	f(σ)	15
$e^- + C_3 \rightarrow e^- + C_2 + C$	f(σ)	15
$e^- + C_3 \rightarrow e^- + C + C + C$	f(σ)	15
$e^- + CH_5^+ \rightarrow CH_3 + H + H$	$2.57 \times 10^{-7} T_e^{-0.30}$	15,20
$e^- + CH_5^+ \rightarrow CH_2 + H_2 + H$	$6.61 \times 10^{-8} T_e^{-0.30}$	15,20
$e^- + CH_4^+ \rightarrow CH_3 + H$	$3.50 \times 10^{-7} T_e^{-0.50}$	15,20
$e^- + CH_4^+ \rightarrow CH_2 + H + H$	$3.50 \times 10^{-7} T_e^{-0.50}$	15,20
$e^- + CH_4^+ \rightarrow CH + H_2 + H$	$1.41 \times 10^{-7} T_e^{-0.50}$	15,20
$e^- + CH_3^+ \rightarrow CH_2 + H$	$3.50 \times 10^{-7} T_e^{-0.50}$	15,20
$e^- + CH_3^+ \rightarrow CH + H_2$	$7.88 \times 10^{-8} T_e^{-0.50}$	15,20
$e^- + CH_3^+ \rightarrow CH + H + H$	$9.00 \times 10^{-8} T_e^{-0.50}$	15,20
$e^- + CH_3^+ \rightarrow C + H_2 + H$	$1.69 \times 10^{-7} T_e^{-0.50}$	15,20
$e^- + CH_2^+ \rightarrow CH + H$	$6.25 \times 10^{-8} T_e^{-0.50}$	15,20
$e^- + CH_2^+ \rightarrow C + H_2$	$5.78 \times 10^{-9} T_e^{-0.50}$	15,20
$e^- + CH_2^+ \rightarrow C + H + H$	$1.59 \times 10^{-9} T_e^{-0.50}$	15,20
$e^- + CH^+ \rightarrow C + H$	$2.53 \times 10^{-7} T_e^{-0.50}$	15,20
$e^- + C_2H_6^+ \rightarrow C_2H_5 + H$	$2.19 \times 10^{-8} T_e^{-0.71}$	21
$e^- + C_2H_6^+ \rightarrow C_2H_4 + H + H$	$3.36 \times 10^{-8} T_e^{-0.71}$	21
$e^- + C_2H_5^+ \rightarrow C_2H_4 + H$	$7.70 \times 10^{-9} T_e^{-0.71}$	21
$e^- + C_2H_5^+ \rightarrow C_2H_3 + H + H$	$1.92 \times 10^{-8} T_e^{-0.71}$	21
$e^- + C_2H_5^+ \rightarrow C_2H_2 + H_2 + H$	$1.60 \times 10^{-8} T_e^{-0.71}$	21

$e^- + C_2H_5^+ \rightarrow C_2H_2 + H + H + H$	$8.98 \times 10^{-9} T_e^{-0.71}$	21
$e^- + C_2H_5^+ \rightarrow CH_3 + CH_2$	$9.62 \times 10^{-9} T_e^{-0.71}$	21
$e^- + C_2H_4^+ \rightarrow C_2H_3 + H$	$6.16 \times 10^{-8} T_e^{-0.76}$	21
$e^- + C_2H_4^+ \rightarrow C_2H_2 + H_2$	$3.36 \times 10^{-8} T_e^{-0.76}$	21
$e^- + C_2H_4^+ \rightarrow C_2H_2 + H + H$	$3.70 \times 10^{-7} T_e^{-0.71}$	21
$e^- + C_2H_4^+ \rightarrow C_2H + H_2 + H$	$5.60 \times 10^{-8} T_e^{-0.76}$	21
$e^- + C_2H_4^+ \rightarrow CH_3 + CH$	$1.12 \times 10^{-8} T_e^{-0.76}$	21
$e^- + C_2H_4^+ \rightarrow CH_2 + CH_2$	$2.24 \times 10^{-8} T_e^{-0.76}$	21
$e^- + C_2H_3^+ \rightarrow C_2H_2 + H$	$1.45 \times 10^{-7} T_e^{-0.84}$	21
$e^- + C_2H_3^+ \rightarrow C_2H + H + H$	$2.95 \times 10^{-7} T_e^{-0.84}$	21
$e^- + C_2H_3^+ \rightarrow C_2 + H + H_2$	$2.87 \times 10^{-8} T_e^{-1.38}$	21
$e^- + C_2H_3^+ \rightarrow C_2H + H_2$	$3.00 \times 10^{-8} T_e^{-0.84}$	21
$e^- + C_2H_3^+ \rightarrow CH_2 + CH$	$1.50 \times 10^{-8} T_e^{-0.84}$	21
$e^- + C_2H_2^+ \rightarrow C_2H + H$	$9.00 \times 10^{-8} T_e^{-0.50}$	21
$e^- + C_2H_2^+ \rightarrow CH + CH$	$9.00 \times 10^{-8} T_e^{-0.50}$	21
$e^- + C_2H_2^+ \rightarrow C_2 + H + H$	$9.00 \times 10^{-8} T_e^{-0.50}$	21
$e^- + C_2H^+ \rightarrow C_2 + H$	$1.16 \times 10^{-7} T_e^{-0.76}$	21
$e^- + C_2H^+ \rightarrow CH + C$	$1.53 \times 10^{-7} T_e^{-0.76}$	21

131

132 **Table S3** Neutral-neutral pressure-dependent recombination reactions with low pressure (k_0) and high
133 pressure (k_∞) limit rate coefficients. T_{gas} is given in units of Kelvin. The respective rate coefficients (in
134 $cm^3 s^{-1}$) k_0 and k_∞ of each reaction are also given alongside the falloff curve expression (F_C) which
135 incorporates the Troe parameters. k_0 , k_∞ and F_C were used to calculate the rate coefficients of pressure
136 dependent reactions (see details in ²²). References are shown in the last column.

$CH_3 + H \rightarrow CH_4$	$k_0 = 1.0 \times 10^{-26} * \exp\left(-\frac{T_{gas}}{21220}\right)^2$ $k_\infty = (3.34 \times 10^{-10}) * \left(\frac{T_{gas}}{298.15}\right)^{-0.186} * \exp\left(-\frac{T_{gas}}{25200}\right)$ $F_C = (0.710) * \exp\left(-\frac{T_{gas}}{3079}\right) + 0.290 * \exp\left(-\frac{T_{gas}}{54}\right)$	23
$CH_3 + CH_3 \rightarrow C_2H_6$	$k_0 = (3.50 \times 10^{-7}) * (T_{gas})^{-7.0} * \exp\left(-\frac{1390}{T_{gas}}\right)$ $k_\infty = (6.00 \times 10^{-11})$ $F_C = 0.381 * \exp\left(-\frac{T_{gas}}{73}\right) + 0.619 * \exp\left(-\frac{T_{gas}}{1180}\right)$	24
$CH_3 + C_2H_5 \rightarrow C_3H_8$	$k_0 = (7.50 \times 10^{-17}) * (T_{gas})^{-3.0} * \exp\left(-\frac{300}{T_{gas}}\right)$ $k_\infty = 6.64 \times 10^{-11}$ $F_C = (1 - 0.153) * \exp\left(-\frac{T_{gas}}{291}\right) + 0.153 * \exp\left(-\frac{T_{gas}}{2742}\right) + \exp\left(-\frac{7748}{T_{gas}}\right)$	22
$CH_2 + H \rightarrow CH_3$	$k_0 = (9.00 \times 10^{-32}) * \exp\left(-\frac{550}{T_{gas}}\right)$ $k_\infty = (8.55 \times 10^{-12}) * (T_{gas})^{0.15}$ $F_C = (1 - 0.562) * \exp\left(-\frac{T_{gas}}{91}\right) + 0.562 * \exp\left(-\frac{T_{gas}}{5836}\right) + \exp\left(-\frac{8552}{T_{gas}}\right)$	24
$CH + H_2 \rightarrow CH_3$	$k = (4.70 \times 10^{-26}) * T_{gas}^{-1.60}$	24

	$k_{\infty} = (8.50 \times 10^{-11}) * (T_{gas})^{0.15}$ $F_C = (1 - 0.578) + \left(0.25 * \exp\left(-\frac{T_{gas}}{300}\right)\right)$	
$H + C_2H_4 \rightarrow C_2H_5$	$k_0 = (1.30 \times 10^{-29}) * \exp\left(-\frac{380}{T_{gas}}\right)$ $k_{\infty} = (6.60 \times 10^{-15}) * (T_{gas})^{1.28} * \exp\left(-\frac{650}{T_{gas}}\right)$ $F_C = (0.240) * \exp\left(-\frac{T_{gas}}{40}\right) + 0.760 * \exp\left(-\frac{T_{gas}}{1025}\right)$	22
$C_2H_4 \rightarrow C_2H_2 + H_2$	$k_0 = (1.70 \times 10^{-6}) * T_{gas} * \exp\left(-\frac{39390}{T_{gas}}\right)$ $k_{\infty} = (8.00 \times 10^{12}) * (T_{gas})^{0.44} * \exp\left(-\frac{88770}{T_{gas}}\right)$ $F_C = (1 - 0.735) * \exp\left(-\frac{T_{gas}}{180}\right) + 0.735 * \exp\left(-\frac{T_{gas}}{1035}\right) + \exp\left(-\frac{5417}{T_{gas}}\right)$	22
$H + C_2H_5 \rightarrow C_2H_6$	$k_0 = (4.00 \times 10^{-19}) * (T_{gas})^{-3.00} * \exp\left(-\frac{600}{T_{gas}}\right)$ $k_{\infty} = (2.00 \times 10^{-10})$ $F_C = (1 - 0.842) * \exp\left(-\frac{T_{gas}}{125}\right) + 0.842 * \exp\left(-\frac{T_{gas}}{2219}\right) + \exp\left(-\frac{6682}{T_{gas}}\right)$	22
$H + C_2H_3 \rightarrow C_2H_4$	$k_0 = 1.75 \times 10^{-27} * (T_{gas})^{-0.347}$ $k_{\infty} = 7.05 \times 10^{-11} * (T_{gas})^{0.180}$ $F_C = 0.0506 * (T_{gas})^{0.40}$	22
$H + C_2H_2 \rightarrow C_2H_3$	$k_0 = (1.60 \times 10^{-20}) * (T_{gas})^{-3.47} * \exp\left(-\frac{475}{T_{gas}}\right)$ $k_{\infty} = (9.20 \times 10^{-16}) * (T_{gas})^{1.64} * \exp\left(-\frac{1055}{T_{gas}}\right)$ $F_C = 7.94 \times 10^{-4} * (T_{gas})^{0.78}$	22
$H + C_3H_7 \rightarrow C_3H_8$	$k_0 = (4.00 \times 10^{-19}) * (T_{gas})^{-3.00} * \exp\left(-\frac{600}{T_{gas}}\right)$ $K_{\infty} = (2.49 \times 10^{-10})$ $F_C = (1 - 0.315) * \exp\left(-\frac{T_{gas}}{369}\right) + 0.315 * \exp\left(-\frac{T_{gas}}{3285}\right) + \exp\left(-\frac{6667}{T_{gas}}\right)$	22
$H + C_2H \rightarrow C_2H_2$	$k_0 = (1.26 \times 10^{-18}) * (T_{gas})^{-3.10} * \exp\left(-\frac{721}{T_{gas}}\right)$ $k_{\infty} = (3.00 \times 10^{-10})$ $F_C = (1 - 0.646) * \exp\left(-\frac{T_{gas}}{132}\right) + 0.65 * \exp\left(-\frac{T_{gas}}{1315}\right) + \exp\left(-\frac{5566}{T_{gas}}\right)$	22
$C_2H_6 \rightarrow CH_3 + CH_3$	$k_0 = (2.60 \times 10^{25}) * (T_{gas})^{-8.37} * \exp\left(-\frac{47290}{T_{gas}}\right)$ $k_{\infty} = (4.50 \times 10^{21}) * (T_{gas})^{-1.37} * \exp\left(-\frac{45900}{T_{gas}}\right)$	22

	$F_C = (0.38) * \exp\left(-\frac{T_{gas}}{73}\right) + 0.62 * \exp\left(-\frac{T_{gas}}{1180}\right)$	
$CH_4 \rightarrow H + CH_3$	$k_0 = (1.40 \times 10^{-6}) * \exp\left(-\frac{45700}{T_{gas}}\right)$ $k_\infty = (2.40 \times 10^{16}) * \exp\left(-\frac{52800}{T_{gas}}\right)$ $F_C = (0.31) * \exp\left(-\frac{T_{gas}}{91}\right) + 0.69 * \exp\left(-\frac{T_{gas}}{2207}\right)$	23
$C_2H_3 \rightarrow C_2H_2 + H$	$k = (4.30 \times 10^3) * (T_{gas})^{-3.40} * \exp\left(-\frac{18020}{T_{gas}}\right)$ $k_\infty = (3.90 \times 10^8) * (T_{gas})^{1.62} * \exp\left(-\frac{18650}{T_{gas}}\right)$ $F_C = (7.37 \times 10^{-4}) * (T_{gas})^{0.80}$	22
$C_2H_5 \rightarrow C_2H_4 + H$	$K_0 = (1.70 \times 10^{-6}) * \exp\left(-\frac{16800}{T_{gas}}\right)$ $K_\infty = (8.20 \times 10^{13}) * \exp\left(-\frac{20070}{T_{gas}}\right)$ $F_C = (0.25) * \exp\left(-\frac{T_{gas}}{97}\right) + 0.75 * \exp\left(-\frac{T_{gas}}{1379}\right)$	22
$C_3H_7 \rightarrow C_3H_6 + H$	$k_0 = (3.56 \times 10^{-7}) * \exp\left(-\frac{14200}{T_{gas}}\right)$ $k_\infty = (8.76 \times 10^7) * (T_{gas})^{1.76} * \exp\left(-\frac{17870}{T_{gas}}\right)$ $F_C = 0.35 \times 10^0$	22
$C_3H_8 \rightarrow CH_3 + C_2H_5$	$k_0 = (1.30 \times 10^{-5}) * \exp\left(-\frac{32700}{T_{gas}}\right)$ $k_\infty = (4.00 \times 10^{23}) * (T_{gas})^{-1.87} * \exp\left(-\frac{45394}{T_{gas}}\right)$ $F_C = (0.24) * \exp\left(-\frac{T_{gas}}{1946}\right) + 0.76 * \exp\left(-\frac{T_{gas}}{38}\right)$	22
$H + H \rightarrow H_2$	$k_0 = (2.70 \times 10^{-31}) * (T_{gas})^{-0.60}$ $k_\infty = (1.00 \times 10^{-11})$ $F_C = (0.0506) * (T_{gas})^{0.40}$	25
$CH_3 + C_2H_3 \rightarrow C_3H_6$	$k = (5.00 \times 10^{-27})$ $k_\infty = (1.10 \times 10^{-10})$ $F_C = (0.0506) * (T_{gas})^{0.40}$	26
$CH_2 + C_2H_4 \rightarrow C_3H_6$	$k_0 = (1.5 \times 10^{-18}) * (T_{gas})^{-3} * \exp\left(-\frac{300}{T_{gas}}\right)$ $k_\infty = (9.17 \times 10^{-12}) * \left(\frac{T_{gas}}{298.15}\right)^{0.00730} * \exp\left(-\frac{4410}{RT_{gas}}\right)$ $F_C = (0.0506) * (T_{gas})^{0.40}$	22

$H + C_3H_6 \rightarrow C_3H_7$	$k_0 = (1.30 \times 10^{-28}) * \exp\left(-\frac{380}{T_{gas}}\right)$ $k_\infty = (9.47 \times 10^{-15}) * (T_{gas})^{1.16} * \exp\left(-\frac{440}{T_{gas}}\right)$ $F_C = (0.0506) * (T_{gas})^{0.40}$	27
$C + H_2 \rightarrow CH_2$	$k_0 = (7.00 \times 10^{-32})$ $k_\infty = (2.06 \times 10^{-11}) * \exp\left(-\frac{57}{T_{gas}}\right)$ $F_C = (0.0506) * (T_{gas})^{0.40}$	28
$H + C_3H_5 \rightarrow C_3H_6$	$k_0 = (1.50 \times 10^{-29})$ $k_\infty = (2.4 \times 10^{-10})$ $F_C = (0.0506) * (T_{gas})^{0.40}$	27

137

138 **Table S4** Neutral-neutral molecular recombination reactions and respective rate coefficients (in $\text{cm}^3 \text{s}^{-1}$
139 1 or $\text{cm}^6 \text{s}^{-1}$). T_{gas} is given in Kelvin and R is the gas constant $8.314 \text{ J mol}^{-1} \text{ K}^{-1}$. References are shown
140 in the last column.

$CH_4 + CH_3 \rightarrow H + C_2H_6$	$4.95 \times 10^{-13} \left(\frac{T_{gas}}{298.15}\right) \exp\left(-\frac{188000}{RT_{gas}}\right)$	29
$CH_4 + CH_3 \rightarrow H_2 + C_2H_5$	$1.66 \times 10^{-11} \exp\left(\frac{-96450}{RT_{gas}}\right)$	29
$CH_4 + CH_2 \rightarrow CH_3 + CH_3$	$7.14 \times 10^{-12} \exp\left(\frac{-41990}{RT_{gas}}\right)$	30
$CH_4 + CH \rightarrow C_2H_4 + H$	$3.96 \times 10^{-8} \left(\frac{T_{gas}}{298.15}\right)^{-1.04} \exp\left(-\frac{36.1}{T_{gas}}\right)$	31
$CH_4 + C \rightarrow CH + CH_3$	$8.30 \times 10^{-11} \exp\left(-\frac{24.015}{1.987 \times T_{gas}}\right)$	32
$CH_4 + C \rightarrow C_2H_4$	5.00×10^{-15}	32
$CH_4 + C_2H_5 \rightarrow C_2H_6 + CH_3$	$2.51 \times 10^{-15} \left(\frac{T_{gas}}{298.15}\right)^{2.84} \exp\left(-\frac{52550}{RT_{gas}}\right)$	33
$CH_4 + C_2H_3 \rightarrow C_2H_4 + CH_3$	$2.13 \times 10^{-14} \left(\frac{T_{gas}}{298.15}\right)^{4.02} \exp\left(-\frac{22860}{RT_{gas}}\right)$	33
$CH_4 + C_2H \rightarrow C_2H_2 + CH_3$	$3.01 \times 10^{-12} \exp\left(-\frac{2080}{RT_{gas}}\right)$	33
$CH_4 + C_3H_7 \rightarrow C_3H_8 + CH_3$	$3.54 \times 10^{-16} \left(\frac{T_{gas}}{298.15}\right)^{4.02} \exp\left(-\frac{45480}{RT_{gas}}\right)$	33
$CH_4 + C_3H_5 \rightarrow C_3H_6 + CH_3$	$1.71 \times 10^{-14} \left(\frac{T_{gas}}{298.15}\right)^{3.40} \exp\left(-\frac{97280}{RT_{gas}}\right)$	34
$CH_4 + H \rightarrow CH_3 + H_2$	$2.94 \times 10^{-10} \exp\left(-\frac{57650}{RT_{gas}}\right)$	35
$CH_3 + CH_3 \rightarrow C_2H_5 + H$	$1.46 \times 10^{-11} \left(\frac{T_{gas}}{298.15}\right)^{0.10} \exp\left(-\frac{44400}{RT_{gas}}\right)$	36
$CH_3 + CH_3 \rightarrow CH_2 + CH_4$	$1.16 \times 10^{-13} \left(\frac{T_{gas}}{298.15}\right)^{1.34} \exp\left(-\frac{67910}{RT_{gas}}\right)$	37

$CH_3 + CH_3 \rightarrow C_2H_4 + H_2$	$1.66 \times 10^{-8} \exp\left(-\frac{138000}{RT_{gas}}\right)$	38
$CH_3 + CH_2 \rightarrow C_2H_4 + H$	5.01×10^{-11}	39
$CH_3 + C_2H_6 \rightarrow C_2H_5 + CH_4$	$1.74 \times 10^{-16} \left(\frac{T_{gas}}{298}\right)^{6.00} \exp\left(-\frac{25280}{RT_{gas}}\right)$	33
$CH_3 + C_2H_5 \rightarrow C_2H_4 + CH_4$	$1.88 \times 10^{-12} \left(\frac{T_{gas}}{298.0}\right)^{-0.5}$	33
$CH_3 + C_2H_5 \rightarrow C_2H_6 + CH_2$	$3.0 \times 10^{-44} (T_{gas})^{9.0956}$	33
$CH_3 + C_2H_4 \rightarrow C_2H_3 + CH_4$	$6.91 \times 10^{-12} \exp\left(-\frac{46560}{RT_{gas}}\right)$	33
$CH_3 + C_2H_4 \rightarrow C_3H_7$	$3.50 \times 10^{-13} \exp\left(-\frac{3700}{T_{gas}}\right)$	22
$CH_3 + C_2H_3 \rightarrow C_2H_2 + CH_4$	$1.5 \times 10^{-11} \exp\left(\frac{3200}{RT_{gas}}\right)$	26
$CH_3 + C_2H_3 \rightarrow C_3H_5 + H$	$2.59 \times 10^{-9} \left(\frac{T_{gas}}{298.0}\right)^{-1.25} \exp\left(-\frac{32100}{RT_{gas}}\right)$	26
$CH_3 + C_2H_2 \rightarrow CH_4 + C_2H$	$3.01 \times 10^{-13} \exp\left(-\frac{72340}{RT_{gas}}\right)$	33
$CH_3 + C_2H_2 \rightarrow C_3H_5$	$1.00 \times 10^{-12} \exp\left(-\frac{3900}{T_{gas}}\right)$	22
$CH_3 + C_3H_8 \rightarrow C_3H_7 + CH_4$	$1.50 \times 10^{-24} (T_{gas})^{3.65} \exp\left(-\frac{7154}{1.987 \times T_{gas}}\right)$	33
$CH_3 + C_3H_7 \rightarrow C_3H_6 + CH_4$	$3.07 \times 10^{-12} \left(\frac{T_{gas}}{298}\right)^{-0.32}$	33
$CH_3 + C_3H_7 \rightarrow C_2H_5 + C_2H_5$	$\left(\frac{1.93 \times 10^{13}}{6.0223 \times 10^{23}}\right) (T_{gas})^{-0.32}$	33
$CH_3 + C_3H_6 \rightarrow C_3H_5 + CH_4$	$1.68 \times 10^{-15} \left(\frac{T_{gas}}{298}\right)^{3.50} \exp\left(-\frac{23780}{RT_{gas}}\right)$	37
$CH_3 + H_2 \rightarrow CH_4 + H$	$2.52 \times 10^{-14} \left(\frac{T_{gas}}{298}\right)^{3.12} \exp\left(\frac{36420}{RT_{gas}}\right)$	35
$CH_3 + H \rightarrow CH_2 + H_2$	$1.00 \times 10^{-10} \exp\left(-\frac{63190}{RT_{gas}}\right)$	35
$CH_3 \rightarrow H_2 + CH$	$8.30 \times 10^{-9} \exp\left(-\frac{356000}{RT_{gas}}\right)$	22
$CH_3 \rightarrow CH_2 + H$	$1.69 \times 10^{-8} \exp\left(-\frac{379000}{RT_{gas}}\right)$	22
$CH_2 + CH_2 \rightarrow C_2H_2 + H + H$	$3.32 \times 10^{-10} \exp\left(-\frac{45980}{RT_{gas}}\right)$	30
$CH_2 + CH_2 \rightarrow C_2H_2 + H_2$	$2.62 \times 10^{-9} \exp\left(-\frac{49970}{RT_{gas}}\right)$	30
$CH_2 + CH_3 \rightarrow C_2H_5$	$7.00 \times 10^{-23} (T_{gas})^{3.6337}$	30
$CH_2 + C_2H_6 \rightarrow C_2H_5 + CH_3$	$9.0 \times 10^{-33} (T_{gas})^{6.4162}$	30
$CH_2 + C_2H_6 \rightarrow C_3H_8$	4.80×10^{-12}	30
$CH_2 + C_2H_5 \rightarrow C_2H_4 + CH_3$	8.01×10^{-11}	30
$CH_2 + C_2H_3 \rightarrow C_2H_2 + CH_3$	8.01×10^{-11}	30

$CH_2 + C_2H_4 \rightarrow C_3H_5 + H$	$4.25 \times 10^{-12} \exp\left(-\frac{2658}{T_{gas}}\right)$	30
$CH_2 + C_2H \rightarrow C_2H_2 + CH$	3.01×10^{-11}	30
$CH_2 + C_3H_8 \rightarrow C_3H_7 + CH_3$	$1.61 \times 10^{-15} \left(\frac{T_{gas}}{298}\right)^{3.65} \exp\left(-\frac{29930}{RT_{gas}}\right)$	30
$CH_2 + C_3H_7 \rightarrow C_2H_4 + C_2H_5$	3.01×10^{-11}	30
$CH_2 + C_3H_7 \rightarrow C_3H_6 + CH_3$	3.01×10^{-11}	30
$CH_2 + C_3H_6 \rightarrow C_3H_5 + CH_3$	$1.20 \times 10^{-12} \exp\left(-\frac{25940}{RT_{gas}}\right)$	30
$CH_2 + H_2 \rightarrow CH_3 + H$	$3.59 \times 10^{-13} \left(\frac{T_{gas}}{298}\right)^{2.30} \exp\left(-\frac{30760}{RT_{gas}}\right)$	30
$CH_2 + H \rightarrow CH + H_2$	$1.00 \times 10^{-11} \exp\left(\frac{7480}{RT_{gas}}\right)$	37
$CH_2 \rightarrow C + H_2$	$5.00 \times 10^{-10} \exp\left(-\frac{32600}{T_{gas}}\right)$	30
$CH_2 \rightarrow CH + H$	$1.56 \times 10^{-8} \exp\left(-\frac{44880}{T_{gas}}\right)$	30
$CH + H_2 \rightarrow CH_2 + H$	$1.48 \times 10^{-11} \left(\frac{T_{gas}}{298.0}\right)^{1.79} \exp\left(-\frac{6980}{RT_{gas}}\right)$	40
$CH + H \rightarrow C + H_2$	$6.50 \times 10^{-10} (T_{gas})^{0.01} \exp\left(-\frac{22330}{RT_{gas}}\right)$	38
$CH + CH_3 \rightarrow C_2H_3 + H$	$\left(\frac{3.0 \times 10^{13}}{6.0223 \times 10^{23}}\right)$	40
$CH + CH_2 \rightarrow C_2H_2 + H$	$\left(\frac{4.0 \times 10^{13}}{6.0223 \times 10^{23}}\right)$	40
$CH + CH \rightarrow C_2H_2$	1.99×10^{-10}	40
$CH + C_2H_2 \rightarrow C_2H + CH_2$	$3.80 \times 10^{-8} (T_{gas})^{-0.859} \exp\left(-\frac{33.5}{T_{gas}}\right)$	31
$CH + C_2H_3 \rightarrow CH_2 + C_2H_2$	8.3×10^{-11}	31
$CH + C_2H_4 \rightarrow C_3H_5$	$2.84 \times 10^{-10} \left(\frac{T_{gas}}{298.15}\right)^{-0.310}$	31
$CH + C_2H_4 \rightarrow C_2H_2 + CH_3$	$0.50 \times 1.59 \times 10^{-9} (T_{gas})^{-0.546} \exp\left(-\frac{29.6}{T_{gas}}\right)$	31
$CH + C_2H_4 \rightarrow CH_4 + C_2H$	$0.50 \times 1.59 \times 10^{-9} (T_{gas})^{-0.546} \exp\left(-\frac{29.6}{T_{gas}}\right)$	31
$CH + C_2H_5 \rightarrow C_3H_5 + H$	$3.80 \times 10^{-8} (T_{gas})^{-0.859} \exp\left(-\frac{33.5}{T_{gas}}\right)$	31
$CH + C_2H_6 \rightarrow C_2H_4 + CH_3$	$3.80 \times 10^{-8} (T_{gas})^{-0.859} \exp\left(-\frac{53.2}{T_{gas}}\right)$	41
$CH + C_2H_6 \rightarrow C_3H_6 + H$	$6.17 \times 10^{-11} (T_{gas})^{-0.52} \exp\left(-\frac{29.2}{T_{gas}}\right)$	41
$CH + C_2H_6 \rightarrow C_3H_7$	1.60×10^{-10}	41
$CH \rightarrow C + H$	$3.16 \times 10^{-10} \exp\left(-\frac{280000}{RT_{gas}}\right)$	40
$C_2H_6 + C_2H_3 \rightarrow C_2H_5 + C_2H_4$	$1.46 \times 10^{-13} \left(\frac{T_{gas}}{298}\right)^{3.30} \exp\left(-\frac{43900}{RT_{gas}}\right)$	42

$C_2H_6 + C_2H \rightarrow C_2H_2 + C_2H_5$	$3.50 \times 10^{-11} \exp\left(\frac{20}{RT_{gas}}\right)$	22
$C_2H_6 + C_3H_7 \rightarrow C_3H_8 + C_2H_5$	$1.19 \times 10^{-15} \left(\frac{T_{gas}}{298}\right)^{3.82} \exp\left(-\frac{37830}{RT_{gas}}\right)$	43
$C_2H_6 + C_3H_5 \rightarrow C_3H_6 + C_2H_5$	$5.71 \times 10^{-14} \left(\frac{T_{gas}}{298}\right)^{3.30} \exp\left(-\frac{83060}{RT_{gas}}\right)$	34
$C_2H_6 + H \rightarrow C_2H_5 + H_2$	$1.23 \times 10^{-11} \left(\frac{T_{gas}}{298}\right)^{1.50} \exp\left(-\frac{31010}{RT_{gas}}\right)$	37
$H + C_2H_6 \rightarrow CH_4 + CH_3$	$8.97 \times 10^{-20} \exp\left(-\frac{48640}{RT_{gas}}\right)$	38
$C_2H_6 \rightarrow C_2H_5 + H$	$8.11 \times 10^{17} \left(\frac{T_{gas}}{298}\right)^{-1.23} \exp\left(-\frac{427000}{RT_{gas}}\right)$	44
$C_2H_6 \rightarrow C_2H_4 + H_2$	$1.32 \times 10^{15} \exp\left(-\frac{306000}{RT_{gas}}\right)$	44
$C_2H_5 + C_2H_3 \rightarrow C_2H_6 + C_2H_2$	2.40×10^{-11}	45
$C_2H_5 + C_2H_3 \rightarrow C_2H_4 + C_2H_4$	9.60×10^{-11}	45
$C_2H_5 + C_2H_5 \rightarrow C_2H_6 + C_2H_4$	2.41×10^{-12}	22
$C_2H_5 + C_2H_4 \rightarrow C_2H_6 + C_2H_3$	$5.83 \times 10^{-14} \left(\frac{T_{gas}}{298}\right)^{3.13} \exp\left(-\frac{75330}{RT_{gas}}\right)$	22
$C_2H_5 + C_2H_2 \rightarrow C_2H_6 + C_2H$	$4.50 \times 10^{-13} \exp\left(-\frac{98110}{RT_{gas}}\right)$	42
$C_2H_5 + C_2H \rightarrow C_2H_4 + C_2H_2$	3.01×10^{-12}	42
$C_2H_5 + C_3H_8 \rightarrow C_2H_6 + C_3H_7$	$1.61 \times 10^{-15} \left(\frac{T_{gas}}{298}\right)^{3.65} \exp\left(-\frac{38250}{RT_{gas}}\right)$	43
$C_2H_5 + C_3H_7 \rightarrow C_3H_8 + C_2H_4$	1.91×10^{-12}	43
$C_2H_5 + C_3H_7 \rightarrow C_3H_6 + C_2H_6$	2.41×10^{-12}	43
$C_2H_5 + C_3H_6 \rightarrow C_3H_5 + C_2H_6$	$1.69 \times 10^{-15} \left(\frac{T_{gas}}{298}\right)^{3.50} \exp\left(-\frac{27770}{RT_{gas}}\right)$	46
$C_2H_5 + C_3H_5 \rightarrow C_3H_6 + C_2H_4$	$4.30 \times 10^{-12} \exp\left(\frac{550}{RT_{gas}}\right)$	34
$C_2H_5 + H_2 \rightarrow C_2H_6 + H$	$5.10 \times 10^{-24} \left(\frac{T_{gas}}{298}\right)^{3.60} \exp\left(-\frac{35340}{RT_{gas}}\right)$	22
$H + C_2H_5 \rightarrow CH_3 + CH_3$	$1.79 \times 10^{-10} \exp\left(-\frac{3640}{RT_{gas}}\right)$	22
$H + C_2H_5 \rightarrow C_2H_4 + H_2$	3.32×10^{-12}	42
$C_2H_5 \rightarrow CH_2 + CH_3$	$1.0 \times 10^{-118} (T_{gas})^{37.47}$	44
$C_2H_4 + C_2H \rightarrow C_2H_2 + C_2H_3$	1.40×10^{-10}	42
$C_2H_4 + C_2H_2 \rightarrow C_2H_3 + C_2H_3$	$4.0 \times 10^{-11} \exp\left(-\frac{286000}{RT_{gas}}\right)$	42
$C_2H_4 + C_3H_6 \rightarrow C_3H_5 + C_2H_5$	$9.6 \times 10^{-11} \exp\left(-\frac{216000}{RT_{gas}}\right)$	46
$C_2H_4 + C_3H_6 \rightarrow C_2H_3 + C_3H_7$	$1.0 \times 10^{-10} \exp\left(-\frac{316000}{RT_{gas}}\right)$	46
$C_2H_4 + C_2H_4 \rightarrow C_2H_5 + C_2H_3$	$8.0 \times 10^{-10} \exp\left(-\frac{299000}{RT_{gas}}\right)$	42

$C_2H_4 + H \rightarrow C_2H_3 + H_2$	$8.41 \times 10^{-17} (T_{gas})^{1.93} \exp\left(-\frac{6518}{T_{gas}}\right)$	37
$C_2H_4 + H_2 \rightarrow C_2H_5 + H$	$1.69 \times 10^{-11} \exp\left(-\frac{285000}{RT_{gas}}\right)$	42
$C_2H_4 + H_2 \rightarrow C_2H_6$	$4.75 \times 10^{-16} \exp\left(-\frac{180000}{RT_{gas}}\right)$	42
$C_2H_4 + C \rightarrow C_2H_2 + CH_2$	1.24×10^{-11}	47
$C_2H_4 \rightarrow C_2H_3 + H$	$2.00 \times 10^{16} \exp\left(-\frac{461000}{RT_{gas}}\right)$	44
$C_2H_3 + C_2H_3 \rightarrow C_2H_4 + C_2H_2$	3.50×10^{-11}	42
$C_2H_3 + C_2H \rightarrow C_2H_2 + C_2H_2$	3.15×10^{-11}	42
$C_2H_3 + C_3H_8 \rightarrow C_2H_4 + C_3H_7$	$1.46 \times 10^{-13} \left(\frac{T_{gas}}{298}\right)^{3.30} \exp\left(-\frac{43900}{RT_{gas}}\right)$	43
$C_2H_3 + C_3H_7 \rightarrow C_3H_8 + C_2H_2$	2.01×10^{-12}	43
$C_2H_3 + C_3H_7 \rightarrow C_3H_6 + C_2H_4$	2.01×10^{-12}	43
$C_2H_3 + C_3H_6 \rightarrow C_3H_5 + C_2H_4$	$1.68 \times 10^{-15} \left(\frac{T_{gas}}{298}\right)^{3.50} \exp\left(-\frac{19620}{RT_{gas}}\right)$	46
$C_2H_3 + C_3H_5 \rightarrow C_3H_6 + C_2H_2$	8.00×10^{-12}	34
$C_2H_3 + H_2 \rightarrow C_2H_4 + H$	$1.61 \times 10^{-13} \left(\frac{T_{gas}}{298}\right)^{2.63} \exp\left(-\frac{35750}{RT_{gas}}\right)$	48
$C_2H_3 + H \rightarrow C_2H_2 + H_2$	$1.50 \times 10^{-12} (T_{gas})^{0.50}$	22
$C_2H_2 + C_3H_7 \rightarrow C_3H_5 + C_2H_4$	$1.20 \times 10^{-12} \exp\left(-\frac{37700}{RT_{gas}}\right)$	43
$C_2H_2 + C_3H_6 \rightarrow C_2H_3 + C_3H_5$	$6.71 \times 10^{-11} \exp\left(-\frac{196000}{RT_{gas}}\right)$	46
$C_2H_2 + C_2H_2 \rightarrow C_2H + C_2H_3$	$1.6 \times 10^{-11} \exp\left(-\frac{353000}{RT_{gas}}\right)$	42
$C_2H_2 + H_2 \rightarrow C_2H_4$	$5.0 \times 10^{-13} \exp\left(-\frac{163000}{RT_{gas}}\right)$	42
$C_2H_2 + H_2 \rightarrow C_2H_3 + H$	$1.33 \times 10^{-12} \exp\left(-\frac{236000}{RT_{gas}}\right)$	42
$C_2H_2 + H \rightarrow C_2H + H_2$	$2.77 \times 10^{-10} \left(\frac{T_{gas}}{298.0}\right)^{1.32} \exp\left(-\frac{128000}{RT_{gas}}\right)$	38
$C_2H_2 \rightarrow C_2H + H$	$2.63 \times 10^{15} \exp\left(-\frac{519000}{RT_{gas}}\right)$	44
$C_2H + C_3H_8 \rightarrow C_2H_2 + C_3H_7$	1.79×10^{-11}	43
$C_2H + C_3H_7 \rightarrow C_3H_6 + C_2H_2$	2.01×10^{-11}	43
$C_2H + C_3H_6 \rightarrow C_3H_5 + C_2H_2$	1.79×10^{-11}	46
$C_2H + C_2H \rightarrow C_2H_2 + C_2$	3.01×10^{-12}	42
$C_2H + H_2 \rightarrow C_2H_2 + H$	$1.59 \times 10^{-11} \left(\frac{T_{gas}}{298}\right)^{0.90} \exp\left(-\frac{8310}{RT_{gas}}\right)$	42
$H + C_2H \rightarrow H_2 + C_2$	$5.99 \times 10^{-11} \exp\left(-\frac{118000}{RT_{gas}}\right)$	37
$C_3H_8 + C_3H_5 \rightarrow C_3H_6 + C_3H_7$	$5.71 \times 10^{-14} \left(\frac{T_{gas}}{298}\right)^{3.30} \exp\left(-\frac{83060}{RT_{gas}}\right)$	34

$C_3H_8 + H \rightarrow C_3H_7 + H_2$	$4.23 \times 10^{-12} \left(\frac{T_{gas}}{298}\right)^{2.54} \exp\left(-\frac{28270}{RT_{gas}}\right)$	38
$C_3H_8 \rightarrow C_3H_7 + H$	$1.58 \times 10^{16} \exp\left(-\frac{408000}{RT_{gas}}\right)$	44
$C_3H_7 + C_3H_7 \rightarrow C_3H_6 + C_3H_8$	2.81×10^{-12}	27
$C_3H_7 + C_3H_6 \rightarrow C_3H_5 + C_3H_8$	$1.69 \times 10^{-15} \left(\frac{T_{gas}}{298}\right)^{3.50} \exp\left(-\frac{27770}{RT_{gas}}\right)$	27
$C_3H_7 + C_3H_5 \rightarrow C_3H_6 + C_3H_6$	$2.41 \times 10^{-12} \exp\left(\frac{550}{RT_{gas}}\right)$	27
$C_3H_7 + H_2 \rightarrow C_3H_8 + H$	$3.19 \times 10^{-14} \left(\frac{T_{gas}}{298}\right)^{2.84} \exp\left(-\frac{38250}{RT_{gas}}\right)$	27
$C_3H_7 + H \rightarrow C_3H_6 + H_2$	3.01×10^{-12}	27
$C_3H_7 + H \rightarrow CH_3 + C_2H_5$	$6.74 \times 10^{-18} (T_{gas})^{2.19} \exp\left(-\frac{890}{1.987 T_{gas}}\right)$	27
$C_3H_7 \rightarrow C_2H_4 + CH_3$	$1.31 \times 10^{13} \left(\frac{T_{gas}}{298}\right)^{0.87} \exp\left(-\frac{127000}{RT_{gas}}\right)$	27
$C_3H_6 + C_3H_6 \rightarrow C_3H_7 + C_3H_5$	$4.2 \times 10^{-10} \exp\left(-\frac{231000}{RT_{gas}}\right)$	37
$C_3H_6 + H \rightarrow C_3H_5 + H_2$	$4.40 \times 10^{-13} \left(\frac{T_{gas}}{298}\right)^{2.50} \exp\left(-\frac{10390}{RT_{gas}}\right)$	38
$C_3H_6 + H \rightarrow C_2H_4 + CH_3$	$7.51 \times 10^{-11} \exp\left(-\frac{17300}{RT_{gas}}\right)$	38
$C_3H_6 \rightarrow C_3H_5 + H$	$2.50 \times 10^{15} \exp\left(\frac{-410000}{RT_{gas}}\right)$	37
$C_3H_6 \rightarrow CH_3 + C_2H_3$	$1.18 \times 10^{18} \left(\frac{T_{gas}}{298}\right)^{-1.20} \exp\left(-\frac{409000}{RT_{gas}}\right)$	37
$C_3H_6 \rightarrow CH_4 + C_2H_2$	$3.50 \times 10^{12} \exp\left(\frac{-293000}{RT_{gas}}\right)$	44
$C_3H_6 \rightarrow CH_2 + C_2H_4$	$5.03 \times 10^{15} \exp\left(\frac{-808000}{RT_{gas}}\right)$	44
$C_3H_5 + H_2 \rightarrow C_3H_6 + H$	$1.39 \times 10^{-13} \left(\frac{T_{gas}}{298}\right)^{2.38} \exp\left(-\frac{79490}{RT_{gas}}\right)$	34
$C_3H_5 + H \rightarrow C_2H_3 + CH_3$	4.00×10^{-12}	34
$C_3H_5 \rightarrow C_2H_2 + CH_3$	$1.26 \times 10^{13} \exp\left(-\frac{140000}{RT_{gas}}\right)$	44
$C + C \rightarrow C_2$	2.20×10^{-12}	49
$C_2 \rightarrow C + C_s$	$1.5 \times 10^{16} \exp\left(-\frac{594630}{RT_{gas}}\right)$	50
$C_3 \rightarrow C_2 + C_s$	$3.48 \times 10^{11} (T_{gas})^{1.1256} \exp\left(-\frac{131430}{RT_{gas}}\right)$	50
$C_2 + C_2 \rightarrow C + C_3$	5.31×10^{-10}	50
$C + H_2 \rightarrow CH + H$	$6.64 \times 10^{-10} \exp\left(-\frac{97280}{RT_{gas}}\right)$	32
$C + CH_2 \rightarrow CH + CH$	$2.69 \times 10^{-12} \exp\left(-\frac{196000}{RT_{gas}}\right)$	51

$C + CH_2 \rightarrow H + C_2H$	8.30×10^{-11}	52
$C + CH_3 \rightarrow H + C_2H_2$	8.30×10^{-11}	52
$C_2 + H_2 \rightarrow C_2H_2$	$1.77 \times 10^{-10} \exp\left(-\frac{1470}{T_{gas}}\right)$	38
$C_2 + H_2 \rightarrow C_2H + H$	$1.10 \times 10^{-10} \exp\left(-\frac{33260}{RT_{gas}}\right)$	38
$C_2 + CH_4 \rightarrow C_2H + CH_3$	$5.05 \times 10^{-11} \exp\left(-\frac{297}{T_{gas}}\right)$	38
$H_2 + M \rightarrow H + H + M$	$3.64 \times 10^{-8} \left(\frac{T_{gas}}{298.15}\right)^{-1.00} \exp\left(-\frac{431000}{RT_{gas}}\right)$	25
$H + H \rightarrow e^- + H + H^+$	See reference	53

141

142 **Table S5** Negative and positive ion-ion and ion-neutral molecular recombination reactions and
143 respective rate coefficients (in $\text{cm}^3 \text{s}^{-1}$ or $\text{cm}^6 \text{s}^{-1}$). T_{gas} is given in Kelvin. References are shown in the
144 last column.

$CH_5^+ + CH_2 \rightarrow CH_3^+ + CH_4$	0.960×10^{-9}	54
$CH_5^+ + CH \rightarrow CH_2^+ + CH_4$	0.690×10^{-9}	54
$CH_5^+ + C \rightarrow CH^+ + CH_4$	0.120×10^{-8}	54
$CH_5^+ + C_2H_6 \rightarrow C_2H_5^+ + H_2 + CH_4$	0.225×10^{-9}	54
$CH_5^+ + C_2H_4 \rightarrow C_2H_5^+ + CH_4$	0.150×10^{-8}	54
$CH_5^+ + C_2H_2 \rightarrow C_2H_3^+ + CH_4$	0.160×10^{-8}	54
$CH_5^+ + C_2H \rightarrow C_2H_2^+ + CH_4$	0.900×10^{-9}	54
$CH_5^+ + C_2 \rightarrow C_2H^+ + CH_4$	0.950×10^{-9}	54
$CH_5^+ + H \rightarrow CH_4^+ + H_2$	0.150×10^{-9}	55
$CH_4^+ + CH_4 \rightarrow CH_5^+ + CH_3$	0.15×10^{-8}	56
$CH_4^+ + C_2H_6 \rightarrow C_2H_4^+ + CH_4 + H_2$	0.19×10^{-8}	56
$CH_4^+ + C_2H_4 \rightarrow C_2H_5^+ + CH_3$	1.38×10^{-9}	56
$CH_4^+ + C_2H_4 \rightarrow C_2H_4^+ + CH_4$	0.42×10^{-9}	56
$CH_4^+ + C_2H_2 \rightarrow C_2H_3^+ + CH_3$	6.27×10^{-10}	56
$CH_4^+ + C_2H_2 \rightarrow C_2H_2^+ + CH_4$	0.55×10^{-9}	56
$CH_4^+ + H_2 \rightarrow CH_5^+ + H$	$4.89 \times 10^{-11} \left(\frac{300}{T_{gas}}\right)^{0.14} \exp\left(-\frac{36.10}{T_{gas}}\right)$	57
$CH_4^+ + H \rightarrow CH_3^+ + H_2$	0.10×10^{-10}	55
$CH_3^+ + CH_4 \rightarrow CH_4^+ + CH_3$	0.136×10^{-9}	56
$CH_3^+ + CH_4 \rightarrow C_2H_5^+ + H_2$	0.120×10^{-8}	56
$CH_3^+ + CH_2 \rightarrow C_2H_3^+ + H_2$	0.990×10^{-9}	56
$CH_3^+ + CH \rightarrow C_2H_2^+ + H_2$	0.710×10^{-9}	56
$CH_3^+ + C \rightarrow C_2H^+ + H_2$	1.200×10^{-9}	56
$CH_3^+ + C_2H_6 \rightarrow C_2H_5^+ + CH_4$	1.48×10^{-9}	56
$CH_3^+ + C_2H_4 \rightarrow C_2H_3^+ + CH_4$	0.35×10^{-9}	56
$CH_3^+ + C_2H_3 \rightarrow C_2H_3^+ + CH_3$	0.300×10^{-9}	56

$CH_3^+ + H_2 \rightarrow CH_4^+ + H$	1.58×10^{-9}	57
$CH_2^+ + CH_4 \rightarrow CH_3^+ + CH_3$	0.138×10^{-9}	54
$CH_2^+ + CH_4 \rightarrow C_2H_5^+ + H$	0.360×10^{-9}	54
$CH_2^+ + CH_4 \rightarrow C_2H_4^+ + H_2$	0.84×10^{-9}	54
$CH_2^+ + CH_4 \rightarrow C_2H_3^+ + H_2 + H$	0.231×10^{-9}	54
$CH_2^+ + CH_4 \rightarrow C_2H_2^+ + 2H_2$	0.397×10^{-9}	54
$CH_2^+ + H_2 \rightarrow CH_3^+ + H$	0.16×10^{-8}	57
$CH_2^+ + C \rightarrow C_2H^+ + H$	0.12×10^{-8}	54
$CH^+ + CH_2 \rightarrow C_2H^+ + H_2$	0.10×10^{-8}	54
$CH^+ + CH \rightarrow C_2^+ + H_2$	0.740×10^{-9}	54
$CH^+ + C \rightarrow C_2^+ + H$	1.2×10^{-9}	54
$CH^+ + H \rightarrow C^+ + H_2$	7.50×10^{-10}	55
$CH^+ + CH_4 \rightarrow C_2H_4^+ + H$	0.65×10^{-10}	54
$CH^+ + CH_4 \rightarrow C_2H_3^+ + H_2$	0.109×10^{-8}	54
$CH^+ + CH_4 \rightarrow C_2H_2^+ + H_2 + H$	0.143×10^{-9}	54
$CH^+ + H_2 \rightarrow CH_2^+ + H$	1.58×10^{-9}	57
$C_2H_6^+ + C_2H_4 \rightarrow C_2H_4^+ + C_2H_6$	1.15×10^{-9}	56
$C_2H_6^+ + C_2H_2 \rightarrow C_2H_5^+ + C_2H_3$	2.47×10^{-10}	56
$C_2H_6^+ + H \rightarrow C_2H_5^+ + H_2$	1.00×10^{-10}	58
$C_2H_5^+ + H \rightarrow C_2H_4^+ + H_2$	1.00×10^{-10}	55
$C_2H_4^+ + C_2H_3 \rightarrow C_2H_5^+ + C_2H_2$	5.00×10^{-10}	56
$C_2H_4^+ + C_2H_3 \rightarrow C_2H_3^+ + C_2H_4$	5.00×10^{-10}	56
$C_2H_4^+ + H \rightarrow C_2H_3^+ + H_2$	3.00×10^{-10}	55
$C_2H_3^+ + C_2H_6 \rightarrow C_2H_5^+ + C_2H_4$	2.91×10^{-10}	56
$C_2H_3^+ + C_2H_4 \rightarrow C_2H_5^+ + C_2H_2$	8.90×10^{-10}	56
$C_2H_3^+ + C_2H_3 \rightarrow C_2H_5^+ + C_2H$	5.00×10^{-10}	59
$C_2H_3^+ + C_2H \rightarrow C_2H_2^+ + C_2H_2$	3.30×10^{-10}	59
$C_2H_3^+ + H \rightarrow C_2H_2^+ + H_2$	6.80×10^{-11}	55
$C_2H_2^+ + CH_4 \rightarrow C_2H_3^+ + CH_3$	4.10×10^{-9}	56
$C_2H_2^+ + C_2H_6 \rightarrow C_2H_5^+ + C_2H_3$	1.31×10^{-10}	56
$C_2H_2^+ + C_2H_6 \rightarrow C_2H_4^+ + C_2H_4$	2.48×10^{-10}	56
$C_2H_2^+ + C_2H_4 \rightarrow C_2H_4^+ + C_2H_2$	4.14×10^{-10}	56
$C_2H_2^+ + C_2H_3 \rightarrow C_2H_3^+ + C_2H_2$	3.30×10^{-10}	56
$C_2H_2^+ + H_2 \rightarrow C_2H_3^+ + H$	1.00×10^{-11}	57
$C_2H^+ + CH_2 \rightarrow CH_3^+ + C_2$	4.40×10^{-10}	59
$C_2H^+ + CH \rightarrow CH_2^+ + C_2$	3.20×10^{-10}	59
$C_2H^+ + CH_4 \rightarrow C_2H_2^+ + CH_3$	3.74×10^{-10}	59
$C_2H^+ + H_2 \rightarrow C_2H_2^+ + H$	1.10×10^{-9}	57
$H_3^+ + CH_4 \rightarrow CH_5^+ + H_2$	2.40×10^{-9}	60

$H_3^+ + CH_3 \rightarrow CH_4^+ + H_2$	2.10×10^{-9}	61
$H_3^+ + CH_2 \rightarrow CH_3^+ + H_2$	1.70×10^{-9}	60
$H_3^+ + CH \rightarrow CH_2^+ + H_2$	1.20×10^{-9}	60
$H_3^+ + C \rightarrow CH^+ + H_2$	2.00×10^{-9}	60
$H_3^+ + C_2H \rightarrow C_2H_2^+ + H_2$	1.70×10^{-9}	61
$H_3^+ + C_2 \rightarrow C_2H^+ + H_2$	1.80×10^{-9}	60
$H_3^+ + C_2H_6 \rightarrow C_2H_5^+ + H_2 + H_2$	2.40×10^{-9}	60
$H_3^+ + C_2H_5 \rightarrow C_2H_6^+ + H_2$	1.40×10^{-9}	61
$H_3^+ + C_2H_4 \rightarrow C_2H_5^+ + H_2$	1.15×10^{-9}	60
$H_3^+ + C_2H_4 \rightarrow C_2H_3^+ + H_2 + H_2$	1.15×10^{-9}	60
$H_3^+ + C_2H_3 \rightarrow C_2H_4^+ + H_2$	2.00×10^{-9}	61
$H_3^+ + C_2H_2 \rightarrow C_2H_3^+ + H_2$	3.50×10^{-9}	60
$H_3^+ + C_3H_6 \rightarrow C_2H_3^+ + CH_4 + H_2$	9.00×10^{-10}	61
$H_2^+ + CH_4 \rightarrow CH_5^+ + H$	1.14×10^{-10}	60
$H_2^+ + CH_4 \rightarrow CH_4^+ + H_2$	1.40×10^{-9}	60
$H_2^+ + CH_4 \rightarrow CH_3^+ + H_2 + H$	2.30×10^{-9}	60
$H_2^+ + CH_2 \rightarrow CH_3^+ + H$	1.00×10^{-9}	60
$H_2^+ + CH_2 \rightarrow CH_2^+ + H_2$	1.00×10^{-9}	60
$H_2^+ + CH \rightarrow CH_2^+ + H$	7.10×10^{-10}	60
$H_2^+ + CH \rightarrow CH^+ + H_2$	7.10×10^{-10}	60
$H_2^+ + C \rightarrow CH^+ + H$	2.40×10^{-9}	60
$H_2^+ + C_2H \rightarrow C_2H_2^+ + H$	1.00×10^{-9}	60
$H_2^+ + C_2H \rightarrow C_2H^+ + H_2$	1.00×10^{-9}	60
$H_2^+ + C_2 \rightarrow C_2H^+ + H$	1.10×10^{-9}	60
$H_2^+ + C_2 \rightarrow C_2^+ + H_2$	1.10×10^{-9}	60
$H_2^+ + C_2H_6 \rightarrow C_2H_6^+ + H_2$	2.94×10^{-9}	60
$H_2^+ + C_2H_6 \rightarrow C_2H_5^+ + H_2 + H$	1.37×10^{-9}	60
$H_2^+ + C_2H_6 \rightarrow C_2H_4^+ + H_2 + H_2$	2.35×10^{-9}	60
$H_2^+ + C_2H_6 \rightarrow C_2H_3^+ + 2 H_2 + H$	6.86×10^{-9}	60
$H_2^+ + C_2H_6 \rightarrow C_2H_2^+ + 3 H_2$	1.96×10^{-9}	60
$H_2^+ + C_2H_4 \rightarrow C_2H_4^+ + H_2$	2.21×10^{-9}	60
$H_2^+ + C_2H_4 \rightarrow C_2H_3^+ + H_2 + H$	1.81×10^{-9}	60
$H_2^+ + C_2H_4 \rightarrow C_2H_2^+ + H_2 + H_2$	8.82×10^{-10}	60
$H_2^+ + C_2H_2 \rightarrow C_2H_3^+ + H$	4.80×10^{-10}	60
$H_2^+ + C_2H_2 \rightarrow C_2H_2^+ + H_2$	4.82×10^{-9}	60
$H^+ + CH_4 \rightarrow CH_4^+ + H$	1.50×10^{-9}	62
$H^+ + CH_4 \rightarrow CH_3^+ + H_2$	2.30×10^{-9}	62
$H^+ + CH_3 \rightarrow CH_3^+ + H$	3.40×10^{-9}	60
$H^+ + CH_2 \rightarrow CH_2^+ + H$	1.40×10^{-9}	60

$H^+ + CH_2 \rightarrow CH^+ + H_2$	1.40×10^{-9}	60
$H^+ + CH \rightarrow CH^+ + H$	1.90×10^{-9}	60
$H^+ + C_2H_6 \rightarrow C_2H_5^+ + H_2$	1.30×10^{-9}	62
$H^+ + C_2H_6 \rightarrow C_2H_4^+ + H_2 + H$	1.40×10^{-9}	62
$H^+ + C_2H_6 \rightarrow C_2H_3^+ + H_2 + H_2$	2.80×10^{-9}	62
$H^+ + C_2H_5 \rightarrow C_2H_4^+ + H_2$	1.65×10^{-9}	60
$H^+ + C_2H_5 \rightarrow C_2H_3^+ + H_2 + H$	3.06×10^{-9}	60
$H^+ + C_2H_4 \rightarrow C_2H_4^+ + H$	1.00×10^{-9}	62
$H^+ + C_2H_4 \rightarrow C_2H_3^+ + H_2$	3.00×10^{-9}	62
$H^+ + C_2H_4 \rightarrow C_2H_2^+ + H_2 + H$	1.00×10^{-9}	62
$H^+ + C_2H_3 \rightarrow C_2H_3^+ + H$	2.00×10^{-9}	59
$H^+ + C_2H_3 \rightarrow C_2H_2^+ + H_2$	2.00×10^{-9}	59
$H^+ + C_2H_2 \rightarrow C_2H_2^+ + H$	5.40×10^{-10}	62
$H^+ + C_2H \rightarrow C_2H^+ + H$	1.50×10^{-9}	60
$H^+ + C_2H \rightarrow C_2^+ + H_2$	1.50×10^{-9}	60
$H^+ + C_2 \rightarrow C_2^+ + H$	3.10×10^{-9}	60
$C^+ + H^- \rightarrow C + H$	$7.51 \times 10^{-8} \left(\frac{T_{gas}}{300}\right)^{-0.50}$	63
$C^+ + CH_4 \rightarrow C_2H_3^+ + H$	1.43×10^{-9}	64
$C^+ + CH_4 \rightarrow C_2H_2^+ + H_2$	3.30×10^{-10}	64
$C^+ + CH_3 \rightarrow C_2H_2^+ + H$	1.30×10^{-9}	64
$C^+ + CH_3 \rightarrow C_2H^+ + H_2$	1.00×10^{-9}	64
$C^+ + CH_2 \rightarrow CH_2^+ + C$	5.20×10^{-10}	64
$C^+ + CH_2 \rightarrow C_2H^+ + H$	5.20×10^{-10}	64
$C^+ + CH \rightarrow CH^+ + C$	3.80×10^{-10}	64
$C^+ + CH \rightarrow C_2^+ + H$	3.80×10^{-10}	64
$C^+ + C_2H_6 \rightarrow C_2H_5^+ + CH$	2.31×10^{-10}	64
$C^+ + C_2H_6 \rightarrow C_2H_4^+ + CH_2$	1.16×10^{-10}	64
$C^+ + C_2H_6 \rightarrow C_2H_3^+ + CH_3$	4.95×10^{-10}	64
$C^+ + C_2H_6 \rightarrow C_2H_2^+ + CH_4$	8.25×10^{-11}	64
$C^+ + C_2H_5 \rightarrow C_2H_5^+ + C$	5.00×10^{-10}	64
$C^+ + C_2H_4 \rightarrow C_2H_4^+ + C$	1.70×10^{-11}	64
$C^+ + C_2H_4 \rightarrow C_2H_3^+ + CH$	8.50×10^{-11}	64
$C^+ + C_3H_6 \rightarrow C_2H_2^+ + C_2H_4$	6.00×10^{-10}	64
$C^+ + C_3H_6 \rightarrow C_2H_3^+ + C_2H_3$	6.00×10^{-10}	64
$C_2^+ + C \rightarrow C_2 + C^+$	1.10×10^{-10}	60
$C_2^+ + CH_4 \rightarrow C_2H_2^+ + CH_2$	1.82×10^{-10}	65
$C_2^+ + CH_4 \rightarrow C_2H^+ + CH_3$	2.38×10^{-10}	65
$C_2^+ + H_2 \rightarrow C_2H^+ + H$	1.40×10^{-9}	57
$C_2^+ + CH_2 \rightarrow CH_2^+ + C_2$	4.50×10^{-10}	65

$C_2^+ + CH \rightarrow CH^+ + C_2$	3.20×10^{-10}	65
$H^+ + 2H_2 \rightarrow H_2 + H_3^+$	$3.10 \times 10^{-29} \left(\frac{300}{T_{gas}}\right)^{0.5}$	17
$H^+ + H + M \rightarrow H_2^+ + M$	1.00×10^{-34}	17
$H_2^+ + H_2 \rightarrow H_2 + H^+ + H$	$1.00 \times 10^{-8} \exp\left(-\frac{84100.0}{T_{gas}}\right)$	57
$H_2^+ + H_2 \rightarrow H + H_3^+$	2.11×10^{-9}	57
$H_2^+ + H \rightarrow H_3^+$	2.10×10^{-9}	66
$H_2^+ + H \rightarrow H_2 + H^+$	6.39×10^{-10}	66
$H^- + M \rightarrow H + e^- + M$	$2.70 \times 10^{-10} \left(\frac{T_{gas}}{300}\right)^{-0.50} \exp\left(-\frac{5590.0}{T_{gas}}\right)$	63
$H^- + H_2^+ \rightarrow H + H + H$	$2.0 \times 10^{-7} \left(\frac{300}{T_{gas}}\right)^{0.50}$	67
$H^- + H_3^+ \rightarrow H_2 + H + H$	$2.0 \times 10^{-7} \left(\frac{300}{T_{gas}}\right)^{0.50}$	67
$H^- + H_3^+ \rightarrow H_2 + H_2$	$2.0 \times 10^{-7} \left(\frac{300}{T_{gas}}\right)^{0.50}$	67
$H^+ + H^- \rightarrow H + H$	$2.00 \times 10^{-7} \left(\frac{T_{gas}}{300}\right)^{-0.50}$	67
$H_2^+ + H^- \rightarrow H_2 + H$	$7.51 \times 10^{-8} \left(\frac{T_{gas}}{300}\right)^{-0.50}$	68
$H + H^- \rightarrow e^- + H_2$	$\frac{1.43 \times 10^{15} \left(\frac{T_{gas}}{300}\right)^{-0.146} \exp\left(-\frac{815}{T_{gas}}\right)}{(6.022 \times 10^{23})}$	69
$H^- + CH_3 \rightarrow CH_4 + e^-$	1.00×10^{-9}	60
$H^- + CH_2 \rightarrow CH_3 + e^-$	1.00×10^{-9}	60
$H^- + CH \rightarrow CH_2 + e^-$	1.00×10^{-10}	60
$H^- + C \rightarrow CH + e^-$	1.00×10^{-9}	60
$H^- + C_2H \rightarrow C_2H_2 + e^-$	1.00×10^{-9}	60
$H^- + C_2 \rightarrow C_2H + e^-$	1.00×10^{-9}	60
$H^- + CH_4^+ \rightarrow H + CH_4$	$7.51 \times 10^{-8} \left(\frac{T_{gas}}{300}\right)^{-0.50}$	67
$H^- + CH_3^+ \rightarrow H + CH_3$	$7.51 \times 10^{-8} \left(\frac{T_{gas}}{300}\right)^{-0.50}$	67
$H^- + C_2H_2^+ \rightarrow H + C_2H_2$	$7.51 \times 10^{-8} \left(\frac{T_{gas}}{300}\right)^{-0.50}$	70
$H^- + C_2H_3^+ \rightarrow H + C_2H_3$	$7.51 \times 10^{-8} \left(\frac{T_{gas}}{300}\right)^{-0.50}$	70
$H^- + C_2H^+ \rightarrow H + C_2H$	$7.51 \times 10^{-8} \left(\frac{T_{gas}}{300}\right)^{-0.50}$	70

$H^- + C_2H_4^+ \rightarrow H + C_2H_4$	$6.23 \times 10^{-8} \left(\frac{T_{gas}}{300}\right)^{-0.50}$	70
$H^- + C_2H_5^+ \rightarrow H + C_2H_5$	$5.16 \times 10^{-8} \left(\frac{T_{gas}}{300}\right)^{-0.50}$	70
$H^- + C_2H_6^+ \rightarrow H + C_2H_6$	$6.04 \times 10^{-8} \left(\frac{T_{gas}}{300}\right)^{-0.50}$	70
$CH_2^- + M \rightarrow CH_2 + e^- + M$	$2.70 \times 10^{-10} \left(\frac{T_{gas}}{300}\right)^{-0.50} \exp\left(-\frac{5590.0}{T_{gas}}\right)$	71
$CH_2 + H^- \rightarrow CH^- + H_2$	$8.87 \times 10^{-11} \left(\frac{T_{gas}}{300}\right)^{2.65} \exp\left(-\frac{416.51}{T_{gas}}\right)$	72
$CH^- + C \rightarrow C_2H + e^-$	1.00×10^{-9}	65
$CH^- + H \rightarrow CH_2 + e^-$	1.00×10^{-10}	65
$CH^- + H^+ \rightarrow CH + H$	$7.51 \times 10^{-8} \left(\frac{T_{gas}}{300}\right)^{-0.50}$	70
$CH^- + H_3^+ \rightarrow CH + H_2 + H$	$7.51 \times 10^{-8} \left(\frac{T_{gas}}{300}\right)^{-0.50}$	70
$CH^- + C^+ \rightarrow C + CH$	$7.51 \times 10^{-8} \left(\frac{T_{gas}}{300}\right)^{-0.50}$	70
$CH^- + CH_3^+ \rightarrow CH + CH_3$	$7.51 \times 10^{-8} \left(\frac{T_{gas}}{300}\right)^{-0.50}$	70
$CH^- + C_2H_2^+ \rightarrow CH + C_2H_2$	$7.51 \times 10^{-8} \left(\frac{T_{gas}}{300}\right)^{-0.50}$	70
$CH^- + C_2H_3^+ \rightarrow CH + C_2H_3$	$7.51 \times 10^{-8} \left(\frac{T_{gas}}{300}\right)^{-0.50}$	70

145

146

7. References

- 147 1. Berthelot, A., Kolev, S. & Bogaerts, A. Different Pressure Regimes of a Surface-Wave Discharge
148 in Argon: a Modeling Investigation. *Proc. ninth Int. Work. Microw. Discharges Fundam.*
149 *Applications* 58–62 (2015).
- 150 2. Friend, D. G., Ely, J. F. & Ingham, H. Thermophysical Properties of Methane. *J. Phys. Chem.*
151 *Ref. Data* **18**, 583–638 (1989).
- 152 3. Hassanpouryouzband, A., Joonaki, E., Edlmann, K., Heinemann, N. & Yang, J. Thermodynamic
153 and transport properties of hydrogen containing streams. *Sci. Data* **7**, 1–14 (2020).
- 154 4. Irikura, K. K. Experimental vibrational zero-point energies: Diatomic molecules. *J. Phys. Chem.*
155 *Ref. Data* **36**, 389–397 (2007).
- 156 5. Matveyev, A. A. & Silakov, V. P. Kinetic processes in a highly-ionized non-equilibrium hydrogen
157 plasma. *Plasma Sources Sci. Technol.* **4**, 606–617 (1995).
- 158 6. Loureiro, J. & Ferreira, C. M. Electron and vibrational kinetics in the hydrogen positive column.
159 *J. Phys. D. Appl. Phys.* **22**, 1680–1691 (1989).
- 160 7. Capitelli, M., Ferreira, C. M., Gordiets, B. F. & Osipov, A. I. *Plasma Kinetics in Atmospheric*
161 *Gases*. vol. 31 (Springer Berlin Heidelberg, 2000).
- 162 8. Gorse, C., Capitelli, M., Bacal, M., Bretagne, J. & Laganà, A. Progress in the non-equilibrium
163 vibrational kinetics of hydrogen in magnetic multicusp H- ion sources. *Chem. Phys.* **117**, 177–
164 195 (1987).
- 165 9. Juurlink, L. B. F., Killelea, D. R. & Utz, A. L. State-resolved probes of methane dissociation
166 dynamics. *Progress in Surface Science* vol. 84 69–134 (2009).

- 167 10. Menard-Bourcin, F., Boursier, C., Doyennette, L. & Menard, J. Rotational and vibrational
168 relaxation of methane excited to 2v3 in CH₄/H₂ and CH₄/He mixtures at 296 and 193 K from
169 double-resonance measurements. *J. Phys. Chem. A* **109**, 3111–3119 (2005).
- 170 11. Wang, J. C. F. & Springer, G. S. Vibrational relaxation times in some hydrocarbons in the range
171 300–900°K. *J. Chem. Phys.* **59**, 6556–6562 (1973).
- 172 12. Willard Richards, L. & Sigafos, D. H. Vibrational relaxation of methane. *J. Chem. Phys.* **43**,
173 492–497 (1965).
- 174 13. Cascella, M., Curik, R. & Gianturco, F. A. Vibrational excitation in electron-CH₄ collisions:
175 exchange interaction effects. *J. Phys. B At. Mol. Opt. Phys.* **34**, 705–723 (2001).
- 176 14. Bardsley, J. N. & Wadehra, J. M. Dissociative attachment and vibrational excitation in low-
177 energy collisions of electrons with H₂ and D₂. *Phys. Rev. A* **20**, 1398–1405 (1979).
- 178 15. Janev, R. K. & Reiter, D. Collision processes of CH_y and CH_y⁺ hydrocarbons with plasma
179 electrons and protons. *Phys. Plasmas* **9**, 4071 (2002).
- 180 16. Yoon, J. S. *et al.* Cross sections for electron collisions with hydrogen molecules. *J. Phys. Chem.*
181 *Ref. Data* **37**, 913–931 (2008).
- 182 17. Brian, J. & Mitchell, A. The dissociative recombination of molecular ions. *Physics Reports* vol.
183 186 215–248 (1990).
- 184 18. Janev, R. K., Reiter, D. & Samm, U. *Collision Processes in Low-Temperature Hydrogen*
185 *Plasmas. Sciences-New York* (2003).
- 186 19. Janev, R. K., Langer, W. D., Post, D. E. & Evans, K. *Elementary Processes in Hydrogen-Helium*
187 *Plasmas. Elementary Processes in Hydrogen-Helium Plasmas* (Springer Berlin Heidelberg,
188 1987). doi:10.1007/978-3-642-71935-6.
- 189 20. Florescu-Mitchell, A. I. & Mitchell, J. B. A. Dissociative recombination. *Phys. Rep.* **430**, 277–374
190 (2006).
- 191 21. Janev, R. K. & Reiter, D. Collision processes of C_{2,3}Hy and C_{2,3}Hy⁺ hydrocarbons with electrons
192 and protons. *Phys. Plasmas* **11**, 780–829 (2004).
- 193 22. Baulch, D. L. *et al.* Evaluated kinetic data for combustion modeling: Supplement II. *J. Phys.*
194 *Chem. Ref. Data* **34**, 757–1397 (2005).
- 195 23. Troe, J. & Ushakov, V. G. The dissociation-recombination reaction CH₄ (+M) ⇌ CH₃ + H (+M): A
196 case study for unimolecular rate theory. *J. Chem. Phys.* **136**, (2012).
- 197 24. Blitz, M. A. *et al.* Reanalysis of Rate Data for the Reaction CH₃ + CH₃ → C₂H₆ Using Revised
198 Cross Sections and a Linearized Second-Order Master Equation. *J. Phys. Chem. A* **119**, 7668–
199 7682 (2015).
- 200 25. Wang, H. Combustion Chemistry. in (2015).
- 201 26. Fahr, A., Laufer, A. H. & Tardy, D. C. Pressure effect on CH₃ and C₂H₃ cross-radical reactions.
202 *J. Phys. Chem. A* **103**, 8433–8439 (1999).
- 203 27. Seakins, P. W. *et al.* Kinetics of the unimolecular decomposition of iso-C₃H₇: Weak collision
204 effects in helium, argon, and nitrogen. *J. Phys. Chem.* **97**, 4450–4458 (1993).
- 205 28. Harding, L. B., Guadagnini, R. & Schatz, G. C. Theoretical studies of the reactions hydrogen
206 atom + methylidyne .fwdarw. carbon + hydrogen and carbon + hydrogen .fwdarw. methylene
207 using an ab initio global ground-state potential surface for methylene. *J. Phys. Chem.* **97**, 5472–
208 5481 (1993).
- 209 29. Tabayashi, K. & Bauer, S. H. The early stages of pyrolysis and oxidation of methane. *Combust.*
210 *Flame* **34**, 63–83 (1979).
- 211 30. Böhland, T., Döbē, S., Temps, F. & Wagner, H. G. Kinetics of the Reactions between
212 CH₂($\bar{X}3B1$)-Radicals and Saturated Hydrocarbons in the Temperature Range 296 K ≤ T ≤ 707
213 K. *Berichte der Bunsengesellschaft für Phys. Chemie* **89**, 1110–1116 (1985).
- 214 31. Canosa, A., Sims, I. R., Travers, D., Smith, I. W. M. & Rowe, B. R. Reactions of the methylidene
215 radical with CH₄, C₂H₂, C₂H₄, C₂H₆, and but-1-ene studied between 23 and 295 K with a CRESU
216 apparatus. *Astron. Astrophys* **323**, 644–651 (1997).
- 217 32. Flash photolysis of carbon suboxide: absolute rate constants for reactions of C(3P) and C(1D)
218 with H₂, N₂, CO, NO, O₂ and CH₄. *Proc. R. Soc. London. A. Math. Phys. Sci.* **312**, 417–434
219 (1969).

- 220 33. Chen, C.-J., Back, M. H. & Back, R. A. The thermal decomposition of methane. II. Secondary
221 reactions, autocatalysis and carbon formation; non-Arrhenius behaviour in the reaction of CH₃
222 with ethane. *Can. J. Chem.* **54**, 3175–3184 (1976).
- 223 34. Niedzielski, J., Gawłowski, J. & Gierczak, T. Dissociation of isomerization of excited C₃H₅
224 radicals in the gas phase. *J. Photochem.* **21**, 195–206 (1983).
- 225 35. Sutherland, J. W., Su, M.-C. & Michael, J. V. Rate constants for H + CH₄, CH₃ + H₂, and CH₄
226 dissociation at high temperature. *Int. J. Chem. Kinet.* **33**, 669–684 (2001).
- 227 36. Baulch, D. L. *et al.* Evaluated Kinetic Data for Combustion Modelling. *J. Phys. Chem. Ref. Data*
228 **21**, 411–734 (1992).
- 229 37. Han, P. *et al.* Reaction rate of propene pyrolysis. *J. Comput. Chem.* **32**, 2745–2755 (2011).
- 230 38. Warnatz, J. Rate Coefficients in the C/H/O System. in *Combustion Chemistry* 197–360 (Springer
231 New York, 1984). doi:10.1007/978-1-4684-0186-8_5.
- 232 39. Pilling, M. J. & Robertson, J. A. A rate constant for CH₂(3B1) + CH₃. *Chem. Phys. Lett.* **33**, 336–
233 339 (1975).
- 234 40. Czyzewski, A. *et al.* Investigation of kinetics of CH radical decay by cavity ring-down
235 spectroscopy. *Chem. Phys. Lett.* **357**, 477–482 (2002).
- 236 41. Galland, N., Caralp, F., Hannachi, Y., Bergeat, A. & Loison, J. C. Experimental and theoretical
237 studies of the methylidyne CH(X2[Σ]) radical reaction with ethane (C₂H₆): Overall rate constant
238 and product channels. *J. Phys. Chem. A* **107**, 5419–5426 (2003).
- 239 42. Tsang, W. & Hampson, R. F. Chemical Kinetic Data Base for Combustion Chemistry. Part I.
240 Methane and Related Compounds. *J. Phys. Chem. Ref. Data* **15**, 1087–1279 (1986).
- 241 43. Tsang, W. Chemical Kinetic Data Base for Combustion Chemistry. Part 3: Propane. *J. Phys.*
242 *Chem. Ref. Data* **17**, 887–951 (1988).
- 243 44. Allara, D. L. & Shaw, R. A compilation of kinetic parameters for the thermal degradation of *n*-
244 alkane molecules. *J. Phys. Chem. Ref. Data* **9**, 523–560 (1982).
- 245 45. Fahr, A. & Tardy, D. C. Rate coefficients and products of ethyl and vinyl cross-radical reactions.
246 *J. Phys. Chem. A* **106**, 11135–11140 (2002).
- 247 46. Tsang, W. Chemical Kinetic Data Base for Combustion Chemistry Part V. Propene. *J. Phys.*
248 *Chem. Ref. Data* **20**, 221–273 (1991).
- 249 47. Mandal, M., Ghosh, S. & Maiti, B. Dynamics of the C(3P) + Ethylene Reaction: A Trajectory
250 Surface Hopping Study. *J. Phys. Chem. A* **122**, 3556–3562 (2018).
- 251 48. Knyazev, V. D., Bencsura, Á., Stoliarov, S. I. & Slagle, I. R. Kinetics of the C₂H₃ + H₂ \rightleftharpoons H + C₂H₄
252 and CH₃ + H₂ \rightleftharpoons H + CH₄ Reactions. *J. Phys. Chem.* **100**, 11346–11354 (1996).
- 253 49. Martinotti, F. F., Welch, M. J. & Wolf, A. P. The reactivity of thermal carbon atoms in the gas
254 phase. *Chem. Commun.* **5**, 115 (1968).
- 255 50. Kruse, T. & Roth, P. Kinetics of C₂ reactions during high-temperature pyrolysis of acetylene. *J.*
256 *Phys. Chem. A* **101**, 2138–2146 (1997).
- 257 51. Mayer, S. W., Schieler, L. & Johnston, H. S. Computation of high-temperature rate constants for
258 bimolecular reactions of combustion products. in *Symposium (International) on Combustion* vol.
259 11 837–844 (1967).
- 260 52. Dean, A. J. & Hanson, R. K. CH and C-atom time histories in dilute hydrocarbon pyrolysis:
261 Measurements and kinetics calculations. *Int. J. Chem. Kinet.* **24**, 517–532 (1992).
- 262 53. Hassouni, K., Capitelli, M., Esposito, F. & Gicquel, A. State to state dissociation constants and
263 non-equilibrium vibrational distributions under microwave hydrogen plasmas. *Chem. Phys. Lett.*
264 **340**, 322–327 (2001).
- 265 54. McElroy, D. *et al.* The UMIST database for astrochemistry 2012. *Astron. Astrophys.* **550**, 36
266 (2013).
- 267 55. McEwan, M. J. *et al.* New H and H₂ Reactions with Small Hydrocarbon Ions and Their Roles in
268 Benzene Synthesis in Dense Interstellar Clouds. *Astrophys. J.* **513**, 287–293 (1999).
- 269 56. Kim, J. K., Anicich, V. G. & Huntress, W. T. Product distributions and rate constants for the
270 reactions of CH₃⁺, CH₄⁺, C₂H₂⁺, C₂H₃⁺, C₂H₄⁺, C₂H₅⁺, and C₂H₆⁺ ions with CH₄, C₂H₂, C₂H₄, and
271 C₂H₆. *J. Phys. Chem.* **81**, 1798–1805 (1977).

- 272 57. Smith, D. & Adams, N. G. Some positive ion reactions with H₂: Interstellar implications. *Mon.*
273 *Not. R. Astron. Soc.* **197**, 377–384 (1981).
- 274 58. Anicich, V. G. Evaluated Bimolecular Ion-Molecule Gas Phase Kinetics of Positive Ions for Use
275 in Modeling Planetary Atmospheres, Cometary Comae, and Interstellar Clouds. *J. Phys. Chem.*
276 *Ref. Data* **22**, 1469–1569 (1993).
- 277 59. Herbst, E. & Leung, C. M. Synthesis of complex molecules in dense interstellar clouds via gas-
278 phase chemistry: model update and sensitivity analysis. *Mon. Not. R. Astron. Soc.* **222**, 689–
279 711 (1986).
- 280 60. Prasad, S. S. & Huntress, W. T., J. A model for gas phase chemistry in interstellar clouds. II -
281 Nonequilibrium effects and effects of temperature and activation energies. *Astrophys. J.* **239**,
282 151 (1980).
- 283 61. Payzant, J. D., Schiff, H. I. & Bohme, D. K. Determination of the proton affinity from the kinetics
284 of proton transfer reactions. V. The equilibrium H₃⁺ + Kr ? KrH⁺ + H₂ and the relative proton
285 affinity of Kr and H₂. *J. Chem. Phys.* **63**, 149–153 (1975).
- 286 62. Smith, D., Spanel, P. & Mayhew, C. A. A selected ion-flow tube study of the reactions of O⁺, H⁺
287 and HeH⁺ with several molecular gases at 300 K. *Int. J. Mass Spectrom. Ion Process.* **117**, 457–
288 473 (1992).
- 289 63. Martinez, O., Yang, Z., Demarais, N. J., Snow, T. P. & Bierbaum, V. M. Gas-phase reactions of
290 hydride anion, H⁻. *Astrophys. J.* **720**, 173–177 (2010).
- 291 64. Martinez, Jr., O. *et al.* Gas Phase Study of C⁺ Reactions of Interstellar Relevance. *Astrophys. J.*
292 **686**, 1486–1492 (2008).
- 293 65. Smith, D. & Adams, N. G. Molecular synthesis in interstellar clouds - Some relevant laboratory
294 measurements. *Astrophys. J.* **217**, 741 (1977).
- 295 66. Woodall, J., Agúndez, M., Markwick-Kemper, A. J. & Millar, T. J. The UMIST database for
296 astrochemistry 2006. *Astron. Astrophys.* **466**, 1197–1204 (2007).
- 297 67. Harada, N. & Herbst, E. Modeling Carbon Chain Anions in L1527. *Astrophys. J.* **685**, 272–280
298 (2008).
- 299 68. Gordiets, B., Ferreira, C. M., Pinheiro, M. J. & Ricard, A. Self-consistent kinetic model of low-
300 pressure N₂-H₂ flowing discharges: II. Surface processes and densities of N, H, NH₃ species.
301 *Plasma Sources Sci. Technol.* **7**, 379–388 (1998).
- 302 69. Bruhns, H., Kreckel, H., Miller, K. A., Urbain, X. & Savin, D. W. Absolute energy-resolved
303 measurements of the H⁻ + H → H₂ + e⁻ associative detachment reaction using a merged-beam
304 apparatus. *Phys. Rev. A - At. Mol. Opt. Phys.* **82**, 42708 (2010).
- 305 70. Millar, T. J., Walsh, C. & Field, T. A. Negative ions in space. *Chemical Reviews* vol. 117 1765–
306 1795 (2017).
- 307 71. Villano, S. M., Eyet, N., Lineberger, W. C. & Bierbaum, V. M. Gas-phase reactions of
308 halogenated radical carbene anions with sulfur and oxygen containing species. *Int. J. Mass*
309 *Spectrom.* **280**, 12–18 (2009).
- 310 72. Yurtsever, E., Satta, M., Wester, R. & Gianturco, F. A. On the Formation of Interstellar CH⁻
311 Anions: Exploring Mechanism and Rates for CH₂ Reacting with H⁻. *J. Phys. Chem. A* **124**, 5098–
312 5108 (2020).
- 313